



BOUNDARY SHEAR STRESSES
IN
CURVED TRAPEZOIDAL CHANNELS

by

Philip Aldrich Drinker

B.S., Yale University
(1954)

Submitted in Partial Fulfillment of the
Requirements for the Degree of
Doctor of Philosophy

at the

Massachusetts Institute of Technology
(1961)

Signature of Author _____

Departments of Civil and Sanitary Engineering
and
Geology and Geophysics
August 20, 1961

Certified by _____

Thesis Supervisor

Chairman, Departmental Committee on Graduate Students



Room 14-0551
77 Massachusetts Avenue
Cambridge, MA 02139
Ph: 617.253.5668 Fax: 617.253.1690
Email: docs@mit.edu
<http://libraries.mit.edu/docs>

DISCLAIMER OF QUALITY

Due to the condition of the original material, there are unavoidable flaws in this reproduction. We have made every effort possible to provide you with the best copy available. If you are dissatisfied with this product and find it unusable, please contact Document Services as soon as possible.

Thank you.

There are numerous pages where the pagination is illegible.

ABSTRACT

Boundary Shear Stresses in Curved
Trapezoidal Channels

by

Philip Aldrich Drinker

Submitted to the Department of Civil and Sanitary Engineering, and the Department of Geology and Geophysics, in partial fulfillment of the requirements for the degree of Doctor of Philosophy.

An investigation is described on the distribution and magnitudes of boundary shear stresses arising from subcritical flows through curved trapezoidal channels. A series of tests was conducted to determine the effects on the stream patterns of variation in discharge, bend geometry, boundary roughness, and upstream channel alignment.

Two flumes of different bend radius and base width were used, each consisting of a single circular curve of 60° central angle, with straight upstream and downstream tangent sections. Both flumes were constructed with 2 to 1 side slopes, and the base horizontal along all transverse sections.

The greatest part of the test program dealt with flows in smooth channels. For a Froude number range of 0.32 to 0.55, the stream geometries varied as follows: ratio of width to depth, $7 < w/y_0 < 12$; ratio of width to centerline radius, $0.29 < w/r_c < 0.80$. Two tests were conducted in a rough surfaced channel at stream geometries corresponding to runs in the smooth channel series. For the final four tests described, which were conducted in a smooth channel, sets of screens were installed in the approach flow in order to simulate the disturbances caused by additional curves upstream from the test reach. By this method, the shear distribution was studied for systems of two curves of similar sense, and for sets of reverse curves.

Local boundary shear stresses were measured with surface Pitot tubes adapted for application in free surface flows. The calibration for these instruments, originally developed for air flows through smooth pipes, was found to be valid for direct application in the smooth channels. A modified Pitot tube was developed and calibrated for use on the rough test surface.

The boundary shear stress data are presented as relative shear, $\tau_0/\bar{\tau}_0$ (i.e. as local shear in terms of the shear for uniform flow) in the form of contour maps of the test reach; velocities and water surface elevations are presented by section.

The boundary shear patterns obtained cannot be predicted quantitatively from the gross characteristics of the flow. Local shears were

found to occur at intensities of more than double the mean tractive force computed for uniform flow; as might be expected, the intensities of these local shears increase markedly with the stream curvature. A one-dimensional treatment of the energy dissipation in the curve and downstream tangent fails to indicate either the peripheral locations or the intensities of the greatest boundary stresses. In general, the distributions and the relative magnitudes of the local boundary shear stresses appear to be functions of the stream geometry, for streams in subcritical motion.

The patterns of velocity and shear in a stream curve are influenced, both directly and indirectly, by the transverse and longitudinal pressure gradients in the curve. An analysis of the water surface superelevation in curving flow reveals that, for conditions of moderate curvature, the transverse water slope is quite insensitive to variations in the velocity distribution, and that it depends only on the mean momentum of the flow and the stream geometry.

Thesis Supervisor: Arthur T. Ippen
Title: Professor of Hydraulics

ACKNOWLEDGEMENT

This investigation was conducted at the Hydrodynamics Laboratory of the Massachusetts Institute of Technology. The work was supported, through the Institute Division of Sponsored Research, by the Soil and Water Conservation Research Division, Agricultural Research Service, U.S. Department of Agriculture, under Contract Number 12-14-100-2590(41) and Cooperative Research Agreement No. 12-14-100-5227(41).

The author is deeply indebted to Dr. Arthur T. Ippen, who, in supervising the investigation, contributed immeasurably to its success. His interest and encouragement led to the uncovering of many facets of the problem which otherwise had been overlooked.

The author is also especially grateful to Messrs. William R. Jobin, and Omar H. Shemdin who were associated with the project as Research Assistants. Mr. Jobin performed much of the experimental work and analysis, and his numerous contributions were vital. Mr. Shemdin, who joined the project after the completion of the experimental work, contributed greatly in the final treatment of the results. The drawings prepared by both these men are gratefully acknowledged.

Messrs. Carl R. Miller and Donald A. Parsons of the Agricultural Research Service were instrumental in setting up the cooperative investigation, and their constant interest made this cooperation both pleasant and productive. The author appreciates their patient criticism and their suggestions arising from the related field problems.

Dr. John P. Miller of Harvard University introduced the author to the field of Geomorphology. Through his guidance in the literature and from warm personal contacts in seminars and informal meetings, the author

developed a real interest in the broadest aspects of fluvial morphology. The sudden death of Dr. Miller in July 1961 cut short the career of an able and dedicated teacher and a leader in modern geomorphology. As with all who knew him, the author feels a great personal loss in his death.

The author also expresses sincere thanks to:

Dr. Ronald E. Nece, who provided technical supervision during the initial phases of the study.

Messrs. Charles A. Givler and George K. Noutsopoulos, who performed thesis research on the project, and from whose data the author has drawn freely.

Mr. Wallace Fleming and the staff of the Laboratory Shop who assisted in the design and instruction of much of the test equipment.

Finally, acknowledgement is made for the contributions of the various members of the Laboratory Staff who have shown interest in the progress of this work. Many suggestions were received through informal discussions; these ideas became integrated into the final result, and as such it would be impossible to acknowledge each separately. To all who so contributed the author is sincerely grateful.

Cambridge, Massachusetts
August, 1961

TABLE OF CONTENTS

	Page
Abstract	i
Acknowledgement	iii
Table of Contents	v
List of Tables	vii
List of Figures	ix
Definitions and Notations	x
I. INTRODUCTION	1
II. FLOW THROUGH CURVED CHANNELS: A REVIEW	4
III. EXPERIMENTAL EQUIPMENT AND TECHNIQUES	11
A. The Test Channel	11
B. Instrumentation	15
1. The Measurement of Boundary Shear Stress	
a. General Requirements	
b. Shear Measurement by Surface Pitot Tubes	
c. Experimental Applications	
(i) Smooth Surface	
(ii) Rough Surface	
2. Additional Instrumentation	
a. Pressure Measurements	
b. Depth Measurements	
c. Velocity Measurements	
IV. THE EXPERIMENTAL PROGRAM	22
A. Scope of the Study	22
B. Presentation of Data	26
V. DISCUSSION OF RESULTS	28
A. Tests Conducted with Uniform Approach Flow	28
1. Smooth Channel	
2. Rough Channel	
B. Tests With Simulated Compound Curve Systems	52
C. Superelevation in a Channel Curve	64
D. Energy Dissipation in the Curved Reach	72
E. Scour Patterns in Alluvial Streams	83

	Page
VI. CONCLUSIONS	89
VII. BIBLIOGRAPHY	94
VIII. APPENDIX	97
A. The Test Channel Facility	97
B. Instrumentation	102
C. Techniques for the Measurement of Boundary Shear Stress: A Review	109
D. The Measurement of Boundary Shear Stress with Surface Pitot Tubes	113
E. Experimental Error	126
IX. BIOGRAPHICAL NOTE	129

LIST OF TABLES

<u>Table</u>		<u>Page</u>
I	The Range of Channel Geometries Covered in the Test Program	23
II	Summary of Test Conditions Determined in the Approach Flow	24
III	Maximum Water Surface Superelevations, Measured and Computed	68
IV	Comparison of the Average Rates of Energy Dissipation in the Test Reach	77

APPENDIX

A-I	Summary of Previous Investigation on the Calibration of Round Surface Pitot Tubes	118
-----	---	-----

LIST OF FIGURES

<u>Figure</u>		<u>Page</u>
1.	Zones of Separation in a Laboratory Channel Bend	7
2.	Helicoidal Motion in a Channel Bend	7
3.	The Two Trapezoidal Test Channels	12
4.	Model III Surface Pitot Tube	19
5.	Velocity Distributions: Run No. 1	30
6.	Velocity Distributions: Run No. 4-B	30
7.	Velocity Distributions: Run No. 6	30
8.	Transverse Water Surface Profiles, all Stations, Run No. 1	31
9.	Transverse Water Surface Profiles, Station 5, Runs No. 5, 6, 7	31
10.	Peripheral Distribution of Boundary Shear in Straight Trapezoidal Channels	36
11.	Boundary Shear Contour Map: Run No. 1	37
12.	Boundary Shear Contour Map: Run No. 2	38
13.	Boundary Shear Contour Map: Run No. 3	39
14.	Boundary Shear Contour Map: Run No. 4	40
15.	Boundary Shear Contour Map: Run No. 5	41
16.	Boundary Shear Contour Map: Run No. 6	42
17.	Boundary Shear Contour Map: Run No. 7	43
18.	Velocity Distributions: Run No. 9	47
19.	Transverse Water Surface Profiles: Run No. 9	47
20.	Boundary Shear Contour Map: Run No. 8	49
21.	Boundary Shear Contour Map: Run No. 9	50
22.	Velocity and Shear Distributions in the Approach Flow: Run No. 10	53
23.	Velocity and Shear Distributions in the Approach Flow: Run No. 11	53
24.	Velocity and Shear Distributions in the Approach Flow: Run No. 12	53
25.	Velocity and Shear Distributions in the Approach Flow: Run No. 13	53

Figure		Page
26.	Transverse Water Surface Profiles: Run No. 11	54
27.	Transverse Water Surface Profiles: Run No. 13	54
28.	Boundary Shear Contour Map: Run No. 10	57
29.	Boundary Shear Contour Map: Run No. 11	58
30.	Boundary Shear Contour Map: Run No. 12	59
31.	Boundary Shear Contour Map: Run No. 13	60
32.	Plot of Computed Maximum Superelevation	68
33.	Shear Distribution by Sections: Runs No. 1 and 4-B	75
34.	Average Rate of Energy Dissipation through the Curve: Runs No. 1 and 4-b	76
35.	Variation with Curvature of the Total Mean Shear Stress	78
36.	Variation with Curvature of the Maximum Relative Shear	78
37.	Variation with Curvature of Scour Areas	78
38.	Map and Sections of an Alluvial Stream	85

APPENDIX

A-1	General Plan of Experimental Facility	99
A-2	Overall View of Channel	100
A-3	Instrument Carriage Mounted in the Curve	100
A-4	Baffle Screen Arrangement for Simulated Curve	101
A-5	Surface Drag Screen used in Curve Simulation	101
A-6	Pitot Tube for Measuring Velocities near the Wall	103
A-7	Model II Surface Pitot Tube	103
A-8	Micromanometer	104
A-9	Development of the Inclined Manometer	104
A-10	Inclined Manometer	104
A-11	Velocity Distribution above the Smooth Test Surface	121
A-12	The Simplified Preston Calibration Curve	121
A-13	Velocity Distribution above the Rough Test Surface	122
A-14	Surface Pitot Tube Calibration, Rough Boundary	122

DEFINITIONS AND NOTATIONS

- A = channel cross-section area.
- b = bottom width of channel.
- C_{fx} = mean coefficient of friction at section s = $\tau_x / \frac{\rho V_x^2}{2}$.
- d = diameter of Pitot and Prandtl tubes.
- IF = Froude Number = $V / \sqrt{gy_m}$.
- g = gravitational acceleration, ft/sec².
- H_0 = specific Head, $y_0 + V^2/2g$, ft-lb/lb.
- ΔH = manometer reading, ft. of water.
- k = absolute height of roughness particle.
- k_s = equivalent sand roughness height.
- L = centerline arc length of the test reach.
- p_t = total, or stagnation pressure, lb/ft².
- p_o = static pressure, lb/ft².
- P = wetted perimeter.
- Q = volumetric rate of flow, ft³/sec.
- r = radial distance to a point in curve.
- r_c = radius of curvature of channel centerline.
- r_o = radius of curvature of outer edge of water surface.
- R = hydraulic radius, A/P, ft.
- R = Reynolds number, $4RV/\nu$.
- R_x = Boundary layer Reynolds Number V_x/ν .
- R_* = Shear Reynolds number, u_*y/ν .
- S_o = channel slope, ft/ft.
- S_e = energy gradient ft/ft.
- \bar{S}_{eL} = average energy gradient over the test reach.

- Se_x = local rate of energy dissipation at section x, ft-lb/lb/ft.
 T = water temperature, °F.
 u, v = local velocity, ft/sec.
 u_* = shear velocity, $\sqrt{\tau_0/\rho}$, ft/sec.
 V = free stream velocity or average velocity, Q/A , ft/sec.
 w = water surface width.
 x = longitudinal distance measured along channel centerline.
 y = distance normal to plane of channel bottom.
 y_m = average depth = A/w .
 y_0 = total depth of flow.
 z = transverse distance.
 α = angular misalignment of test probe.
 γ = specific weight of liquid, lb/ft³
 δ = boundary layer thickness, ft.
 θ = local central angle of curvature from beginning of bend, degrees.
 μ = dynamic viscosity of fluid, lb-sec/ft².
 ν = kinematic viscosity of fluid, ft²/sec.
 ρ = mass density of fluid, slugs/ft³
 τ_0 = local boundary shear stress, lb/ft².
 $\bar{\tau}_0$ = average boundary shear stress at curve entrance (Sta.1) lb/ft².
 τ_x = average boundary shear stress at section x.
 $\bar{\tau}_L$ = average boundary shear stress over the full test reach.
 $f(), \phi()$ = function of.

I. INTRODUCTION

Stream meandering has become a problem of real economic importance in recent years as the amount of valuable land destroyed by bank erosion steadily increases. In large, navigable streams, meandering must be corrected and controlled by costly dredging, and by construction of revetments. The amount of agricultural land lost due to erosion by smaller alluvial streams can hardly be estimated, but its extent has stimulated an increasing amount of research in this field. The immediate practical interest has been in developing methods to stabilize the streams and so to prevent further progression of the meanders.

For lack of systematic quantitative information on the modes of erosion in curves, the installation of revetments has an empirical basis, founded upon field studies of localized stream systems (36)(42). The success of these revetment projects has been so varied that it is still not possible to design stabilization works with assurance. In general, the cost of stabilizing small alluvial streams is in excess of \$50,000 per mile of channel. Not only is there great variation among streams in different regions of the country, but in a given stream the regime varies with time. It is quite common to find several feet of alluvium deposited over new revetments in an area which had formerly been undergoing active erosion.

A great deal of effort has been devoted to the general study of stream hydraulics and stream morphology (24)(27)(28)(43). Laboratory studies (13)(26), have resulted in further understanding of the geometry of meander patterns in alluvial streams. These investigations give a fairly good indication to the engineer of what to expect in the way of

0000

meander patterns and downvalley progression of bands, but they do not supply him with adequate information to control these phenomena. In addition, studies of velocity distributions in bends (31)(39) have been useful in gaining a clearer conception of the dynamics of stream flow through curves, but they fail to delineate the extent and degree of attack on the stream bed. A flowing stream dissipates its energy through shear or tractive forces on its boundaries. For an alluvial stream which is free from obstructions and major irregularities, erosion and movement of bed material will be controlled by this boundary shear stress and the current pattern. The shear stress parameter has long been used in the definition of stability of straight channels and has been extensively studied (10)(22)(25). For such a channel the average shear stress can be computed reasonably well from a coefficient of resistance and the mean velocity head. Within a curved reach however, the local shear stresses vary in a manner which cannot be predicted at present due to the effects of local accelerations and of secondary motion in the flow.

It is recognized that to completely divorce the problem of erosion from the related problems of deposition and sediment transport is, in the final analysis, unrealistic. Not only do all three factors appear to be integral aspects of the continuously variable phenomenon of sediment mechanics, but there is also compelling evidence that the presence of suspended particles modifies the dynamic properties of the transporting fluid (3)(9)(45). However, the quantitative understanding of these latter phenomena is still a very distant goal, and an experimental attack on the whole problem would not permit at present a clear cut separation of the various influences inherent in this problem. For this reason a limited experimental program was adopted in which all sediment properties are

excluded, the channel geometry remains clearly defined and only the effect of the flow pattern on the boundary is determined.

The experimental phase of the investigation consists of a series of tests conducted in curving trapezoidal channels. For fixed boundary geometries, boundary shear stresses were mapped under varied conditions of flow. An attempt is made, insofar as possible, to correlate trends in the shear patterns with variations in flow rate and geometry. Velocity distributions and water surface configurations were recorded for assistance in developing a more general understanding of curved flow, through which erosive attack in channel boundaries may be anticipated.

It is hoped that ultimately these findings may have practical value in determining the degree and areal extent of protective works required to stabilize natural stream channels. The practical applications of this work will be limited to those cases where mean shear stress is a dominant factor in bank stability, such as in streams flowing over surfaces of relatively uniform texture. The introduction of individual bank protrusions creates yet another problem which is not amenable to treatment by this simplified approach.

II. FLOW THROUGH CURVED CHANNELS: A REVIEW

As a basic model of flow through channel curves, consider first the flow through a deep, smooth-surfaced, prismatic bend. If frictional effects are assumed negligible, potential theory permits description of the curved flow as a free vortex. Mockmore (31), among others, has demonstrated that at some distance from the boundaries both the velocity distribution and the transverse water surface profile are well described by an irrotational vortex. For this case the transverse velocity distribution is given by the constant product of local tangential velocity, u , and radius, r . By equating the radial forces on a fluid particle as,

$$\frac{dp}{dr} = \rho \frac{u^2}{r} \quad (1)$$

the water surface profile can be computed from

$$\Delta y = \frac{1}{g} \int \frac{u^2}{r} dr, \quad (2)$$

where the flow in the curve is assumed to be concentric. For the free vortex the water surface profile is hyperbolic, convex upward.

However, examination of the flow near the boundaries shows that even in a smooth-walled flume, frictional effects combined with the superelevation tend to cause two important deviations from potential flow: helicoidal motion of the main stream and separation in zones of adverse pressure gradient.

In 1876 Thompson (44) gave his now familiar explanation of helicoidal, or spiral flow as being due to the difference in centripetal acceleration between the fluid near the bottom, which has been retarded by boundary drag, and the faster moving layers near the free surface.

This acceleration, which results from the radial increase in depth (and hence in pressure) causes the low velocity fluid near the bed to move towards the center of the curve, while the fluid near the surface, having excess momentum, moves towards the outside.

The superelevation of the water surface in a channel curve leads to two occurrences of longitudinal increase in depth: along the outer bank of the curve as the water rises entering the curve, and at the curve exit along the inner bank where the flow recovers to normal depth (see for example, Figures 5 and 8). For channels of large curvature separation may develop in these two areas and the water surface may slope upstream locally. The fluid particles near the boundary have insufficient kinetic energy to move against a pressure gradient and separation of the boundary layer from the streambank results. A simple circular curve connecting two tangent channels is likely to produce larger separation zones than would a natural stream bend, with more gradual transitions. In periods of high flows separation in natural channel bends manifests itself as eddies or "bank rollers" and results in bar deposits.

It has been pointed out (26)(46) that superelevation as such in subcritical, curving flow is quite insensitive to radial variation in the velocity distribution. Substitution into Equation (2) of other assumed velocity distributions, and integration over the full width of the stream, gives only minor variations in the total elevation difference, even though the surface profiles vary in shape. Superelevation is a result of curved flow for all fluids, and is essentially independent of the frictional aspects and the velocity distribution of the flow. It is controlled primarily by the boundary geometry and the mean momentum of the stream. Thus, while superelevation provides the mechanism by which

separation and helicoid motion take place, their direct cause is boundary friction or shear stress, and in a completely frictionless flow they could not occur.

In deep, turbulent streams, the separation zone at the concave bank is usually obliterated by the turbulent infusion of momentum from the main body of the stream, although bank rollers are observed at the outside of abrupt, shallow bends. The separation zone at the inner bank is more persistent, as shown by the point bar deposits common to virtually all streams except those which are deeply incised and actively degrading. The persistence and extent of this latter zone is due both to the abrupt rise in water surface at this point, and to the spiral motion of the stream which tends to move the faster moving fluid to the opposite bank.

Examples of helicoidal motion and separation in a laboratory flume bend are shown in Figures 1 and 2. Both of these photographs were taken from the bend exit, facing upstream, so that the flow is from top to bottom of the photographs. Figure 1 was taken after dye had been injected and allowed to spread to the full extent of the separation zones. In Figure 2 the fainter dark streaks were caused by dye crystals moving towards the inner bank with the bottom current (the dashed arrow) while the heavier plume was made by continuous injection of dye at the surface, (the solid arrow).

These two phenomena have far reaching effects on the flow in natural streams. The helicoidal pattern is, perhaps, the more important, in that, by shifting the faster moving fluid to the outside of the bend, it tends to suppress the free vortex pattern. Einstein and Harder (8) show experimentally that, for a curve of sufficient length, a stable velocity distribution develops in which the velocity increases radially

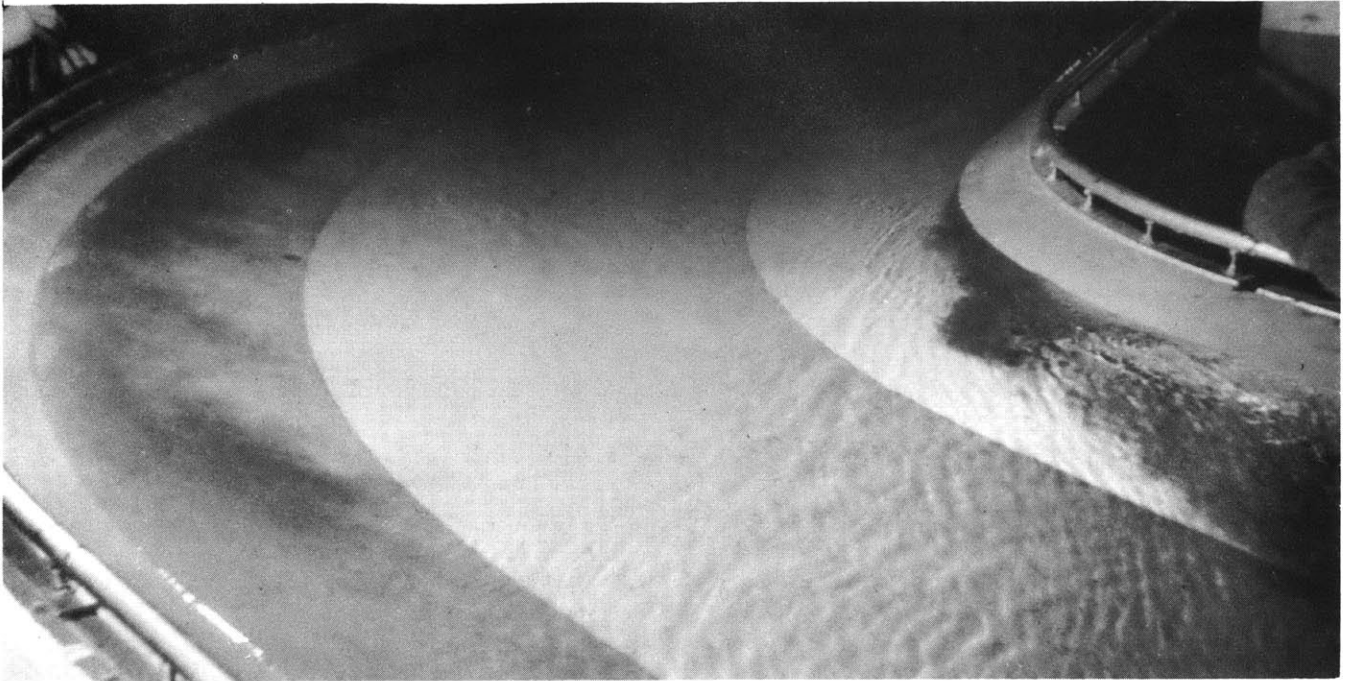


Figure 1. (above)
Zones of Separation
in Laboratory Channel
Bend.



Figure 2. (left)
Helicoidal Flow in
Channel Bend.

outwards. That is, of course, the phenomenon observed in long river curves in which the thalweg remains near to the concave bank.

The pattern of helicoidal flows in the bend of a rectangular flume was studied by Shukry (39) using a Pitot sphere to determine the three components of the local velocity vector. It was found that the helicoidal (i.e. radial) velocities increase with increasing relative curvature, w/r_c and ratio of width to depth, w/y_0 . Einstein and Harder (8) also observed that increasing the ratio, w/y_0 , as well as increasing the boundary roughness, led to high velocities towards the outer bank, due, presumably, to a more pronounced helicoidal motion.

The laboratory bends in which the irrotational type of flow is observed are too short to complete the transfer of the filament of highest velocity to the outer bank. The patterns of flow in sharp bends -- of both flumes and rivers -- represent a transitional type which, with sufficient length of curved reach, would develop into the friction controlled flow described above. The length of this transition reach, however, has not been well defined in terms of the pertinent parameters.

Recently Leopold and co-workers (26) have reported an investigation on the frictional resistance of rigid sinuous channels. By studying the overall head loss over a reach, for channels of constant shape but varied sinuosities, the authors show that not only is the total energy dissipation greater in curved channels than in straight, but that it increases discontinuously above a certain threshold Froude number, due to the formation of local standing waves, or "spills", along the banks. While the rate of increase in total boundary shear is not clearly defined, a relationship is suggested between the ratio of width to radius and the Froude number at which the discontinuity occurs. In the laboratory tests

(10)

the threshold Froude number varied from about 0.4 to 0.6, while, from a survey of river data, the authors found that bankfull flows generally occur in streams in the range $0.2 < F < 0.45$. They suggest that the rare occurrence of higher Froude numbers may be due to a tendency of alluvial rivers to eliminate local areas of high resistance. Such a local reduction in boundary shear could come about through erosion of the banks at points of greatest spill occurrence, where there is increased dissipation of energy.

The relationship between shear stresses and erosion is further complicated in natural streams by loose bed material which permits an additional degree of freedom not possessed by rigid boundary flumes. This freedom to shape its own bed undoubtedly causes a river to alter its flow pattern in ways which cannot readily be predicted from a study of rigid, prismatic channels (23). Thus, scour will occur in regions of high shear stress; the modifications in the bed configuration caused by the scour will in turn modify the current pattern and hence the shear distribution.

Previous investigations of energy dissipation in curved flow have been restricted to one-dimensional analyses for both open and enclosed conduits. As shown by Anderson (2), the different experimental techniques, as well as the varied definitions of a loss coefficient, used by past investigators have led to considerable confusion. Ito (21) has demonstrated, by a re-analysis of early data, that the loss coefficient of a smooth bend can be predicted empirically, if the measurements and definitions are given a common basis. With respect to the present study, a one-dimensional approach is not very revealing in that it gives no indication as to the distribution of the boundary shear stresses which

cause the loss in bends. Indeed, as is shown in the discussion to follow, the mean section loss gives little indication of the magnitudes of the local shears, and that the location and intensity of erosive attack cannot be predicted by this means.

III. EXPERIMENTAL EQUIPMENT AND TECHNIQUES

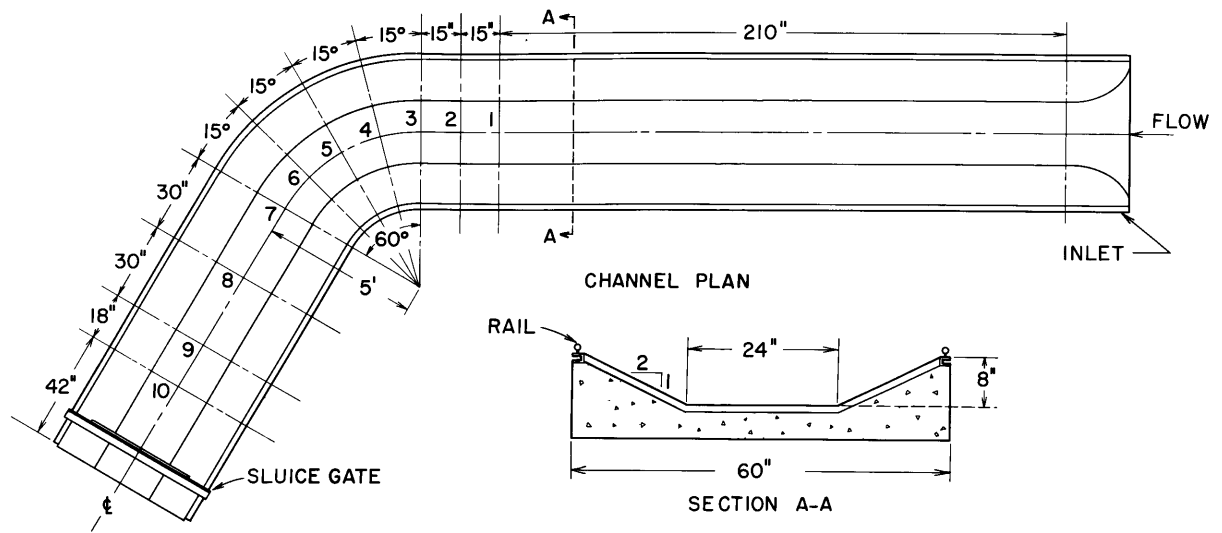
A. The Test Channel

1. Description of the Equipment

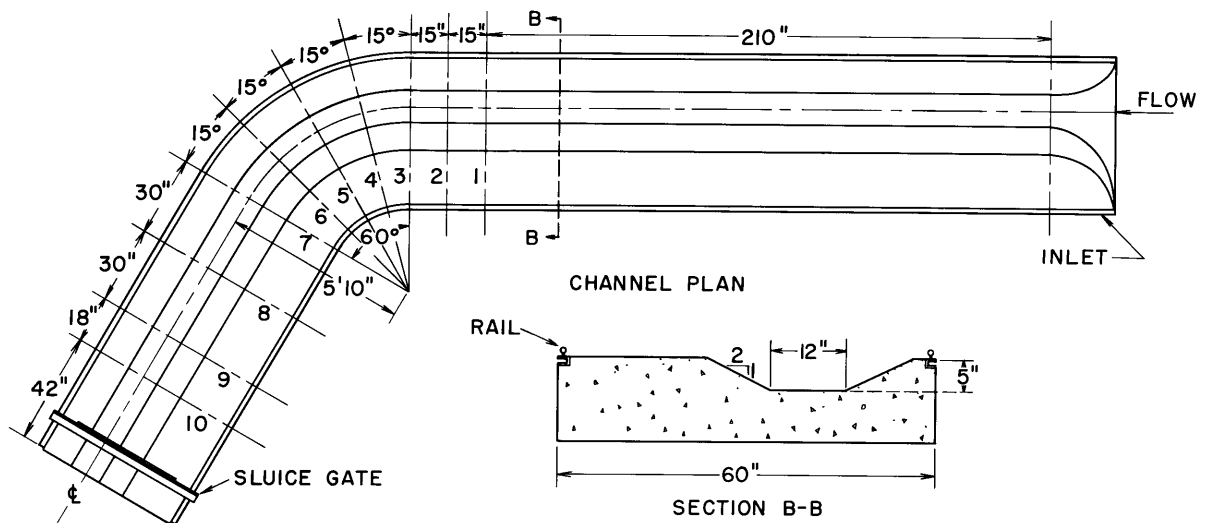
The experiments were conducted in the two trapezoidal flumes shown in Figure 3. In both channels the general arrangement is the same, consisting of a straight approach section 20 feet in length, a single curve of 60 degree central angle, and a straight 10 foot exit section. The side slopes are constant at 2 horizontal to 1 vertical and the channels were constructed with the invert horizontal along all radial sections. A smooth entrance transition from the stilling basin at the upstream end of the approach channel reduces the tendencies for local separation. Additional control of depth is provided by an adjustable sluice gate mounted at the exit section. Details of the basic design of the channel facility are given in Appendix A.

The larger flume (Figure 3a) has a 24-inch base width, and the radius of the curve centerline is 60 inches. For the smaller flume, which was laid in the bed of the larger, the base width dimension was halved, and the stream section was shifted outward to follow the concave bank of the original curve, giving a curve centerline radius of 70 inches.

In a curved trapezoidal stream, the relative curvature -- i.e. the ratio of surface width to bend radius -- varies with depth and thus cannot be given solely in terms of the boundary geometry. However, the limiting values of relative curvature are those set by the base width. Thus, the range of curvatures which may be obtained in the two flumes is limited by $\frac{w}{r_c} > \frac{b}{r_c} = 0.40$ and $\frac{w}{r_c} > \frac{b}{r_c} = 0.17$ in the larger and smaller channels, respectively. In each channel, therefore, tests at several depths give a



(a)



(b)

Figure 3. The Trapezoidal Channels. The locations of the ten test stations are indicated by the dashed section lines.

moderate range in relative curvature, the lower limit of which is fixed by the boundary curvatures, $\frac{b}{r_c}$.

During the installation of the original flume structure, the centerline slope was set at $0.00064 = 1/1563$. The slope was not adjusted throughout the test program; however, after construction of the smaller channel, it was found that the approach slope had decreased to 0.00055 due to settling of the foundations.

The channels were treated with a waterproof plastic coating which dries to form a tough elastic film. For the series of smooth boundary tests it was found that this material provides a hydraulically smooth surface, giving a mean Manning coefficient of 0.010 .

For the rough boundary tests which were conducted in the larger channel the surface was prepared as follows: the channel was given two coats of varnish; while the surface was still wet, roughness particles were spread by hand over the bottom and sidewalls of the section. After the material had dried, the surface was scraped with a flat bar to knock off any protruding particles, and then sealed with a final coat of varnish. The rough surface was applied over 15 feet of the approach section, through the curve and for 8 feet in the exit reach. The roughness particles are uniform, rectangular, lucite parallelepipeds, of the approximate dimensions, $0.18 \times 0.10 \times 0.10$ inches. The absolute roughness height of the completed surface was taken as 0.1 inches; for the treated channel the Manning coefficient is 0.017 .

Modification of the test facility to incorporate additional combinations of curves would have entailed great additional expense. Therefore, the effects of varied channel alignment were studied through simulation of the flow disturbances caused by curvature in the approach

channel. For this purpose, sets of screen baffles were installed in the upstream tangent. The different screen combinations were established by trial and error to produce the desired flow patterns at the entrance to the curve. A typical screen arrangement is shown in Figures A-4 and A-5, Appendix A.

2. Operating Conditions

For each desired depth condition, the discharge at uniform flow was calculated from the Manning equation. During the early tests in the smooth channels the Manning coefficient was assumed as $n = 0.009$. As the test program continued the channel resistance could be checked, and it was found that the proper value for the plastic finish was $n = 0.010$. A similar trial procedure in the rough channel gave the Manning coefficient, $n = 0.017$.

With the proper discharge flowing in the channel, the sluice gate was employed to adjust the depth at the entrance to the curve. This downstream control was necessary because of the backwater effects of the channel outfall which, before its installation, had been observed to extend through the curve and well into the approach tangent.

Flow uniformity had little significance in the tests on the simulated curve systems due to the large scale modification of the flow pattern produced by the screens. For these tests, therefore, the discharges and sluice gate settings were those established for the corresponding tests at uniform approach condition.

B. Instrumentation

1. The Measurement of Boundary Shear Stress

a. General Requirements: The basic objective of this study involved the mapping of boundary shear intensities in the curved test reach at varied conditions of flow. Thus, the primary requirements of the shear instrument to be used were that it be readily movable and that it have a rapid response.

Because of the secondary currents in the bend region, it was further necessary that the instrument be insensitive to moderate variations in the direction of flow. Local velocities close to the boundary in a bend possess lateral as well as longitudinal components, and consequently the boundary shear stresses are also skewed with respect to the channel centerline. For moderate skewness however (e.g. less than 20 degrees), the magnitudes of the local velocities and boundary shear stresses may be taken as equal to their downstream components. Thus, local shear magnitudes may be adequately determined with an instrument aligned parallel to the downstream direction, provided the instrument itself is not subject to appreciable error arising from lateral components of flow.

A discussion of methods of determining local shears is given in Appendix C; each of the techniques listed was reviewed in terms of the requirements of this study.

b. Shear Measurement by Surface Pitot Tubes: Of the various means available for the measurement of boundary shear stress the surface Pitot tube technique developed by Preston (37) was found to be best suited to the purposes of this study. By this method, the shear stress on a smooth boundary is computed from the dynamic pressure registered by a round

Pitot tube resting on the surface. Preston demonstrated that, for a tube of sufficiently large diameter, the effects of the viscous sublayer become negligible, and the mean total pressure over the face of the tube is dependent only on the velocity distribution in the turbulent boundary layer.

The velocity distribution in the turbulent boundary layer over a smooth surface can be expressed,

$$\frac{u}{u_*} = f\left(\frac{u_* y}{\nu}\right) ; \quad u_* = \sqrt{\frac{\tau_o}{\rho}} . \quad (3)$$

Preston developed the functional groupings by which the shear stress at the wall, τ_o , could be expressed as a dependent variable, and by direct calibration in pipe flows obtained the equation,

$$\log \frac{\tau_o d^2}{4\rho\nu^2} = -1.396 + 0.875 \log \frac{(p_t - p_o)d^2}{4\rho\nu^2} \quad (4)$$

valid within the range, $4.5 < \log \frac{(p_t - p_o)d^2}{4\rho\nu^2} < 6.5$.

Here ρ and ν are the density and kinematic viscosity of the fluid, and $(p_t - p_o)$ is the dynamic pressure recorded by a round Pitot tube of outer diameter = d . This calibration equation depends on the velocity distribution near the wall which was found to be expressible as the power law,

$$\frac{u}{u_*} = 8.61 \left(\frac{u_* y}{\nu}\right)^{1/7} \quad (5)$$

Although Preston developed Equation (4) for a set of Pitot tubes of constant ratio of inner to outer diameters, Hsu (18) later showed, both analytically and by experiment, that, for a tube of given outer diameter, the internal

diameter has negligible effect on the Pitot tube calibration.

Equation (4) was verified by both Preston and Hsu on flat surfaces under varied pressure gradients. For the present open channel work, the calibration was first checked directly in a tilting glass flume. In the curve of the trapezoidal test channel, however, direct calibration was not possible because of the non-uniformity of the flow. In order to establish the validity of Equation (4) for this application, velocity profiles in the flow immediately adjacent to the boundary ($y < 1$ cm) were taken at various points in the curve. By this method the existence of the velocity distribution given by Equation (5) was established (see Figure A-11, Appendix D); therefore, the validity of Equation (4) could be assumed, subject to the restriction that the surface Pitot tube lie wholly within the established boundary layer region of similarity.

For the rough boundary tests, a surface Pitot calibration was developed, which had been suggested in principle by Preston. In turbulent flow over a hydraulically rough surface, the velocity distribution being independent of Reynolds number may be expressed,

$$\frac{u}{u_*} = f_a \left(\frac{y}{k} \right), \quad (6)$$

where k is the absolute height of the boundary protrusions. Thus, by dimensional considerations alone, the expression analogous to Equation (4) becomes,

$$\frac{\tau_o}{(p_t - p_o)} = f_b \left(\frac{d}{k} \right) \quad (7)$$

On the non-uniform surfaces encountered in general practice,

direct application of Equation (7) would be questionable, due to the uncertainty of consistent Pitot tube placement. Furthermore, from analysis of Nikuradse's rough surface velocity data (33), it seems clear that f , in Equation (7), should vary with the value of y_0/k .

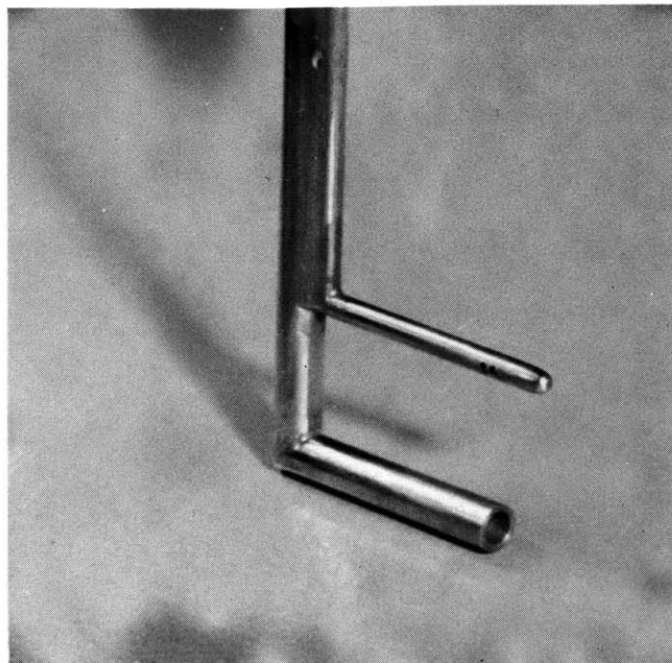
If, however, tests are conducted over a limited range of y_0/k on a surface of sufficiently uniform roughness, then it should be possible to find a single form of Equation (7). Direct calibration of a round Pitot tube was performed in a tilting flume on an artificially roughened surface, identical to that which was later used in the test channel. The test conditions were: $d = 0.432$ ", $k = 0.1$ ", $2'' < y_0 < 6$ ", for mean velocities ranging up to 5 fps. The empirical equation obtained,

$$\tau_0 = 0.021 (p_y - p_0), \quad (8)$$

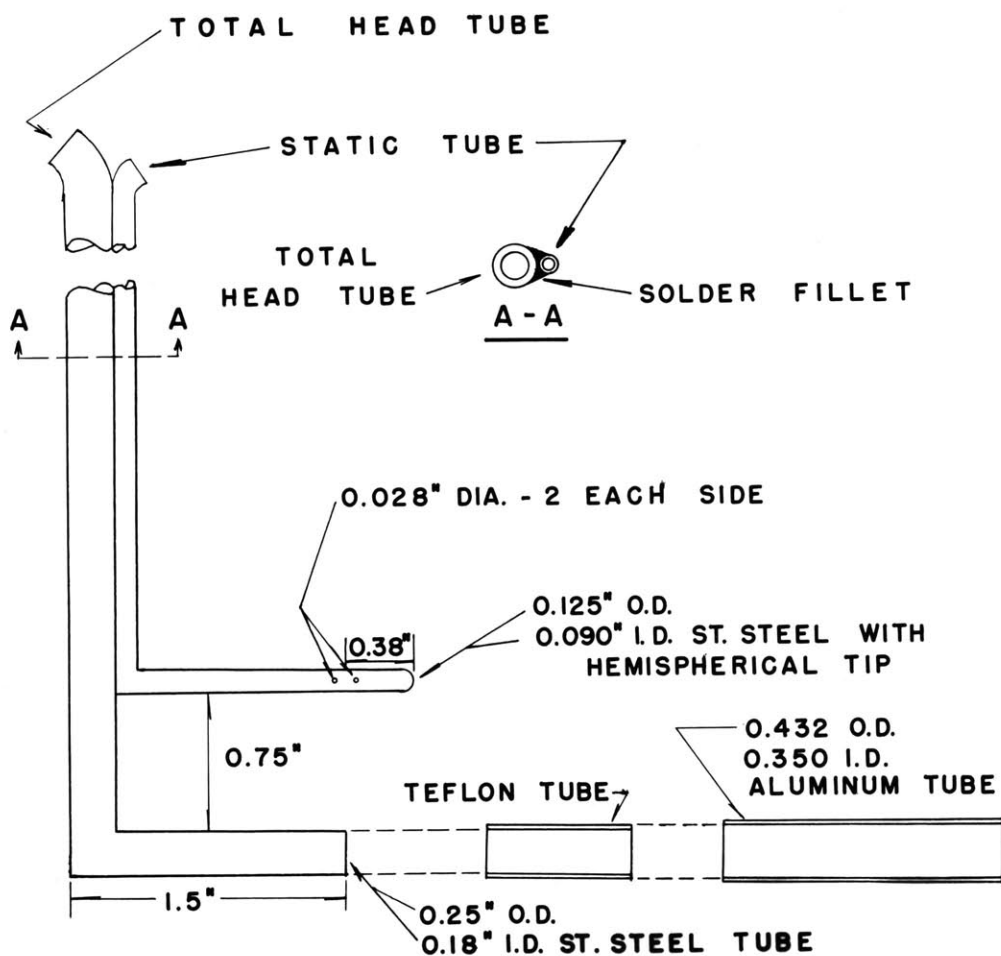
is valid only for the above set of conditions. Since the calibration was performed with only one Pitot tube, the general dimensionless expression, Equation (7), was not established, and the restricted form, Equation (8), is to be preferred.

An extended discussion of the principles underlying the use of surface Pitot tubes, together with calibration procedures is presented in Appendix D.

c. Experimental Application: (i) Smooth Surface. Various models of surface Pitot tubes, which are described in Appendix B, were employed during the tests. The final version, designated as the Model III instrument, is shown in Figure 4. The static tube is positioned above the total head tube in order to minimize the effects of the total pressure gradient near the boundary on the measured static pressure. Before final



(a.) Instrument Mounted on Flat Surface.



(b.) Construction details showing the cylindrical sleeve adapter for the Model III - A Rough Surface Tube.

Figure 4. Model III Surface Pitot Tube

assembly of the instrument it was determined that the two tubes exert no mutual interference, and that the pressure in the channel curve is hydrostatically distributed over the depth of flow. The two leads from the instrument are connected to a manometer to give the desired dynamic head, $(p_t - p_o)/\gamma$.

To measure the boundary shear stress at a point, the instrument is mounted vertically with the total head tube aligned parallel to the downstream direction and the tip resting on the boundary. The shear value is computed from Equation (4) using the dynamic head as read from a manometer. Because each test involved about 200 readings, it was expedient to re-arrange and plot Equation (4) to give a direct graphical solution of τ_o . (See Figure A-12, Appendix D).

In preliminary tests it was found that the instrument is quite insensitive to moderate misalignment of the probe axis with the local direction of velocity. For deflection angles up to 20° , the error in measured shear stress varies essentially as $(1 - \cos \alpha)$; at $\alpha = 20^\circ$ the error is 6%, and at $\alpha = 15^\circ$ the error is about 3%. Dye traces in the channel curve revealed a maximum angularity of the flow of about 20° , which is confined however to a very thin zone adjacent to the boundary.

(ii) Rough Surface. For the measurement of shear stress on the rough test surface, the Model III tube was fitted with the adapter sleeve and bushing shown in Figure 4 which raised the diameter of the impact tube to 0.432 inches. This was done in order to increase the value of the manometer readings obtained, as well as to reduce the effects of local disturbances due to the individual roughness particles. The procedure for measuring shear stress with the modified instrument is essentially the same as the smooth surface technique, the value of τ_o being computed in

this case from Equation (8).

2. Additional Instrumentation

a. Pressure Measurements: Pressures were measured with the two manometers described in Appendix B and shown in Figures A-8 and A-10. The manometers could in general be used interchangeably, depending on the range and precision required. The inclined manometer, being the faster and more convenient of the two, was used in most of the work. The micromanometer was necessary to measure head differentials outside of the range of the inclined manometer and for those cases where absolute pressures were required.

b. Depth Measurements: Depths of water in the channel were measured with a point gauge mounted on the instrument carriage. In certain of the tests it was more convenient to determine depths from static pressure measurements which were correlated with the centerline depths as determined from the point gauge readings.

c. Velocity Measurements: Stream velocities were measured with a 5/16-inch Prandtl Tube. The instrument was always aligned parallel to the downstream component of flow, and no attempt was made to determine the lateral velocity components.

IV. THE EXPERIMENTAL PROGRAM

A. Scope of the Study

The tests were conducted in the two channels shown in Figures 3a and 3b, covering the range of flow geometries which is summarized in Tables I and II.

With the exception of Runs 10-13, the flow entering the curve was essentially uniform and symmetrical about the centerline. For purposes of discussion, therefore, it is convenient to consider Runs 1-9 as comprising one test series covering a broad range of boundary geometries for the simple configuration of a curve with straight tangents. Runs 1-7 comprise the complete series of smooth surface, single curve tests; for Runs 8 and 9, the channel roughness was increased and flows were studied for stream geometries similar to those in Runs 2 and 4.

In Runs 10-13, the velocity distribution in the approach flow was modified through installation of various combinations of baffle screens. By superposing asymmetrical conditions on the entrance flow it was possible to simulate the effects of varied upstream channel alignments. Tests at two depths were conducted to determine the shear pattern in a sequent bend of a double series (U-configuration), and a reverse series (S-configuration) of curves.

During the course of the test series various modifications were made in the design of the surface Pitot tube. The classification of instrument models, as listed in Table II, is given with a description of the instruments in Appendix B. In order to establish that the measured distributions of relative shear were not influenced by the specific model designs, the shear measurements were completely re-taken with

TABLE I

Summary of Channel Geometries Covered in the Test Program.

Run No.	Nominal Stream Dimensions		Channel Dimensions	Boundary Roughness	Velocity Distribution in Approach Flow
	$\frac{w}{y_0}$	$\frac{w}{r_c}$			
1	12	0.60	} $b/r_c = 0.40$ Fig. 3a	} Smooth } $n = 0.010$	} Symmetric; Single curve with straight tangents.
2	10	0.67			
3	8.8	0.73			
4	8	0.80			
5	10	0.29	} $b/r_c = 0.17$ Fig. 3b	} Rough } $n = 0.017$	
6	8	0.34			
7	7	0.40			
8	10	0.67	} $b/r_c = 0.40$ Fig. 3a	} Smooth } $n = 0.010$	} Asymmetric; Flow pattern modified to simulate up- stream curvature.
9	8	0.80			
10	10	0.67			
11	8	0.80			
12	10	0.67			
13	8	0.80			

TABLE II

Summary of Test Conditions Determined in the Approach Flow (Station 1).

Run No.		1	2-A; 10; 12	2-B	3-A; B	4-A; 11; 13	4-B	5	6	7	8**	9**
y_o	in	2.98	3.86	4.00	5.08	6.00	5.99	2.01	3.02	3.98	3.94	6.04
A	sf	0.620	0.850	0.889	1.210	1.500	1.498	0.223	0.378	0.550	0.889	1.463
R	ft	0.199	0.246	0.255	0.311	0.354	0.354	0.127	0.177	0.222	0.249	0.337
w	in	35.92	39.44	40.00	44.32	48.00	47.96	20.04	24.08	27.92	40.70	49.10
y_m	ft	0.208	0.259	0.267	0.326	0.375	0.375	0.134	0.188	0.236	0.262	0.357
r_o/w		2.17	2.02	2.00	1.86	1.75	1.75	4.00	3.41	3.01	1.97	1.73
w/y_o		12.05	10.21	10.00	8.72	8.00	7.99	9.98	7.98	7.02	10.32	8.13
Q	cfs	0.85	1.27	1.26	2.02	2.86	2.00	0.19	0.45	0.77	0.84	1.77
V	fps	1.36	1.50	1.43	1.67	1.91	1.33	0.87	1.19	1.40	0.94	1.18
F		0.53	0.52	0.49	0.52	0.55	0.38	0.42	0.48	0.51	0.32	0.34
$R \times 10^{-5}$		1.21	1.63	1.62	2.31	3.00	2.10	0.44	0.84	1.24	0.94	1.42
$S_e \times 10^5$ *		71	60	64	65	68	32	52	64	66	68	67
$\gamma R S_e \times 10^4$	psf	88	92	102	127	150	70	40	70	88	105	140
$\bar{\tau}_o \times 10^4$	psf	70	87 81	88	101 121	148 123	60	34	55	74	85	120
Surface Pitot Tube Model		II	I III	II	III II	II III	II	III	III	III	III-A	III-A

*The bottom slope, S_o , is assumed as 0.00064 in all but Runs 5-7; in Runs 5, 6, 7, $S_o = 0.00055$.

**The slight difference in geometries between these and the corresponding smooth surface runs is due to the installation of the rough surface material.

different instruments. Comparison of the shear distributions for Run 2-A (Model I) with 2-B (Model II), and Run 3-A (Model III) with 3-B (Model II), showed that, while the absolute magnitudes of the local shears varied with the model used, there were no essential differences in the maps of relative shear given in terms of the mean shear stress measured at Station 1, $\overline{\tau_0}$.

In performing the runs on the simulated curve systems with the Model III tube, it was simply necessary, on the basis of the above tests, to re-measure the shear distribution at Station 1 and then to apply the relative shear data as computed previously. Thus the second value of $\overline{\tau_0}$ given in Table II for Run 2-A and for Run 4-A, represents the measurement with the Model III instrument, which was used in the corresponding compound **curve** tests.

It will also be noticed that while two tests were conducted at a 6 inch depth, the energy gradient, mean velocity, and hence the shear stress of the approach flow were varied markedly between the two runs. Unlike Runs 2 and 3 which were repeated at similar conditions in order to verify the experimental techniques, Runs 4-A and -B represent essentially different tests. The purpose of these tests, which are discussed in a later section, was to study the effect of approach flow non-uniformity on the shear pattern in the curve.

For all of the tests boundary shear stresses were measured at the ten test stations indicated in Figures 3a and 3b. Highly non-uniform shear patterns in several of the runs made it necessary to add two intermediate sections between Stations 7 and 8. Shear measurements were taken at 2" intervals across each station, covering the full wetted perimeter except the outer 4" along each side.

Complete measurements of water surface elevations and local

velocities were made at each station in Runs 1-4. As the test program progressed coverage of these variables was decreased in order to limit the amount of data to be processed. At all depths, however, sufficient data were taken to indicate the gross characteristics of water surface superelevation and velocity distribution.

It should be mentioned that the numbering system of the test runs shown in Table I was established to give a logical sequence to the order of discussion, and that it does not follow the chronological order of the experiments. All of the tests involving the larger smooth channel (Figure 3a) were completed before application of the rough surface. Following the completion of the two tests on the rough surface, the channel was modified to give the flume arrangement shown in Figure 3b, and the final three tests were those conducted in the smaller smooth surfaced channel.

B. Presentation of Data

The volume of the basic data compiled during the course of this study is such that direct presentation of the tabulated material would make analysis difficult. Therefore, in order to facilitate the discussions of the results, the data presented herein have been reduced to graphical form. The complete compilation of tabulated data has been printed and is available in the basic data supplements of Hydrodynamics Laboratory Technical Report No. 43 (19) and No. 47 (to be released January 1962).

The data figures for the various tests are presented in the appropriate discussion sections in the following text. Before proceeding with the discussions, however, it is convenient to define the method of

presentation of each group of data.

1. Velocity and Water Surface Profile Data.

The velocity distributions and transverse surface profiles are presented by stream sections following the sequence of test stations in the curved reach. Because of the repetitive nature of these patterns drawings were prepared only for representative tests.

2. Boundary Shear Stress Data.

The value of the mean measured shear stress at Station 1, $\overline{\tau}_0$, was determined for each test by graphical integration of a plot of the local shear stress, τ_0 , over the wetted perimeter;

$$\overline{\tau}_0 = \frac{1}{P} \int_P \tau_0 dP]_{\text{Sta. 1}} \quad (9)$$

The maps of boundary shear distribution for the full test series are presented in terms of relative local shear, $\tau_0 / \overline{\tau}_0$. This form is preferable to reporting absolute values, since application of the results is simpler, and the shear patterns for varying flow conditions are readily compared. The absolute magnitudes of local shears may be computed from the shear maps using the values of $\overline{\tau}_0$ (Table I) obtained from Equation (9).

V. DISCUSSION OF RESULTS

A. Tests Conducted with Uniform Conditions of Approach: Flow Through Single Curves

1. Smooth Channel, Runs 1-7.

a. Entrance Conditions. For the series of tests conducted in the smooth channels with undisturbed approach conditions, the velocity, water surface and shear stress configurations at the entrance to the test section are essentially symmetrical about the centerline axis (Figures 5-10). At conditions of greater relative curvature and depth a slight asymmetry becomes evident at Station 1 due to the backwater effects of the curve. It seems clear however that the flow pattern in the bend cannot be ascribed to upstream distortion of the flow.

The existence of a fully developed turbulent boundary layer was desired at the entrance to the curve. The boundary layer thickness, δ , may be approximated by the Blasius expression, assuming turbulent conditions from the channel entrance, $x = 0$;

$$\frac{\delta}{x} = \frac{0.38}{\left(\frac{Vx}{\nu}\right)^{1/5}} \quad (10)$$

Substitution of the values, $V = 1.50$ fps and $\nu = 10^{-5}$ ft²/sec, gives $\delta = 4.6$ inches at $x = 20$ feet. Because of the relatively small variation in Reynolds numbers, the boundary layer thickness varied only a small amount over the full set of flow conditions. Thus the boundary layer was fully developed in Runs 1-2 and 5-7, and essentially so for the 5-inch and 6-inch depths, Runs 3 and 4.

Because the low channel slope made it impossible to obtain the energy gradient accurately, it is not known to what extent fully uniform

V. DISCUSSION OF RESULTS

A. Tests Conducted with Uniform Conditions of Approach: Flow Through Single Curves

1. Smooth Channel, Runs 1-7.

a. Entrance Conditions. For the series of tests conducted in the smooth channels with undisturbed approach conditions, the velocity, water surface and shear stress configurations at the entrance to the test section are essentially symmetrical about the centerline axis (Figures 5-10). At conditions of greater relative curvature and depth a slight asymmetry becomes evident at Station 1 due to the backwater effects of the curve. It seems clear however that the flow pattern in the bend cannot be ascribed to upstream distortion of the flow.

The existence of a fully developed turbulent boundary layer was desired at the entrance to the curve. The boundary layer thickness, δ , may be approximated by the Blasius expression, assuming turbulent conditions from the channel entrance, $x = 0$;

$$\frac{\delta}{x} = \frac{0.38}{\left(\frac{Vx}{\nu}\right)^{1/5}} \quad (10)$$

Substitution of the values, $V = 1.50$ fps and $\nu = 10^{-5}$ ft²/sec, gives $\delta = 4.6$ inches at $x = 20$ feet. Because of the relatively small variation in Reynolds numbers, the boundary layer thickness varied only a small amount over the full set of flow conditions. Thus the boundary layer was fully developed in Runs 1-2 and 5-7, and essentially so for the 5-inch and 6-inch depths, Runs 3 and 4.

Because the low channel slope made it impossible to obtain the energy gradient accurately, it is not known to what extent fully uniform

00000

flow was achieved. However, it is believed that this condition is not of great consequence for the results of this study. It will be noted that Runs 4-A and B represent the largest variation in F and S_e , yet the contours of $\tau_0 / \bar{\tau}_0$ for these tests were found to be virtually identical. Thus, while the magnitude of the mean shear stress varies essentially as the mean velocity head, the distribution of relative shears is but little affected by variations in the Froude number and energy gradient of the approach flow.

b. Flow through the Curve. The flow through the channel bend exhibits the expected tendency towards free vortex motion, and in the upstream portion of the curve (Stations 3-5) the velocity patterns and water surface configurations are in general agreement with those found by previous investigators (31)(39). For the full range of conditions tested the maximum total water surface superelevations (See Section V-C below) as well as the surface profile shapes (Figures 8 and 9) conform quite closely to the trend predictable for free vortices.

The irrotational aspects of the flow are most pronounced at conditions of greatest depth and curvature. In Runs 1-4, the irrotational type of motion persists over the full length of the curve, and high velocities appear along the outer bank only at the start of the downstream tangent. (Figures 5 and 6). However, at decreased curvature (Figure 7), the transfer of higher velocities towards the outer bank is quite evident throughout the second half of the curve, and below Station 5, the irrotational pattern is suppressed.

Attention is called here once more to the phenomenon previously discussed which are not readily apparent from the plots of velocities and surface elevation: separation and helicoidal motion.

Figures 5, 6, 7. Velocity Distributions Shown by Section for Condition of Uniform Approach, Smooth Channel.

Figure 5. Run No. 1.

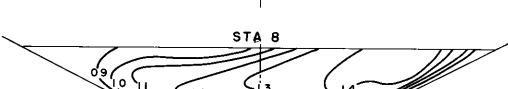
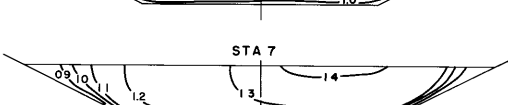
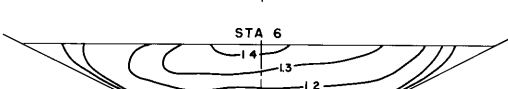
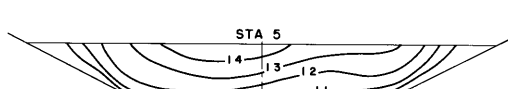
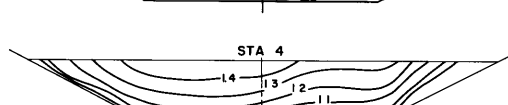
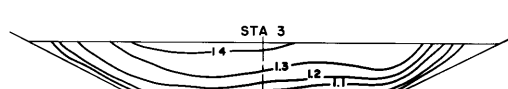
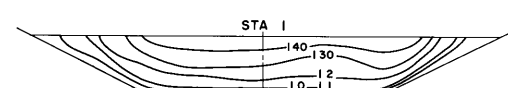
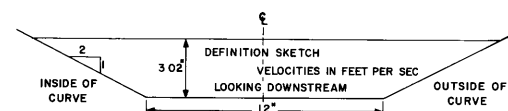
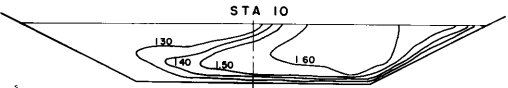
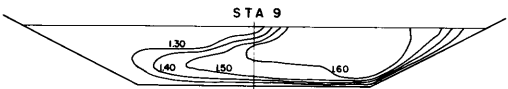
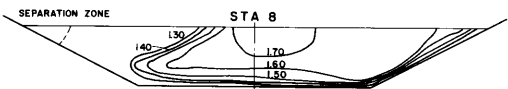
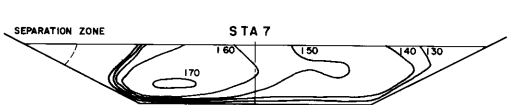
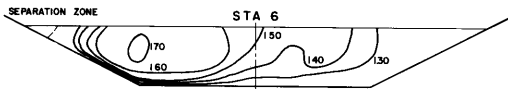
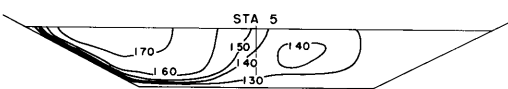
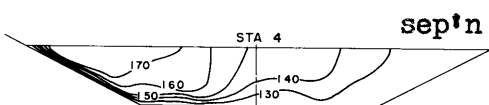
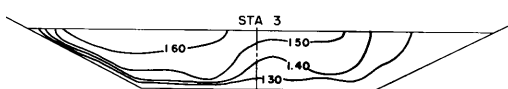
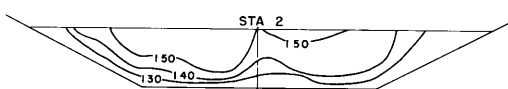
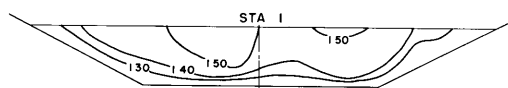
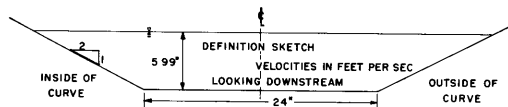
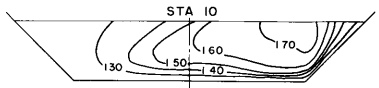
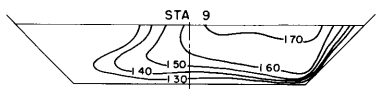
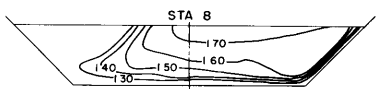
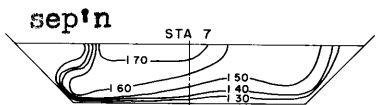
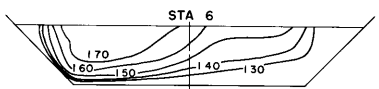
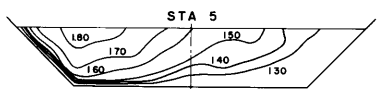
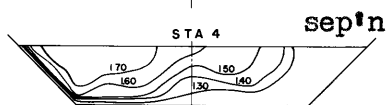
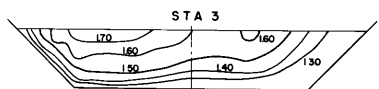
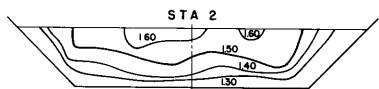
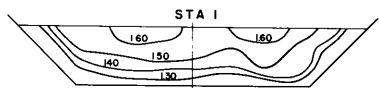
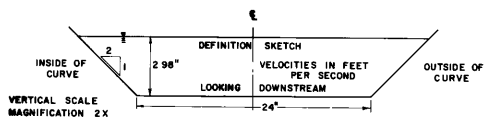
$y_0 = 2.98"$, $w/y_0 = 12$, $w/r_c = 0.6$

Figure 6. Run No. 4-B.

$y_0 = 5.99"$, $w/y_0 = 8$, $w/r_c = 0.8$

Figure 7. Run No. 6.

$y_0 = 3.02$, $w/y_0 = 8$, $w/r_c = 0.34$.



0030

Figs. 5,6,7

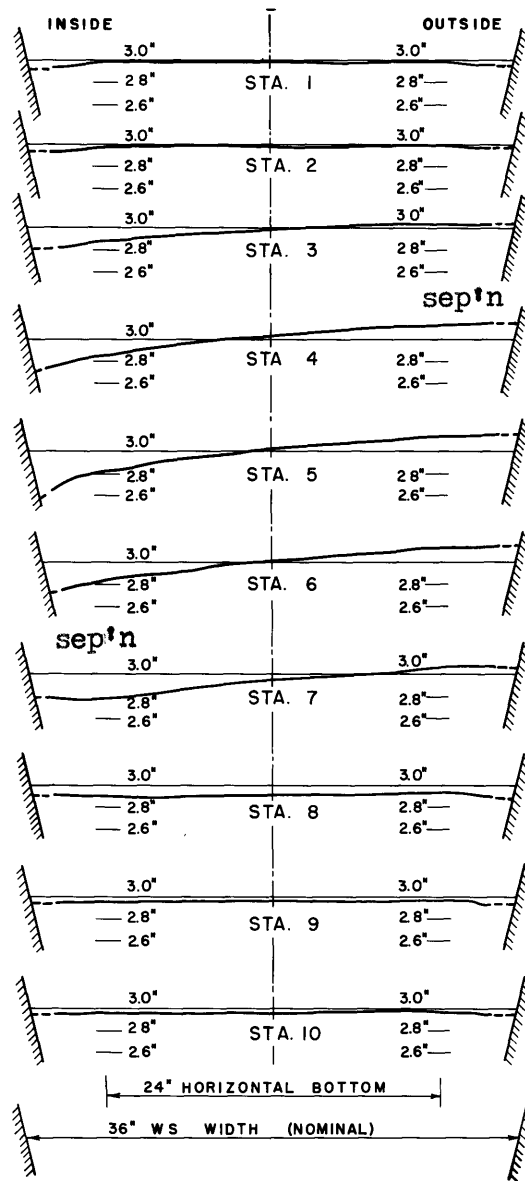


Figure 8. Transverse Water Profiles shown by Section.
Run No. 1: $y_0 = 2.98''$, $b/r_c = 0.42$.

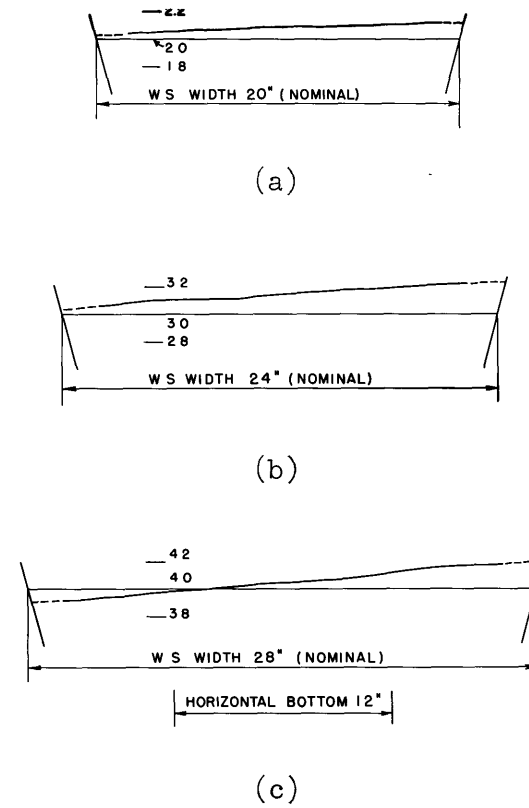


Figure 9. Transverse Water Surface Profiles at Station 5.
(a). Run No. 5: $y_0 = 2.01''$,
 $b/r_c = 0.17$.
(b). Run No. 6: $y_0 = 3.02''$,
 $b/r_c = 0.17$.
(c). Run No. 7: $y_0 = 3.98''$,
 $b/r_c = 0.17$.

04

Figures 1, 5, and 6 indicate the two zones of separation which may occur at the points of locally rising water surface. The zones are manifested by stable areas of reversed flow along the sloping banks. Dye injected into the bank rollers spreads rapidly throughout the separated regions, but is slow to diffuse into the main stream. The presence of these zones depends primarily on the relative curvature of the stream. At conditions of lower curvature and depth, variations in surface elevation are more gradual and are greatly reduced. In Runs 5-7 there could be detected only a vestigial zone on the inner bank, and there was no sign whatever of separation along the outer boundary.

As is shown in Figure 2, a helicoidal pattern, due to the transverse surface gradient, is well developed in the smooth channel. Since lateral components of velocities were not measured, it is not possible to evaluate the effects of bend curvature on the intensity of the spiral currents. However, the spiral velocities are generated by the transverse pressure gradient in the curve and it is to be expected that they should be subject to the same control and thus will vary as the velocity head and relative curvature. The angularity of the flow, which is a measure of the spiral velocities relative to the mean downstream velocity, did not appear to vary greatly over the range of test conditions. In all of the runs, the maximum angular deflection which could be observed from dye traces was about 15° - 20° in a thin zone close to the channel bottom; at $1/2$ " above the bottom, however, the velocities appeared to have little angularity with respect to the curve centerline. The importance of the secondary bottom currents, as related to the shape of the inner separation zone and to sediment transport is demonstrated in Figure 2 by the infusion of dye to the separation zone (lower right hand

corner of photograph) from the bed of the stream.

The ultimate breakdown of the free vortex patterns and the establishment of a high velocity zone near the outer bank are due to two major factors, the relative importance of which depends on the stream curvature.

1. The helicoidal motion tends to move the high velocity fluid continuously toward the outer bank.

2. The separation zone which originates at the inside of the curve reduces the effective area of the section, resulting in acceleration of the constricted stream, and a deflection of the flow away from the inner bank.

In the tests at reduced curvature, Runs 5-7, the first of these factors is clearly dominant. The separation zone remains small yet the high velocities begin to develop along the concave bank midway through the curve.

At higher curvatures, (Runs 1-4), however, the separation zone is strongly developed on the inner bank, and the second effect assumes the greater importance. In addition, because of the relatively shorter length of flow in a sharper curve, the helicoidal motion is not as fully developed, and the momentum transfer by this means is greatly reduced. This dominant action of the separation zone was demonstrated in the tests of the simulated reverse curve systems (Runs 11 and 13) which are discussed in a later section. In the latter tests, which were conducted at conditions similar to those of Runs 2 and 4A, the higher velocities in the entrance flow were diverted towards the inner bank, preventing the formation of the separation zone. Dye traces showed that the helicoidal motion was undiminished, yet for these conditions the high velocity zone

did not develop on the outer bank.

The further persistence of the flow asymmetry in a long straight reach following the curve could not be determined in these tests. The channel was too short to permit a return to normal flow, but, from the similarity between the distributions at Stations 9 and 10, of both velocity and shear, it is evident that such a return would be quite gradual requiring a considerable length of straight channel below the curve. Shukry (39) found that uniform flow is not re-established for a distance of at least eight stream widths, while investigations on pipe bends have shown that the rate of headloss may not return to normal within a length of less than fifty pipe diameters (2)(21). The distance of recovery following a curve is subject to great variation as it depends on the degree of non-uniformity produced by the curve itself. In general it may be surmised that this recovery length will be of the order of the distance required to establish a normal boundary layer.

c. Boundary Shear Stress. The distribution of shear stresses in the approach flow is in general agreement with the results reported by Enger (10) on tests performed in a straight channel of similar trapezoidal section lined with sand-gravel mixtures. In Figure 10, the shear distributions at Station 1 are shown for the complete series of tests in the single curve. For comparison, data from the rough surface tests, Runs 8 and 9, are included, as well as from several of Enger's tests.

The fact that the shears measured in the gravel-lined channel show a somewhat greater scatter emphasizes the difficulties encountered in working with streams through non-homogeneous materials. While the shears measured in both the smooth and rough channels appear quite consistent, it must be borne in mind that, in natural streams, greater

variation is to be expected in the local tractive, or scouring, forces.

The close physical relationship between the boundary shear and velocity patterns is shown by comparison of Figures 5, 6, and 7, with the corresponding shear maps, Figures 11, 14, and 16. That the shear pattern should be governed by the velocity distribution is to be expected.

Beneath a zone of high velocity the gradient of velocity, and hence the local rate of momentum transfer are increased, resulting in higher shear stresses. However, the ability to relate boundary shear stress to local velocities presupposes a rather idealized boundary layer, which may be described by a single velocity distribution function. While such a law is realized for the flow immediately adjacent to the boundary (see Figure A-11, Appendix D), non-uniformity in the curving stream prevents such general formulation for the full depth of flow, and the relation between the shear distribution and the gross velocity patterns can only be considered on a qualitative basis.

Comparison of the shear maps, Figures 11-17, reveals certain trends in the variations in shear patterns with stream geometry. The maps for the tests at greater curvature (Runs 1-4) are essentially similar, showing the higher stresses developed on the inner bank through most of the curve, and on the outer bank only below Station 7. With decreasing curvature the suppression of the free vortex motion becomes more evident in the shear maps. Thus, while high shears occur on the inner bank in Run 7, the crossover of the shear pattern is developed between Stations 5 and 6. In Run 6, the inner bank shears are greatly diminished and the crossover occurs at Station 5, while in Run 5, the asymmetry of the shear pattern in the beginning of the curve is barely perceptible.

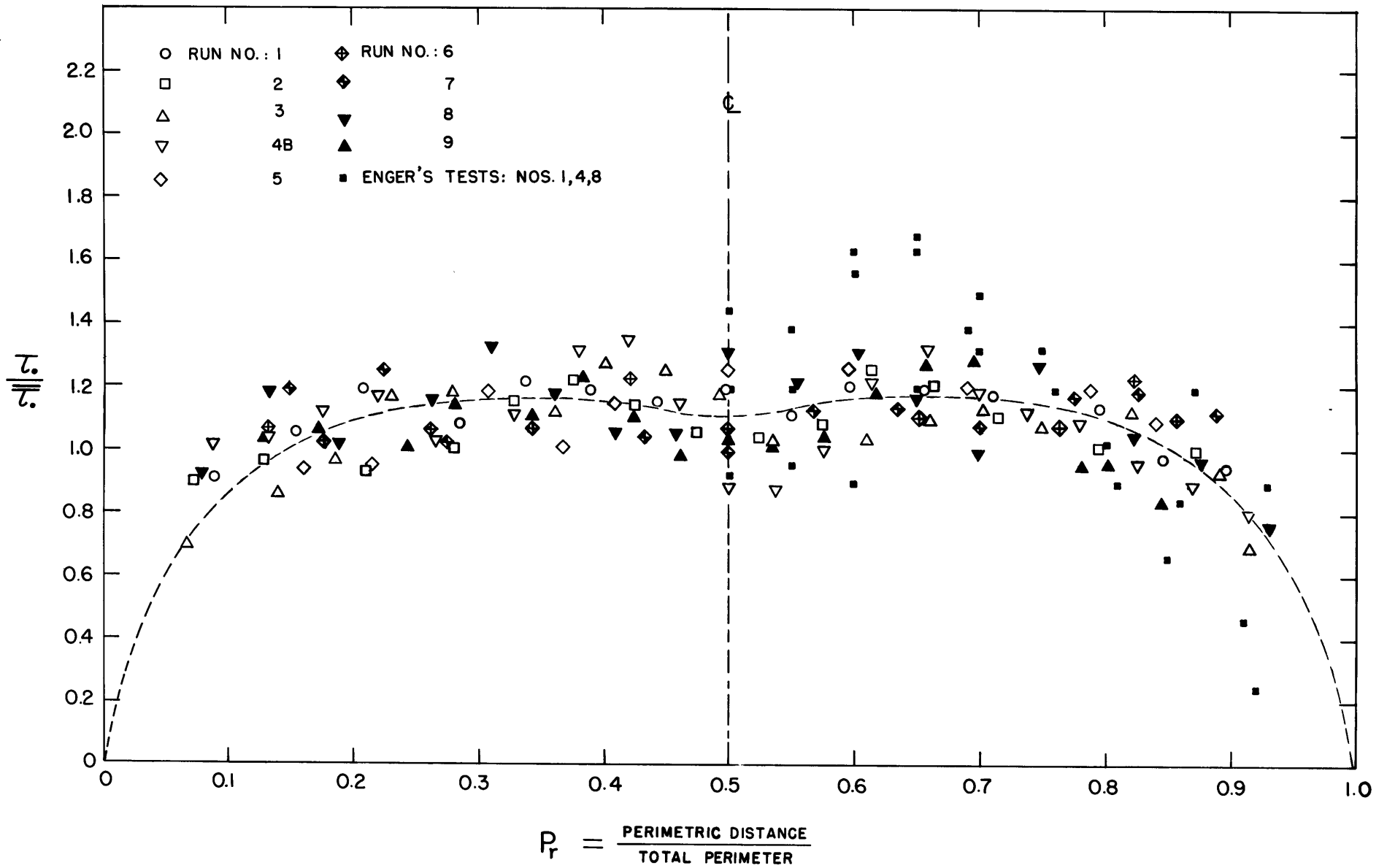


Figure 10. The Peripheral Distribution of Local Boundary Shear Stresses in Straight Trapezoidal Channels (Facing downstream).

Figure 11. The Distribution of Boundary Shear Stresses in the Curved Reach Shown by Contours of $\tau_o/\overline{\tau_o}$;

Run No. 1: smooth channel, $b/r_c = 0.42$, uniform approach, $y_o = 2.98''$, $w/y_o = 12$, $w/r_c = 0.6$, $\overline{\tau_o} = 0.0070$ psf.

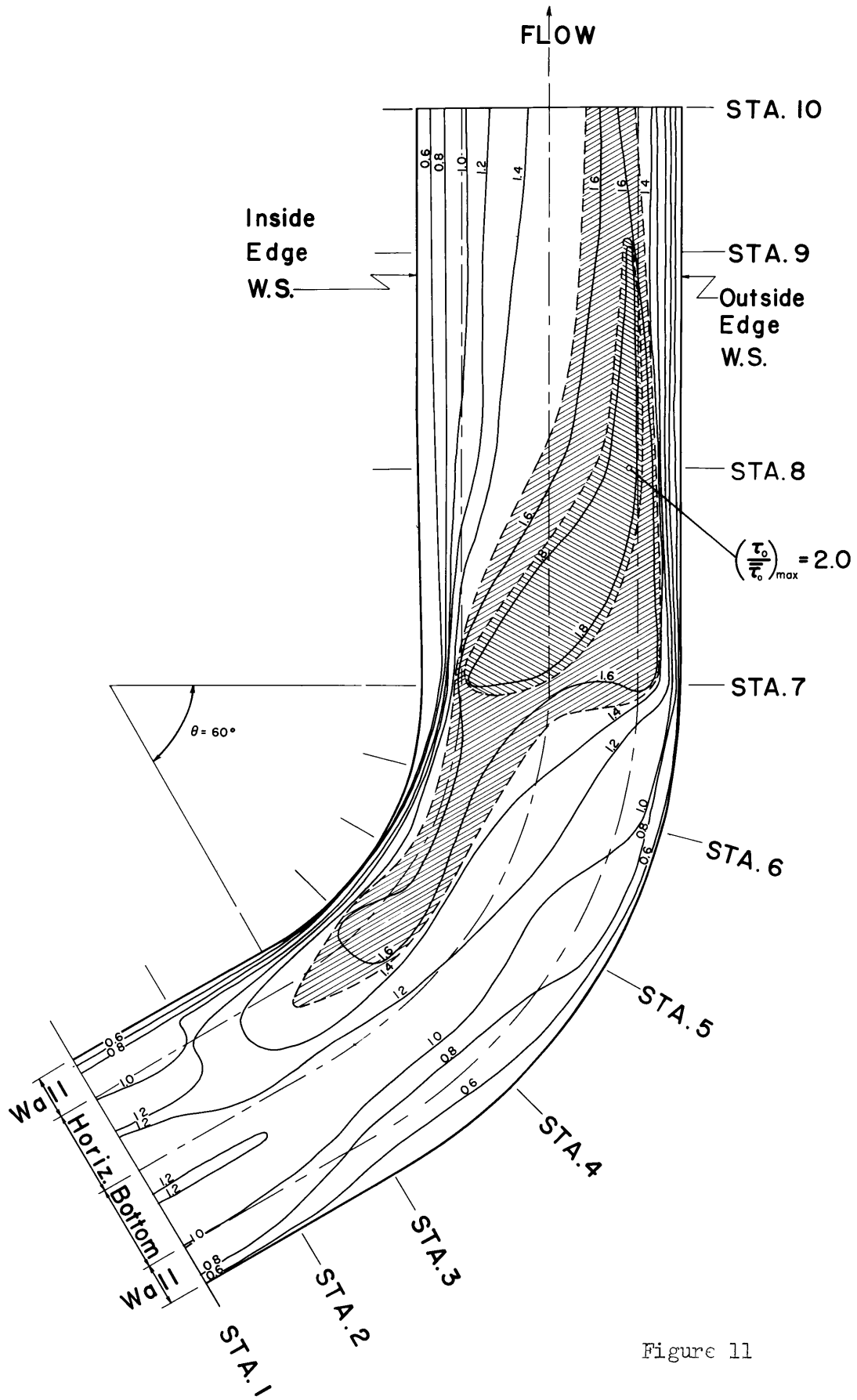


Figure 11

Figure 12. The Distribution of Boundary Shear Stresses in the Curved Reach, Shown by Contours of $\tau_0/\bar{\tau}_0$;

Run Nos. 2-A and B: smooth channel, $b/r_c = 0.42$, uniform approach,
 $w/y_0 = 10$, $w/r_c = 0.67$, (A): $y_0 = 3.86''$,
 $\bar{\tau}_0 = 0.0087$ psf., (B): $y_0 = 4.00''$,
 $\bar{\tau}_0 = 0.0088$ psf.

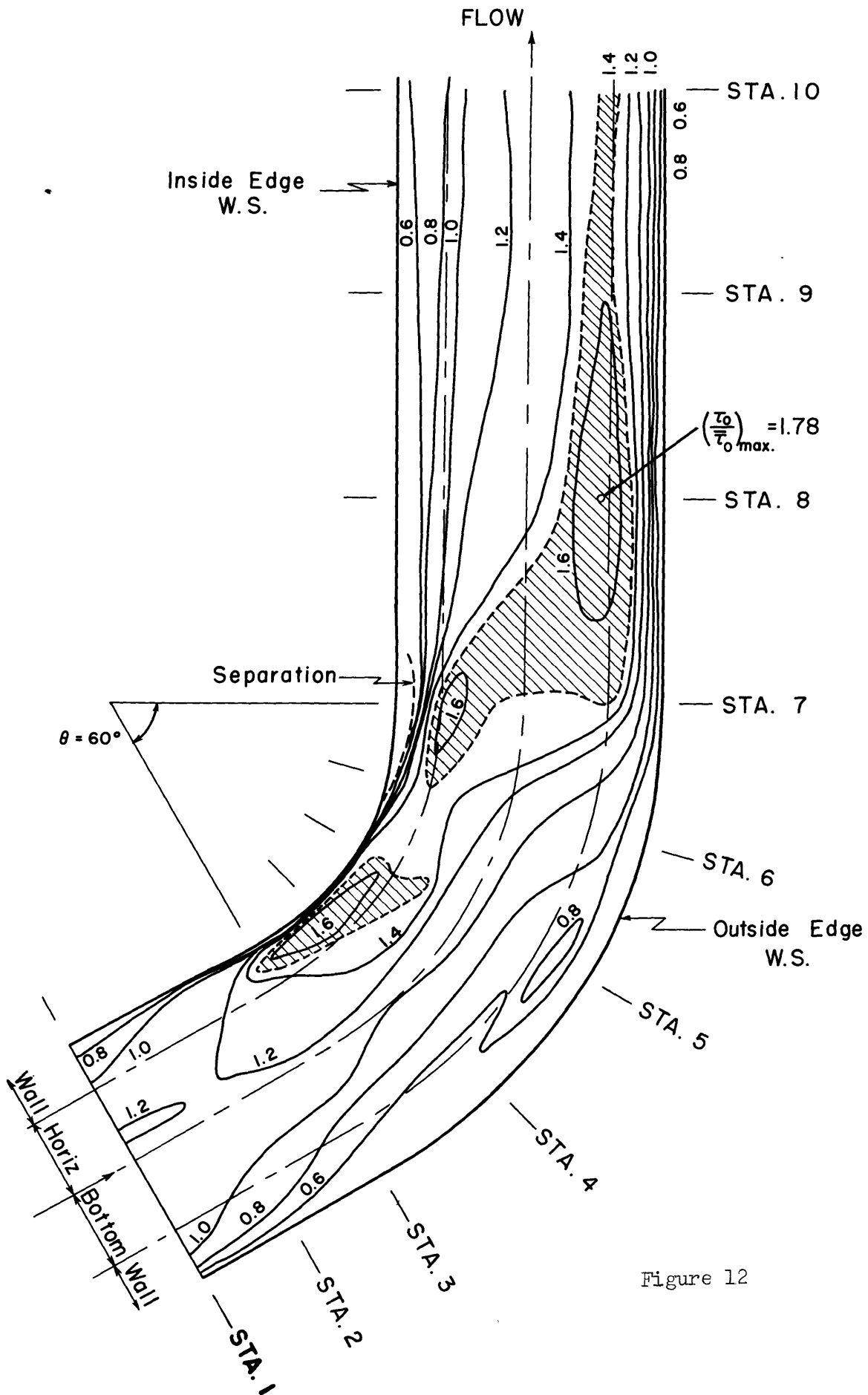


Figure 12

Figure 13. The Distribution of Boundary Shear Stresses in the Curved Reach, Shown by Contours of $\tau_o/\bar{\tau}_o$;

Run Nos. 3-A and B: smooth channel, $b/r = 0.42$, uniform approach,
 $w/y_o = 8.8$, $w/r_c = 0.73$, (A): $y_o = 5.08''$,
 $\bar{\tau}_o = 0.0101$ psf., (B): $y_o = 5.08''$,
 $\bar{\tau}_o = 0.0121$ psf.

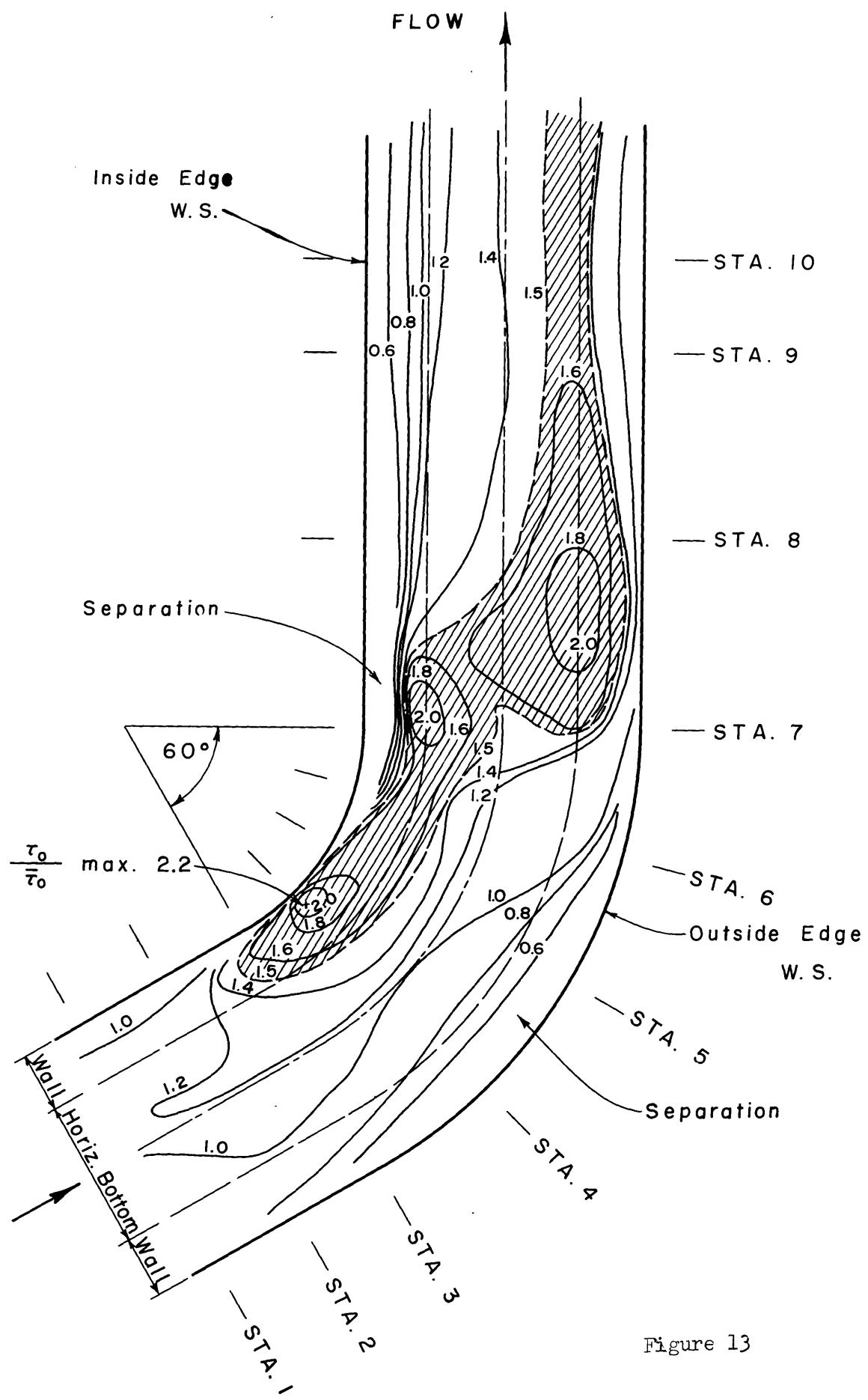


Figure 13

Figure 14. The Distribution of Boundary Shear Stresses in the Curved Reach, Shown by Contours of $\tau_o/\bar{\tau}_o$;

Run Nos. 4-A and B: smooth channel, $b/r_c = 0.42$, uniform approach
 $w/y_o = 8$, $w/r_c = 0.8$, (A): $y_o = 6.00"$,
 $\bar{\tau}_o = 0.0148$ psf., (B): $y_o = 5.99"$,
 $\bar{\tau}_o = 0.0060$ psf.

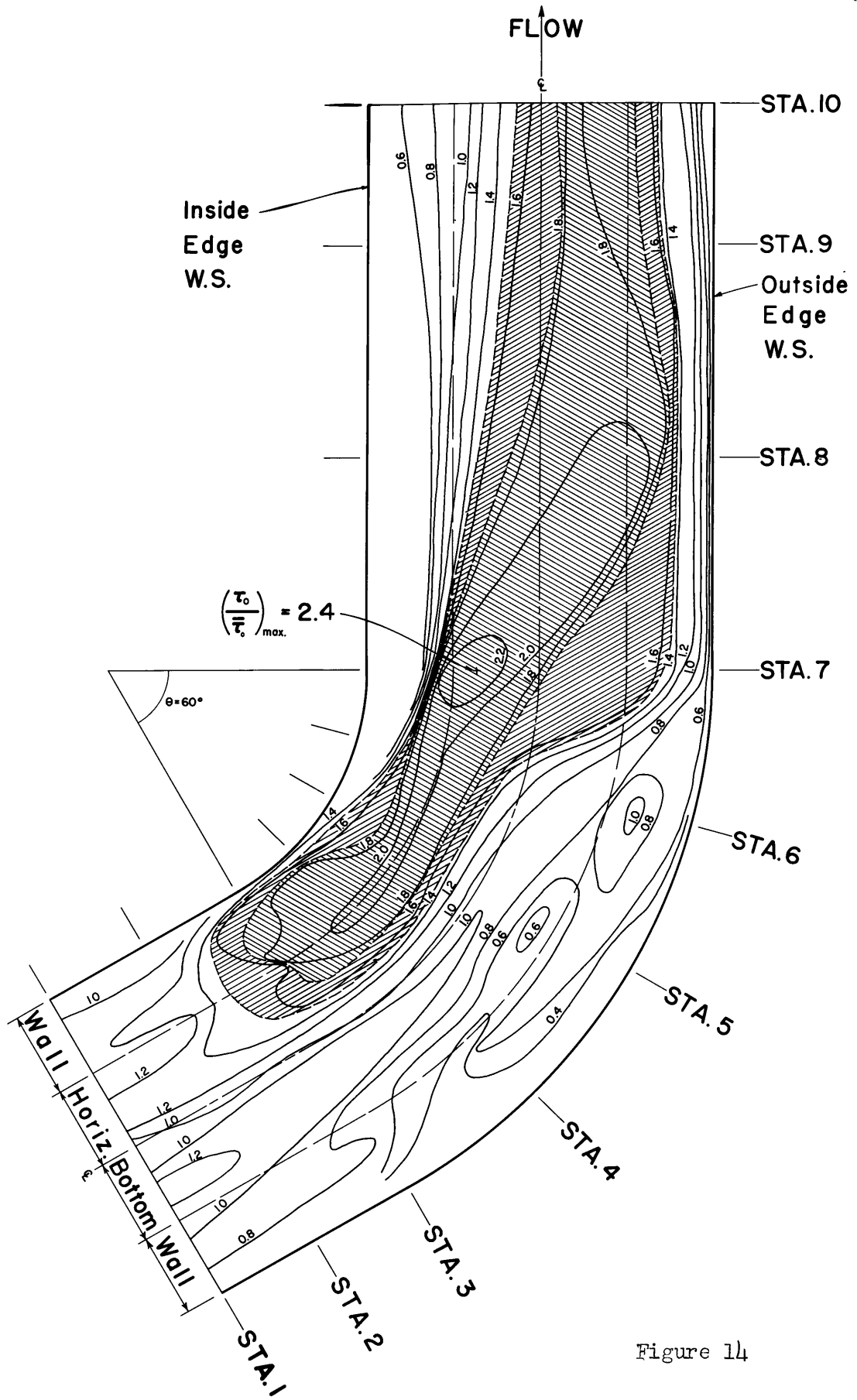


Figure 14

Figure 15. The Distribution of Boundary Shear Stresses in the Curved Reach, Shown by Contours of $\tau_o/\bar{\tau}_o$

Run No. 5: smooth channel, $b/r_c = 0.17$, uniform approach, $w/y_o = 10$,
 $w/r_c = 0.29$, $y_o = 2.01''$, $\bar{\tau}_o = 0.0034$ psf.

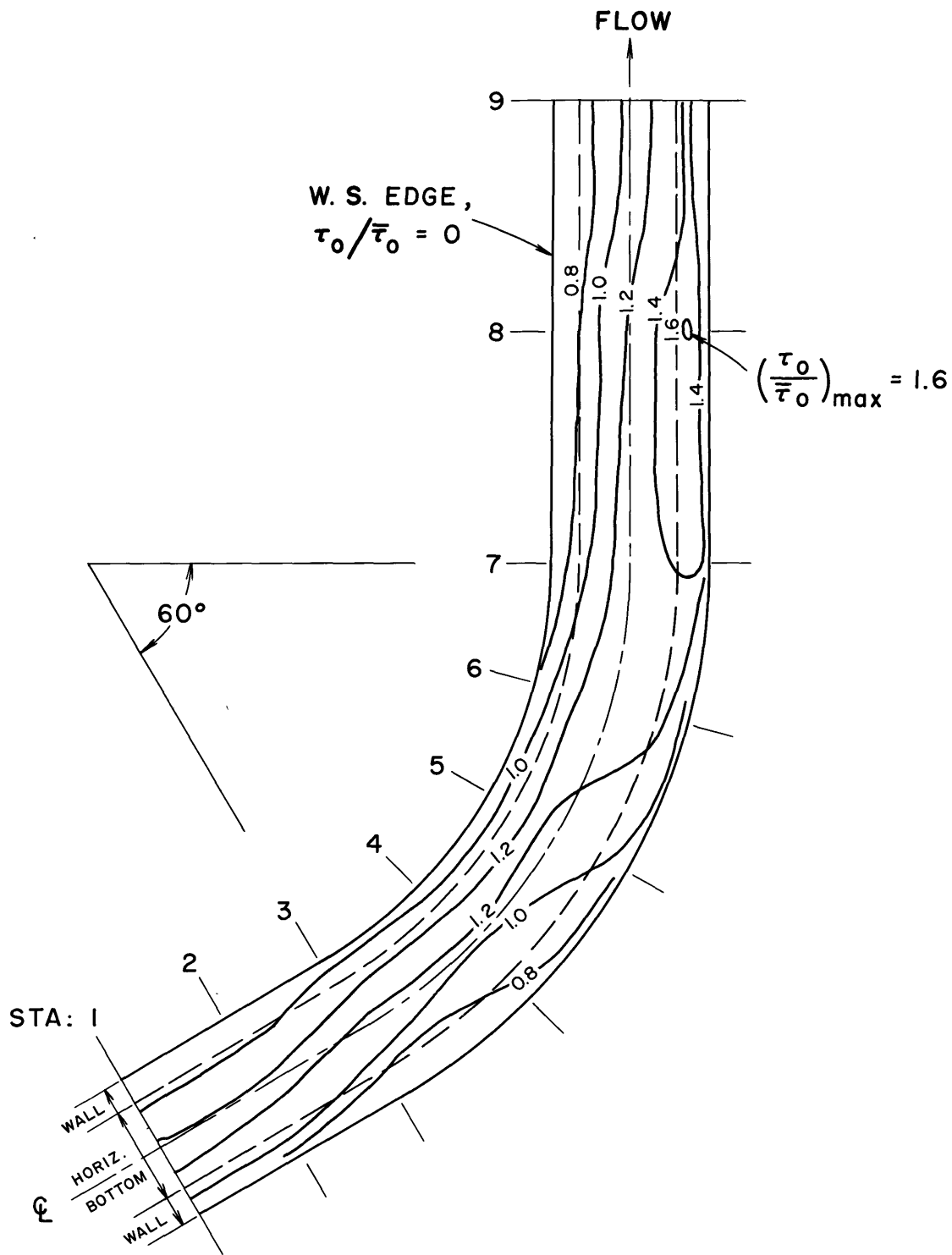


Figure 15

Figure 16. The Distribution of Boundary Shear Stresses in the Curved Reach, Shown by Contours of $\tau_o/\bar{\tau}_o$;

Run No. 6: smooth channel, $b/r_c = 0.17$, uniform approach, $w/y_o = 8$, $w/r_c = 0.34$, $y_o = 3.02''$, $\bar{\tau}_o = 0.0055$ psf.

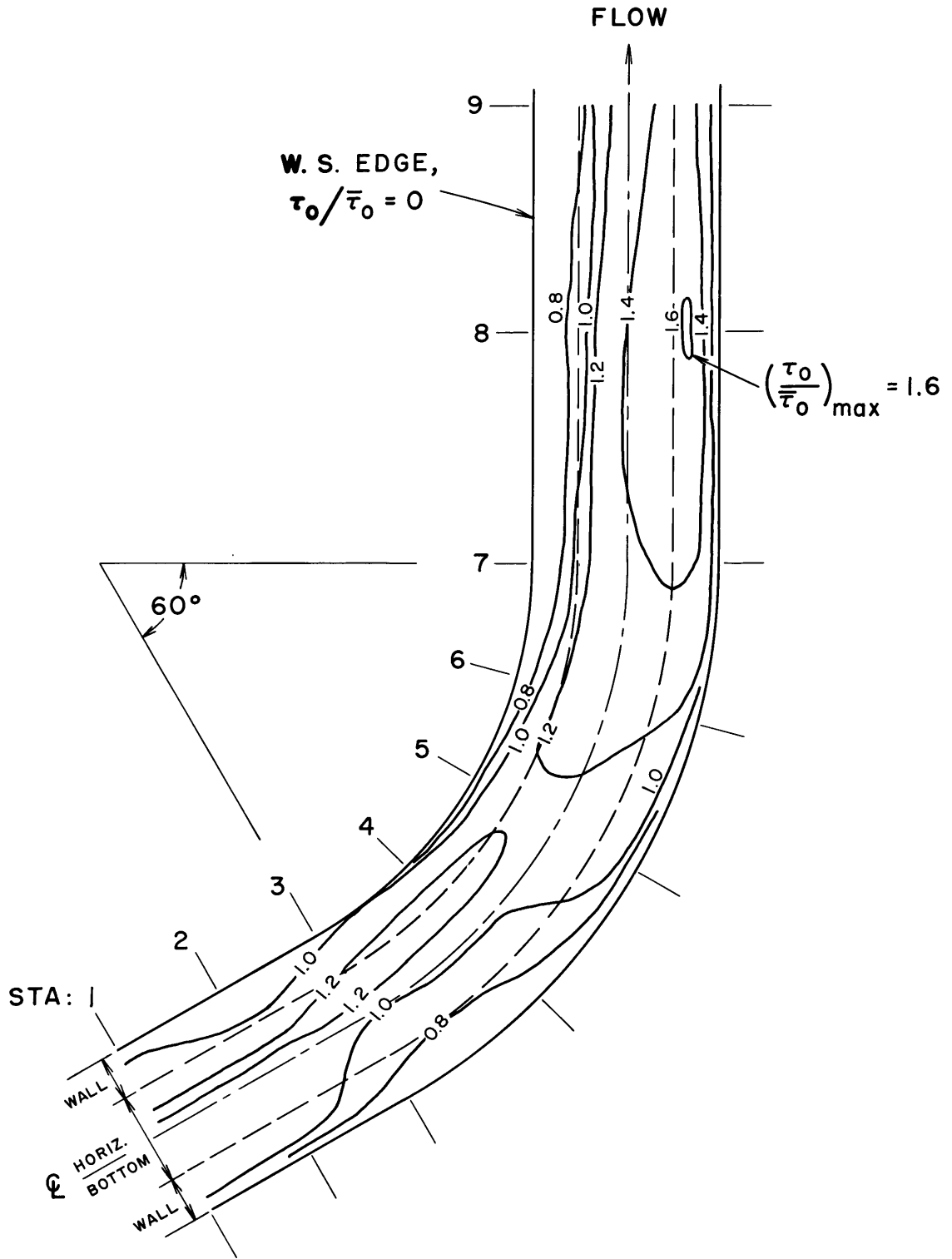


Figure 16

Figure 17. The Distribution of Boundary Shear Stresses in the Curved Reach, Shown by Contours of $\tau_o/\bar{\tau}_o$;

Run No. 7: smooth channel, $b/r_c = 0.17$, uniform approach, $w/y_o = 7$, $w/r_c = 0.4$, $y_o = 3.98''$, $\bar{\tau}_o = 0.0074$ psf.

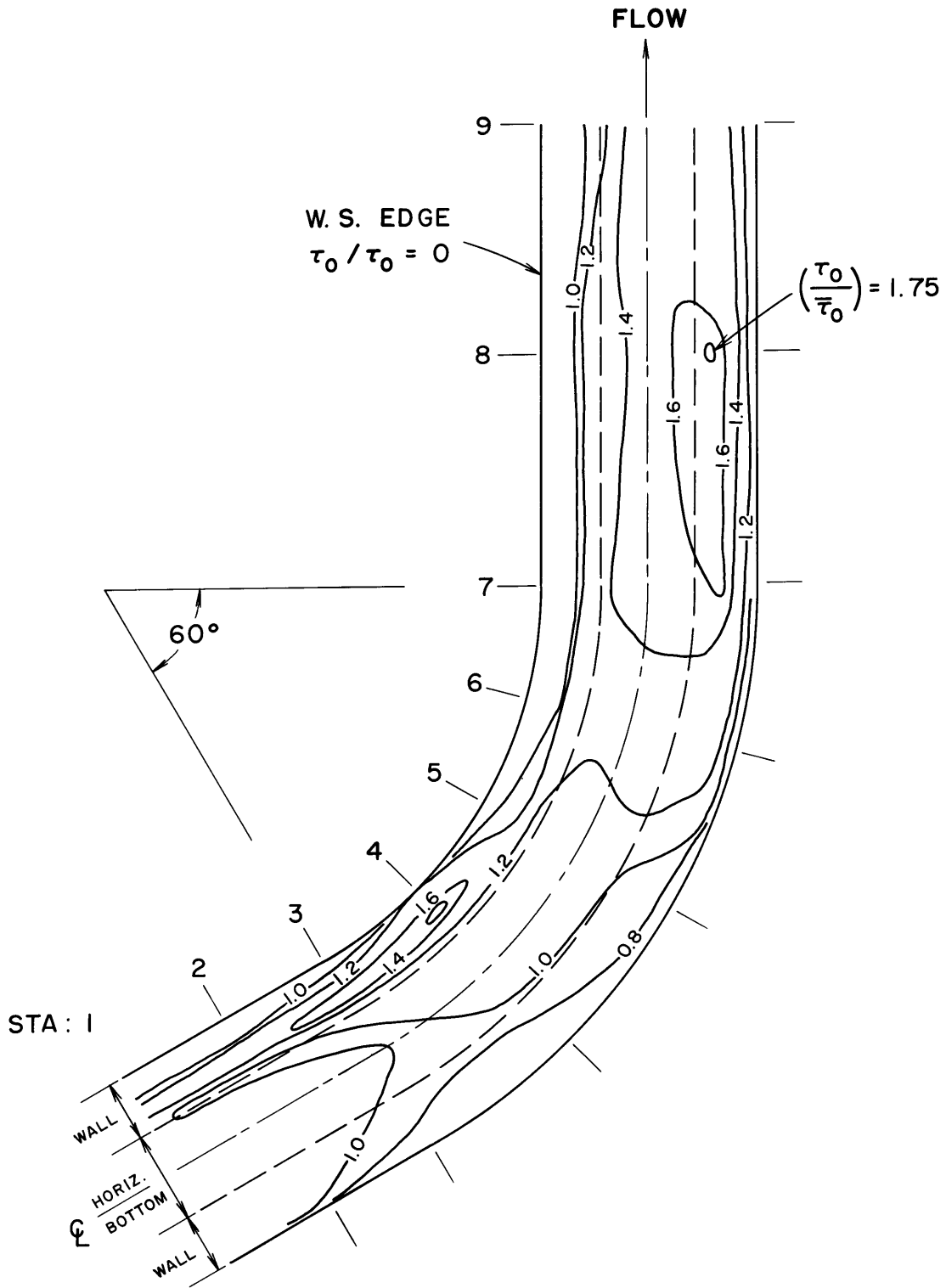


Figure 17

Closely allied with the above trend is the change in location of the maximum local shear stress with variation in stream depth and curvature; with increasing depth and curvature the location of the highest shear shifts upstream from the outer bank to the inner part of the curve. In Runs 5, 6, 7, 1, and 2 the maximum shear was measured near the outer bank in the downstream tangent. In Run 3, there are three points of high shear, the maximum occurring high on the inner bank at Station 4, while in Run 4, the maximum occurs at Station 7, with high shears extending above Station 3 along the bank.

An evaluation was made of the average relative shear over the entire test reach affected by the curve, from Stations 1 through 9. The variation of the ratio $\overline{\tau_L} / \overline{\tau_0}$ with relative curvature, w/r_c which is shown in Figure 35, suggests a trend of increasing average shear with increasing curvature. It should be borne in mind, however, that for the range of curvatures studied, the total variation observed in $\overline{\tau_L} / \overline{\tau_0}$ is of the same order of magnitude as the experimental error inherent in the shear measurement technique (See Appendix E). Thus, while a greater range in w/r_c would be necessary in order to define the variation in $\overline{\tau_L} / \overline{\tau_0}$, the trend shown in Figure 35 is clearly indicative of the effect of stream curvature on bend resistance.

The tests conducted at similar ratios of width to depth are indicated in Figure 35. For Runs 2 and 5, $w/y_0 = 10$, and for Runs 4 and 6, $w/y_0 = 8$. With the very limited amount of data available for this comparison, no trend could be observed simply on the basis of the cross-sectional shape of the stream. It seems reasonable to assume, however, that the effect of depth per se on the shear pattern should be less important and that the dominant factor is the stream curvature.

(11)

In addition to the comparison of the mean relative shear stresses shown in Figure 35, plots were prepared showing the variation with w/r_c of the maximum local relative shear, as well as of the area enclosed by a condition of given relative shear stress. While the mean shear $\overline{\tau}_L / \overline{\tau}_0$ is of interest as an indication of the bend resistance, the information given in Figures 36 and 37 is perhaps more directly applicable to the problem of revetment design in channel curves. In spite of considerable scatter in the data, there is an evident trend of increasing relative shears with increasing curvature.

It is of interest to note that in an earlier report (19) which did not include the results of Runs 5-7, it was stated that the mean relative shear in Run 2 appeared to be inexplicably lower than those of the other three tests. However, from the results of the completed test series (Figures 35-37), it is evident that Run 2 conforms quite well to the general trend, and that the relative shears in Run 1 are somewhat high. The possible significance of the deviations of Runs 1 and 2 from the general trend is discussed in the section below on Energy Dissipation in the Test Reach (WD).

The greater deviation of Run 1 may be due to error in the calibration of the static pressure probe in the Model II surface Pitot tube (See Appendix B) which was used in the test. At the time of the first four tests, Runs 2 and 3 were completely verified with different instruments, but since the results of Run 1 appeared reasonable it was not checked. After completion of the full test series, the remainder of which was conducted with the Model III instrument, it was found that the Model II calibration becomes uncertain at low depths, tending to give substantial positive errors in the computed local shears. It is

unfortunate that this calibration error was discovered after the alteration of the channel, which prevented a re-examination of Run 1.

In Figure 36 it will be noticed that the maximum local shear in Run 1 conforms to the indicated trend while that in Run 2 appears to be too low. While this may indeed be the case, it should be recognized that measurement of the point of extreme shear is statistically uncertain for the relatively small sampling of the total stream bed areas which was necessary in these tests. Thus, a more reliable criterion of the variation between tests is the mean relative shear, or, alternatively, the percentage of the test reach affected by a given intensity of relative shears.

From these tests it can be concluded that the boundary shear stresses in a channel curve vary with the flow conditions and with the channel configuration. The distribution and magnitudes of the relative shear stresses appear to be functions primarily of the stream geometry. For the range of conditions tested in 60-degree curves, $7 < w/y_0 < 12$ and $1.75 < r_0/w < 4$, the maximum local shears, expressed as $\tau_0/\bar{\tau}_0$, are of the order of 2.

2. Rough Channel: Tests 8 and 9.

a. Entrance Conditions. As with Runs 1-7 discussed previously, the flow at the entrance to the curve in the rough channel is essentially symmetrical about the channel axis (Figures 10,18,19). While there is no expression analogous to Equation (10) for the estimation of the boundary layer over a rough surface, it may be inferred that the boundary layer was fully developed in both tests. The decrease in Reynolds number and the increased coefficient of friction for the rough channel would both lead to a more rapid development of uniform flow.

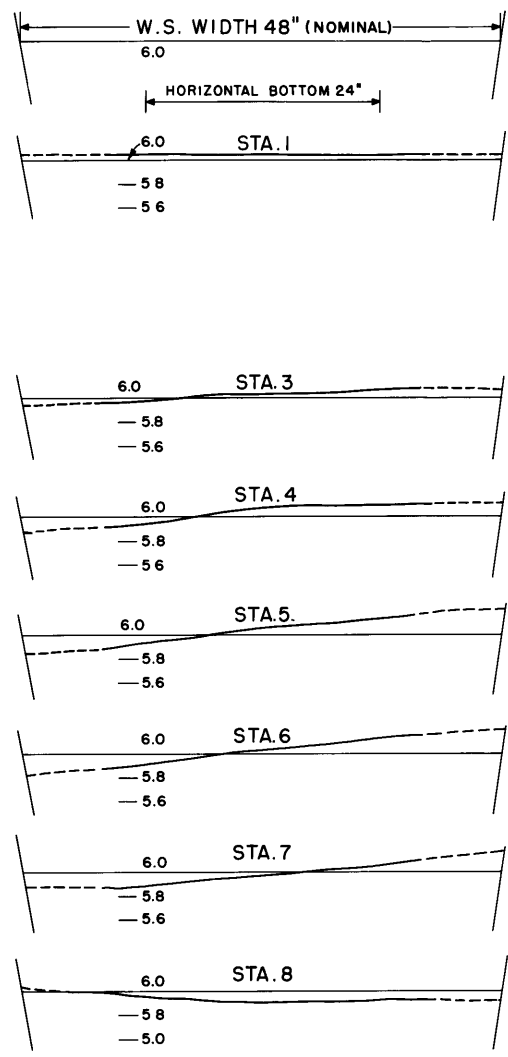
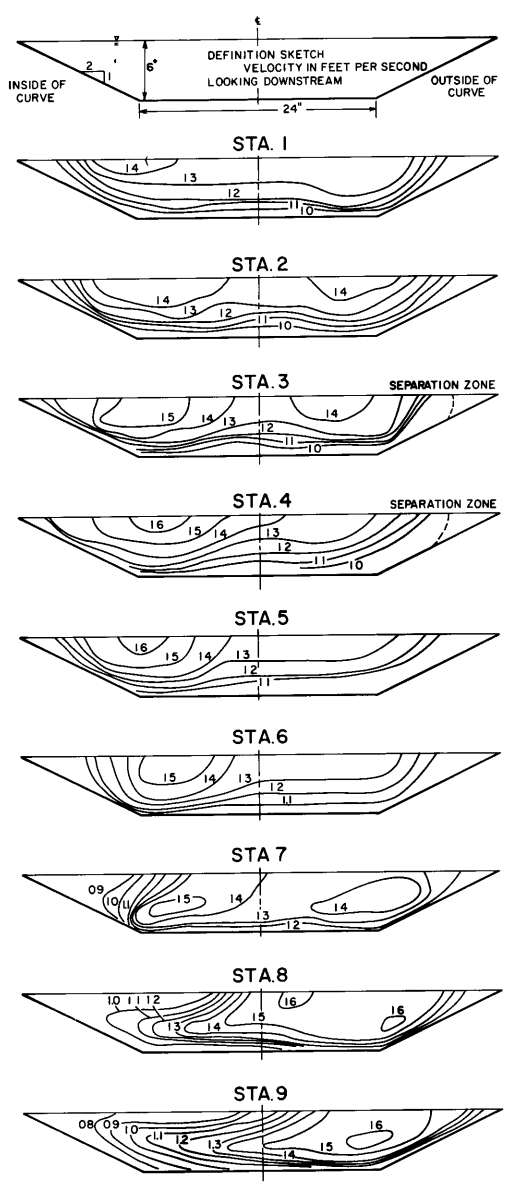


Figure 18. Velocity Distributions;
Run No. 9: Rough Channel,
Uniform approach,
 $y_0 = 6.05''$,
 $w/y_0 = 8$, $w/r_c = 0.8$.

Figure 19. Transverse Water
Surface Profiles
Run No. 9.

b. Flow through the Curve. The tendency towards free vortex motion is again evident in the velocity distributions and water surface configurations for flow through the rough channel. Comparison of Figure 18 with Figure 6 shows that the gross characteristics of the flow are essentially unchanged by the introduction of boundary roughness to a bend of a given geometry.

For channels of equal cross section and slope, but of different roughnesses, the mean shear stress over the full perimeter at uniform flow, $\gamma R S_e$, is a constant, independent of the roughness. Any variation in the friction factors for different channels requires an inverse variation in the mean velocity head of the stream in order to maintain uniform conditions. While it was not possible to duplicate exactly the conditions of the corresponding smooth channel tests, a comparison of the values of $\overline{\tau}_0$ and $\gamma R S_e$ in Table II for Runs 2 and 8 and Runs 4-B and 9 shows that the magnitudes of the mean shears at each depth are indeed independent of the boundary roughness.

c. Boundary Shear Stress. The general patterns of the boundary shear distributions for these tests are quite similar to those in the corresponding smooth channel tests. As a result of the predominant free vortex type of motion the stresses in the early part of the curve are greatest on the convex bank. Towards the exit of the curve the transfer of high momentum fluid to the outer bank causes increased shears along the outer edge of the stream.

However, a comparison of Figure 20 with Figure 12, and Figure 21 with Figure 14 reveals certain deviations from the smooth channel patterns. In the maps for the rough channel tests the initial crossover pattern is quite evident at Station 6, suggesting a more rapid transfer of the stream

Figure 20. The Distribution of Boundary Shear Stresses in the Curved Reach, Shown by Contours of $\tau_o/\bar{\tau}_o$;

Run No. 8: rough channel, $b/r_c = 0.42$, uniform approach, $w/y_o = 10$, $w/r_c = 0.67$, $y_o = 3.94''$, $\bar{\tau}_o = 0.0085$ psf.

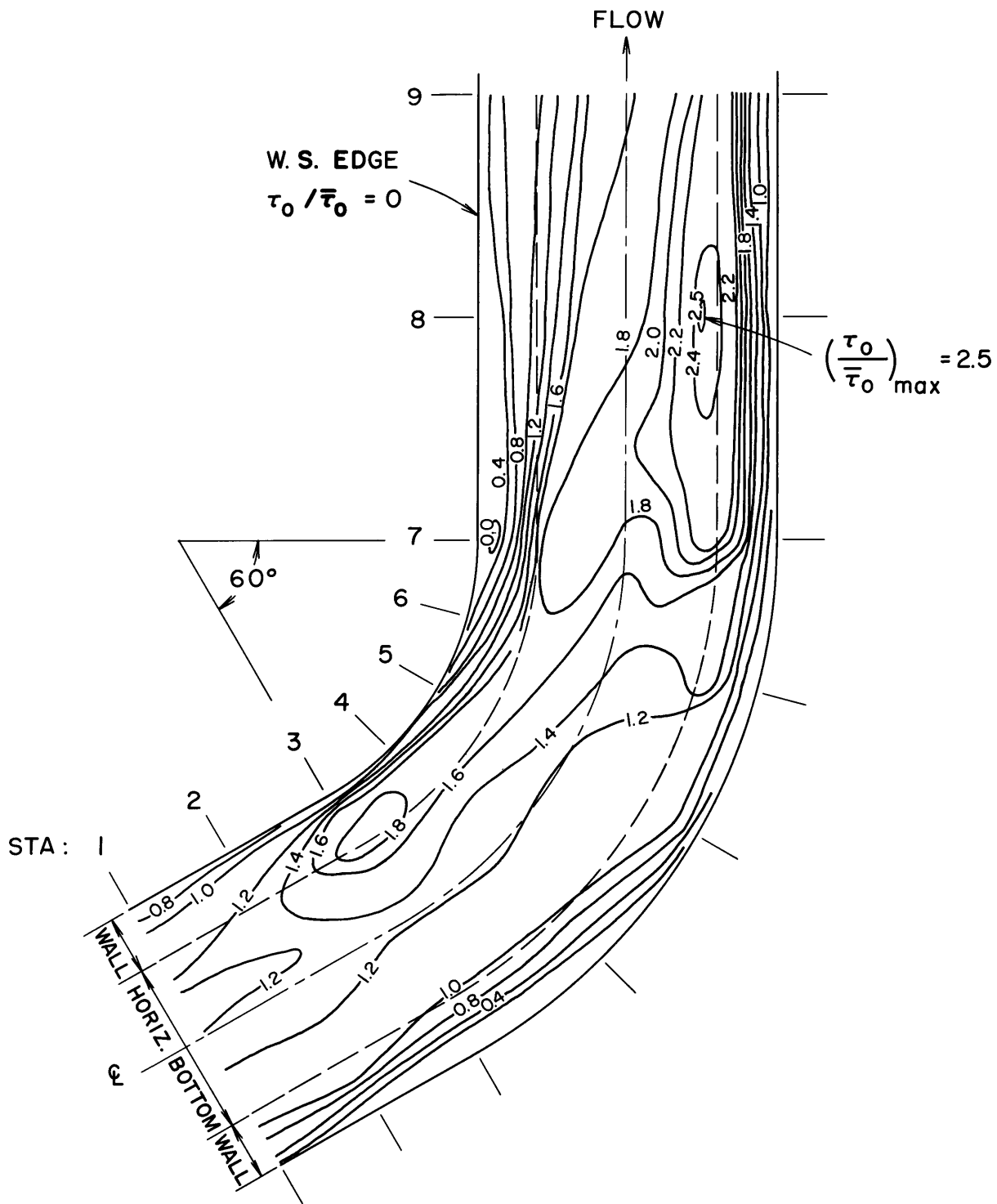


Figure 20

Figure 21. The Distribution of Boundary Shear Stresses in the Curved Reach, Shown by Contours of $\tau_o/\overline{\tau_o}$;

Run No. 9: rough channel, $b/r_c = 0.42$, uniform approach, $w/y_o = 8$, $w/r_c = 0.8$, $y_o = 6.05''$, $\overline{\tau_o} = 0.012$ psf.

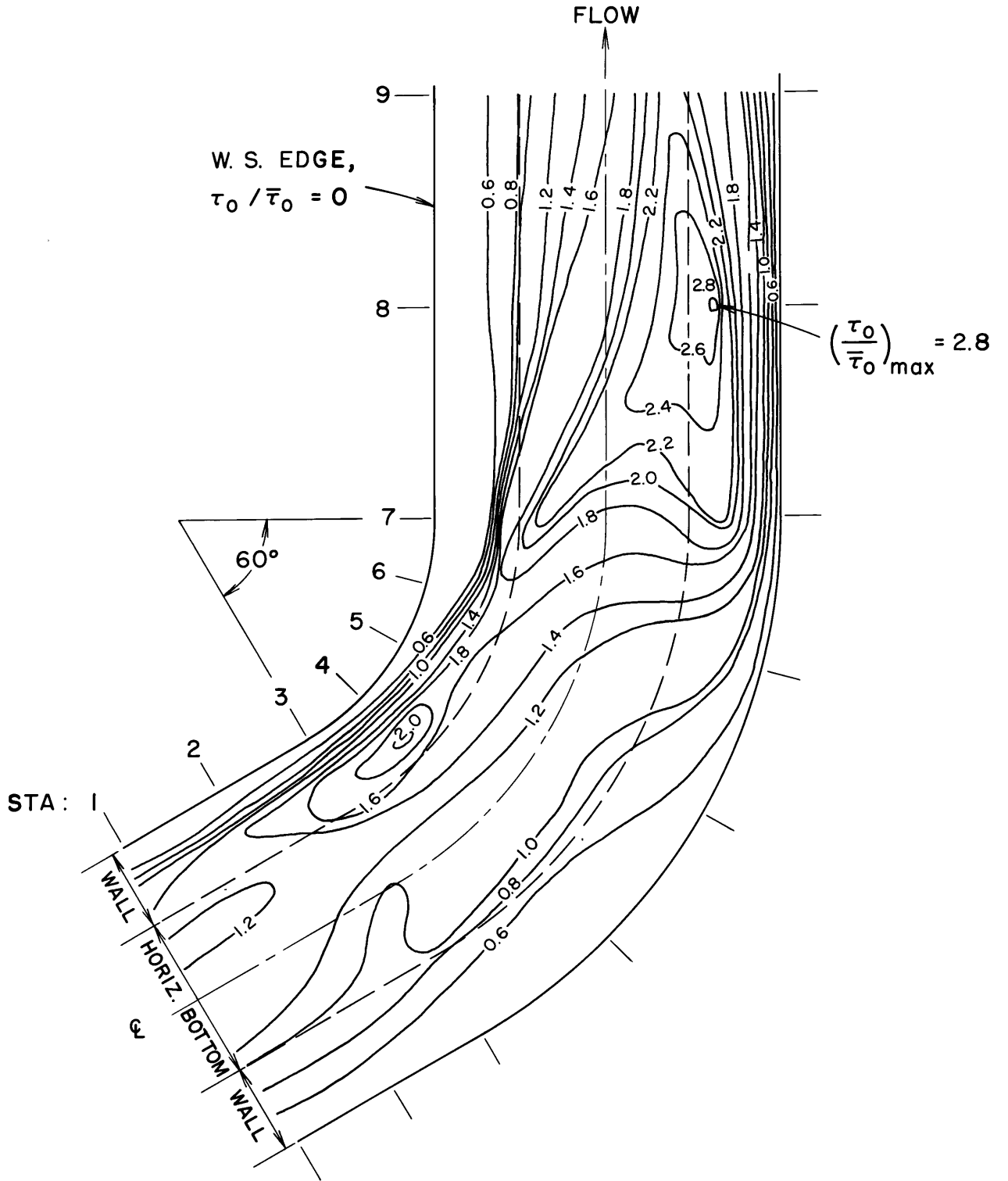


Figure 21

momentum to the outer bank. In addition, while the shear stresses throughout most of the curve are of the same magnitudes as in the smooth channel tests, those in the downstream reach are considerably higher.

In order to explain this behavior, the helicoidal motion in the curve may again be considered. Due to the rough boundary, which prevented the motion of dye crystals, and also caused a rapid diffusion of the aqueous dye, it was not possible to clearly evaluate the secondary bottom currents. However the presence of the helicoidal motion was obvious, and some inferences can be drawn regarding its effect on the flow structure. In the rough channel, the mean velocity and, hence, the super-elevation in the curve, are lower than for the same curve geometry in the smooth channel. However, since all velocities are decreased, it is reasonable to assume that the maximum angularity of the flow remains essentially constant. Near the bed of the rough channel, a relatively greater thickness of the fluid is retarded by boundary drag. Thus, a greater portion of the stream will undergo transverse motion due to the radial pressure gradient. The result of this will be to accelerate the crossover bringing more high momentum fluid to the outer bank, with an ultimate increase in the attack exerted by the stream along the outside bank.

From the two tests in the rough channel it may be concluded that the general pattern of flow through a bend of given curvature is not greatly affected by the boundary roughness. With increased roughness the helicoidal motion affects more of the stream, resulting in a greater concentration of momentum and higher shear stresses along the outer. For these tests at relatively high curvature, the maximum local shear stress is of the order of $\tau_o / \bar{\tau}_o = 2.5$.

B. Tests with Simulated Compound Curve Systems: Runs 10-13

1. Entrance Conditions.

In the tests of simulated double and reverse-bend patterns, the approach flow was deliberately distorted in order to determine the effect of upstream curvature on the boundary shear distribution. For this purpose, systems of baffle screens (See Appendix A, Figures A-4 and A-5) were installed near the channel entrance to impose the desired conditions at Station 1.

The simulation of the double-bend pattern was established as follows: using as models the downstream shear and velocity distributions taken in the corresponding single curve tests (Run 2, Station 8 for Run 10; Run 4-A, Station 9 for Run 11), the screen sets were adjusted until these same distributions were obtained at Station 1. Figures 22 and 23, a, b, and e, show the comparison of the desired patterns with those obtained by this technique.

The reverse-bend patterns were obtained in a similar way by screens placed on the opposite side of the channel. For these tests the downstream distributions of velocity and shear from Runs 2 and 4-A were reversed, and the inverted patterns used as models. The desired and obtained distributions are shown for the reverse-bend tests in Figures 24 and 25, a, b, and e.

In each case the major portion of the screen system was located as far upstream as possible. This produced a more gradual shift of the velocity distribution near the entrance to the curve, without creating major surface disturbances. The screen arrangement for each test is shown schematically in the inset sketch on the appropriate shear map (Figures 28-31).

Figures 22, 23, 24, 25. Shear and Velocity Patterns obtained for the simulated compound curve systems. The four tests were performed in the smooth channel, $b/r_c = 0.42$.

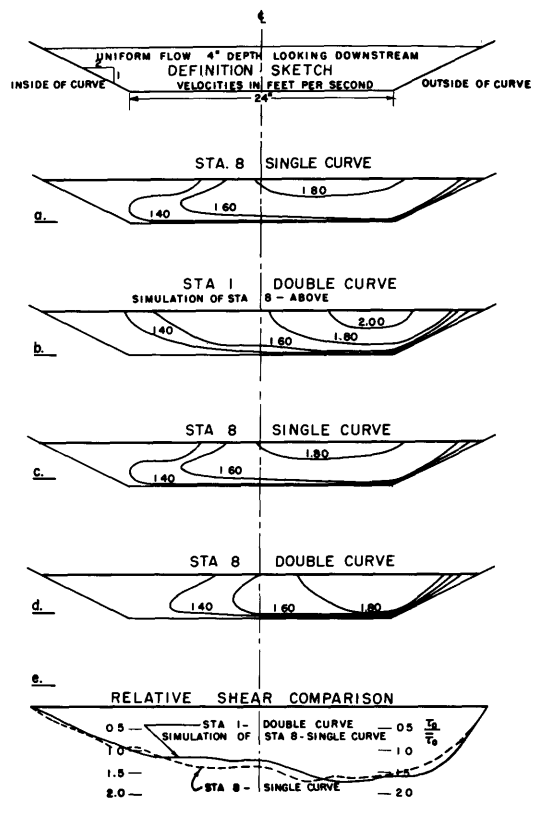


Figure 22. Run No. 10:
Double Curve, $y_0 = 3.86''$,
 $\tau_0 = 0.0081$ psf.

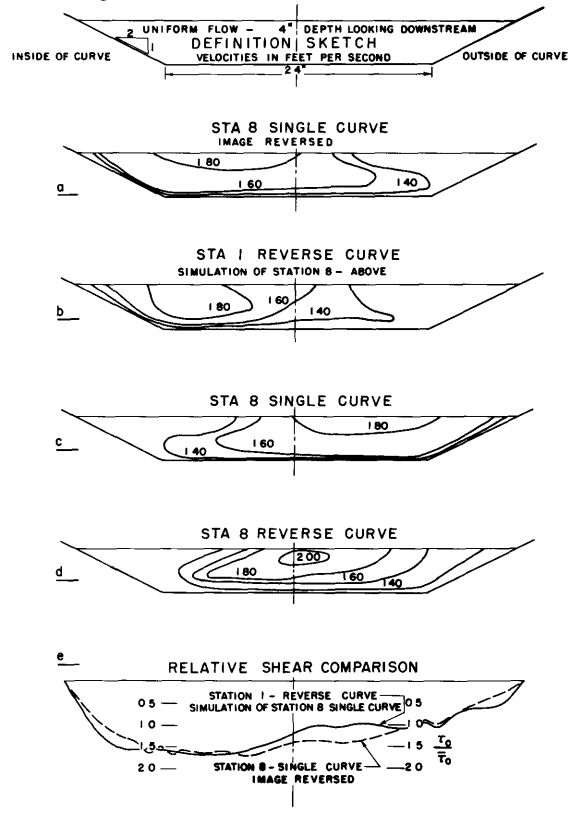


Figure 24. Run No. 12:
Reverse Curve, $y_0 = 3.86''$,
 $\tau_0 = 0.0081$ psf.

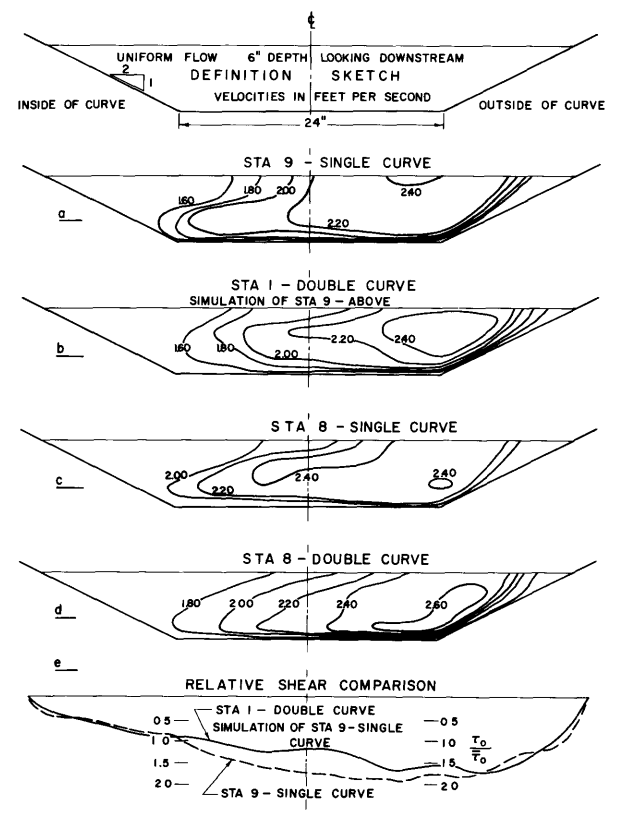


Figure 23. Run No. 11: Double
Curve, $y_0 = 6.00''$, $\tau_0 = 0.0123$ psf.

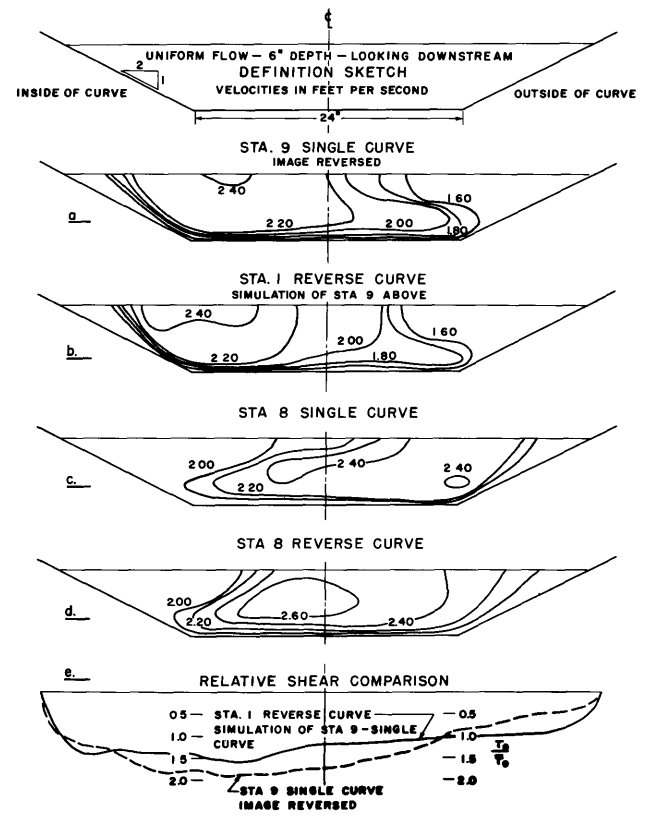


Figure 25. Run No. 13: Reverse Curve
 $y_0 = 6.00''$, $\tau_0 = 0.0123$ psf.

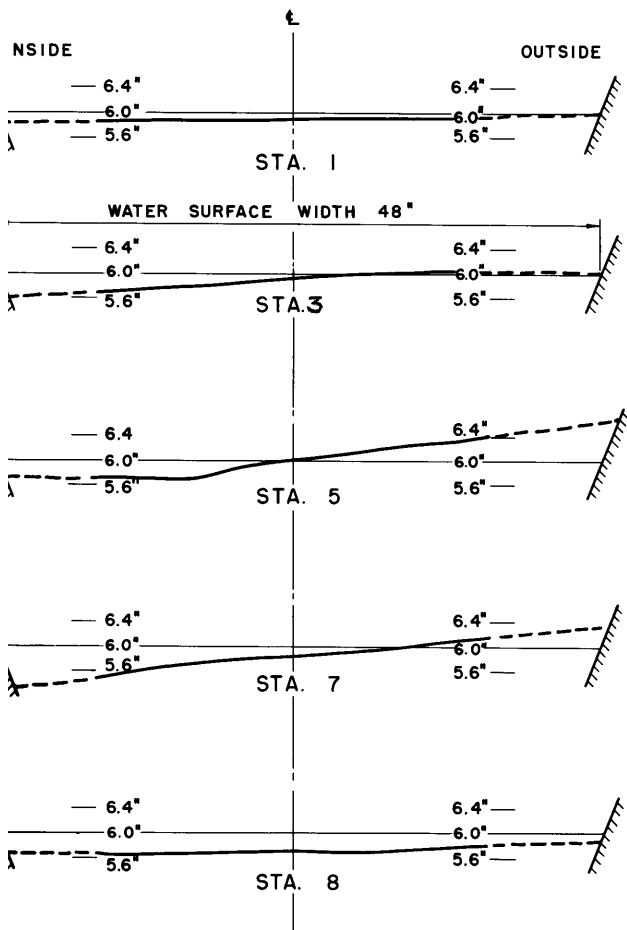


Figure 26. Transverse Water Surface Profiles;
 Run No. 11: Simulated Double curve,
 $y_0 = 6.00''$.

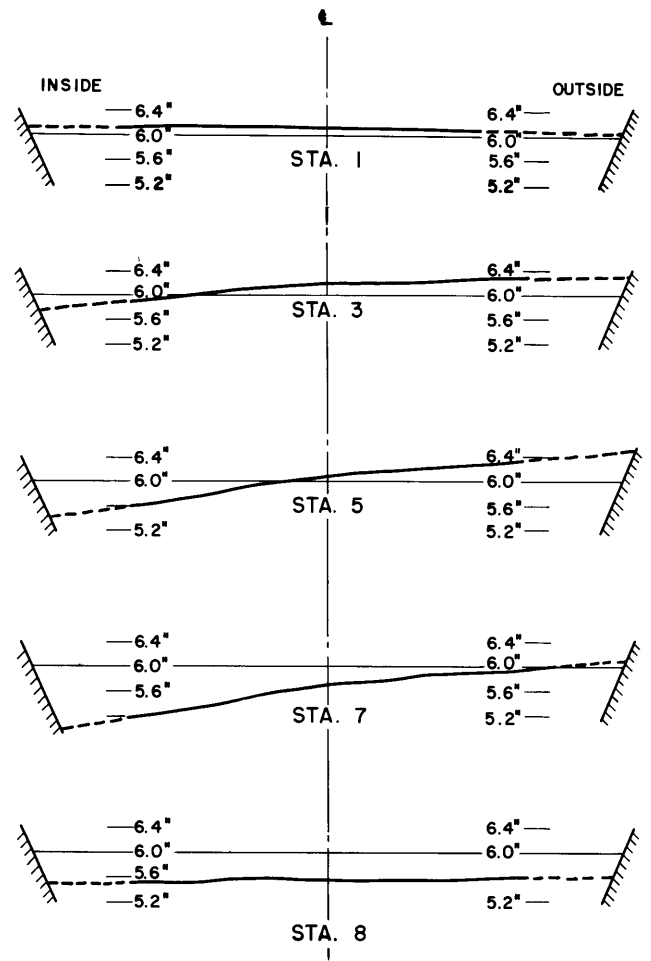


Figure 27. Transverse Water Surface Profiles;
 Run No. 13: Simulated Reverse Curve,
 $y_0 = 6.00''$.

The baffle screens caused non-uniform conditions which prevented the determination of approach flow gradient and which also increased the average shear stress at Station 1 to a value greater than that measured at conditions of uniform approach. In the calculation of $\tau_o / \overline{\tau_o}$, therefore, the average shear, $\overline{\tau_o}$, was used as determined in the single curve series for Runs 2 and 4-A.

The modifying screen systems produced velocity and shear distributions corresponding to the exit conditions of a curve upstream of the channel bend. It was unnecessary to reproduce a helicoidal motion, since below the curve exit the superelevation and, hence, the secondary current, abates rapidly. Since the degree of similitude which can be attained with simple screen arrangements is limited, the shear patterns obtained from the compound curve series should be regarded as being somewhat qualitative.

2. Flow through the Curve.

The overall pattern of flow through the curve was not greatly affected by the velocity distributions which were imposed at Station 1. The helicoidal pattern could again be detected by dye traces, although the increased turbulence of the flow caused a more rapid diffusion of the dye. As might be expected, the separation zone on the same side of the flume as the higher velocities was reduced while that on the opposite bank was increased in extent. In the reverse-bend tests, the roller on the convex bank was barely evident, and in the double-bend tests, reduced velocities occurred on the concave bank without reversed flow.

The shapes of the water surface profiles (Figures 26, 27) for the double and reverse curves varied somewhat from those measured in the single curve tests. The profile at Station 5 for the double curve test shows the

effect of the higher velocities along the outer bank, with a broad stagnant zone on the inner part of the bend. In the reverse bend tests, the separation zone on the inner bank is reduced, and the profiles are accordingly steeper near the inside edge throughout the curve.

In spite of the gross variations in velocity distributions imposed on the flow, the maximum superelevations measured in these tests are essentially the same as those for the corresponding single curve tests. The superelevations measured and computed for Runs 2, 10, 12, and Runs 4-A, 11, 13 may be compared in Table IIIa, b.

Because the velocity distribution in the single curve tests was shown to be related to the mapped shear pattern, the detailed velocity profiles are not given for the compound curve tests. Parts b and d of Figures 22-25 show the velocity profiles taken at Stations 1 and 8 in the four tests. Further discussion of the velocity distribution is given in relation to the shear stress patterns.

3. Boundary Shear Stress.

Before proceeding with a discussion of the shear stress distributions determined in these tests, it is necessary to explain the shear maps shown in Figures 28-31. Consider the map of the 4-inch double-bend test, Figure 28; the right-hand half of the figure represents that portion of the channel which was actually mapped for the entrance conditions of velocity and shear shown in b and e of Figure 22. In the left half of Figure 28, the shear data for the single curve 4-inch test, Figure 12, have been reproduced. The two maps were joined by sketching the contours together to provide the shear distribution throughout the double bend shown in Figure 28.

For the 4-inch reverse-bend test, Figure 30, the right-hand

Figure 28. The Distribution of Boundary Shear Stresses in a Simulated Double Curve System, Shown by Contours of $\tau_o/\bar{\tau}_o$;

Run No. 10: smooth channel, $b/r_c = 0.42$, non-uniform approach, $w/y_o = 10$, $w/r_c = 0.67$, $y_o = 3.86''$, $\bar{\tau}_o = 0.0081$ psf.

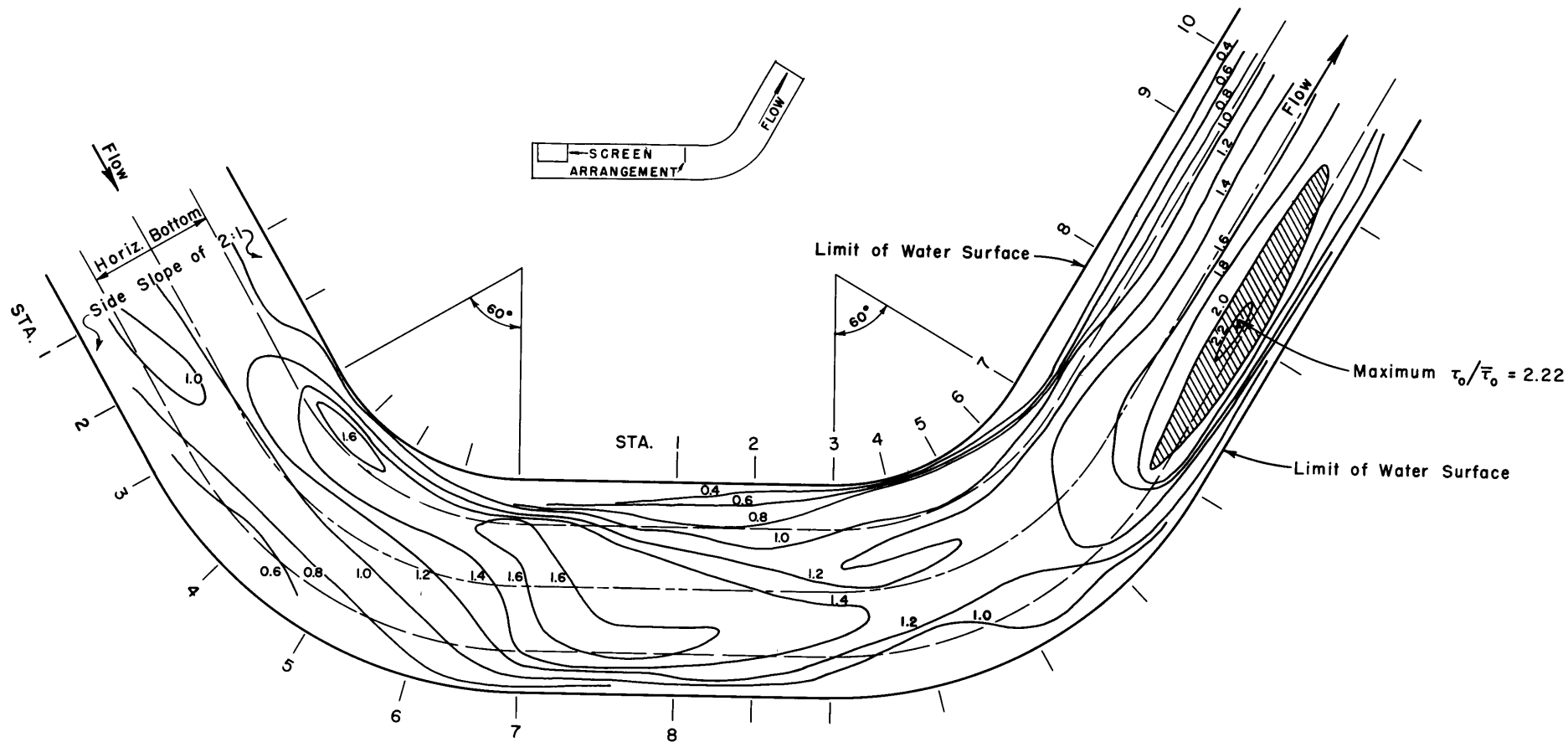


Figure 28

0057

Figure 29. The Distribution of Boundary Shear Stresses in a Simulated Double Curve System, Shown by Contours of $\tau_o/\bar{\tau}_o$;

Run No. 11: smooth channel, $b/r_c = 0.42$, non-uniform approach, $w/y_o = 8$, $w/r_c = 0.8$, $y_o = 6.00"$, $\bar{\tau}_o = 0.0123$ psf.

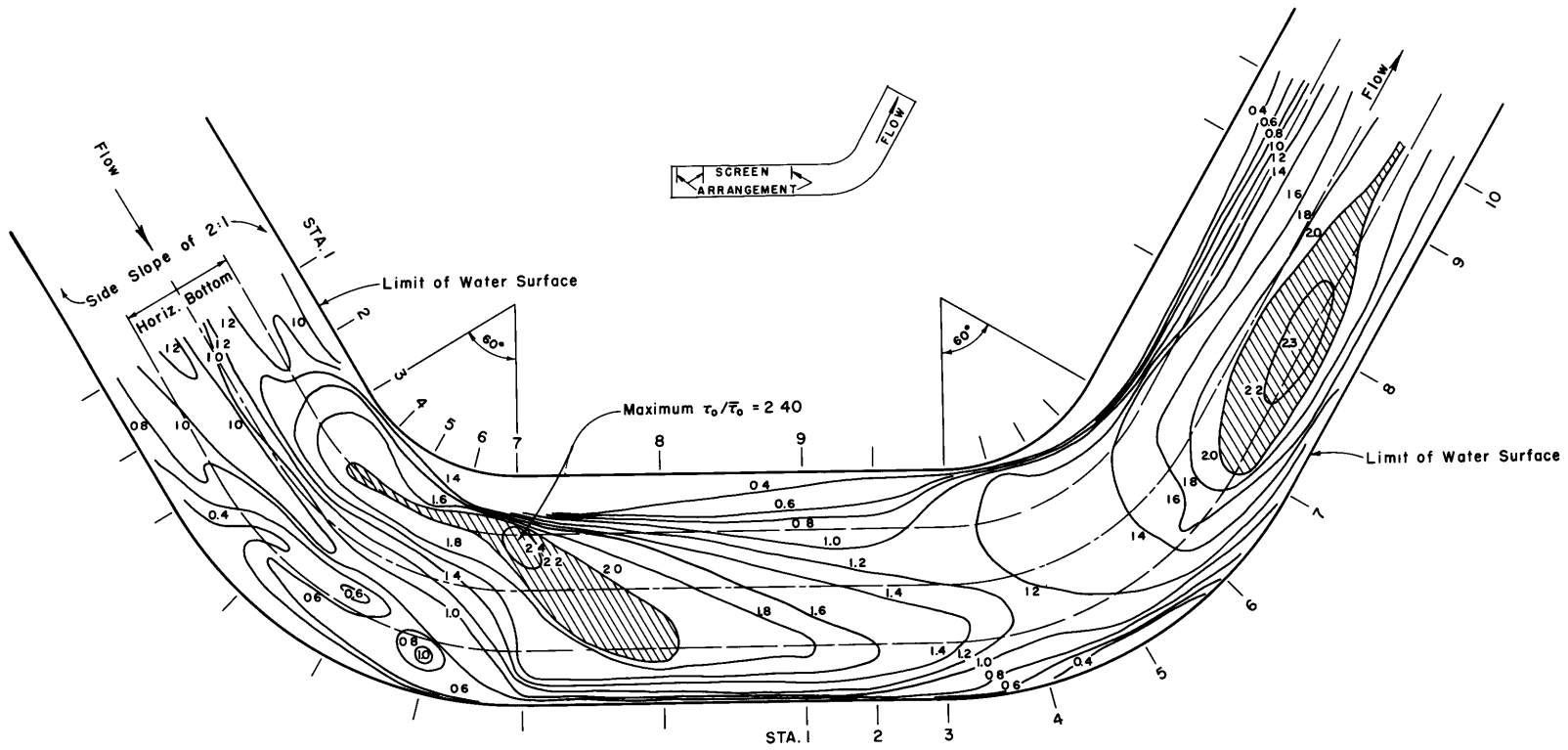


Figure 29

Figure 30. The Distribution of Boundary Shear Stresses in a Simulated Reverse Curve System, Shown by Contours of $\tau_o/\bar{\tau}_o$;

Run No. 12: smooth channel, $b/r = 0.42$, non-uniform approach, $w/y_o = 10$, $w/r_c = 0.67$, $y_o = 3.86''$, $\bar{\tau}_o = 0.0081$ psf.

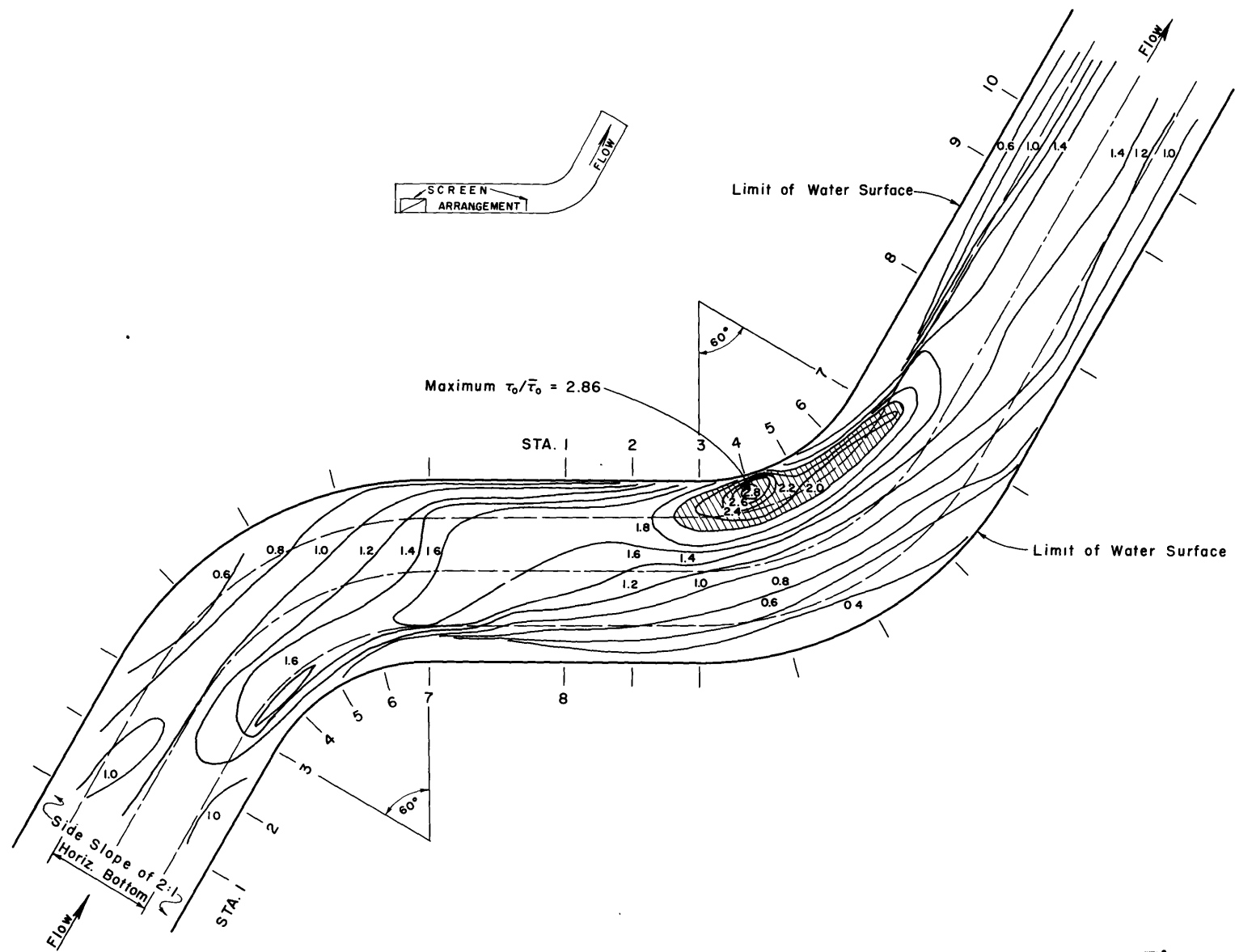


Figure 30

00500

Figure 31. The Distribution of Boundary Shear Stresses in a Simulated Reverse Curve System, Shown by Contours of $\tau_o/\bar{\tau}_o$;

Run No. 13: smooth channel, non-uniform approach, $w/y_o = 8$,
 $w/r_c = 0.8$, $y_o = 6.00''$, $\bar{\tau}_o = 0.0123$ psf.

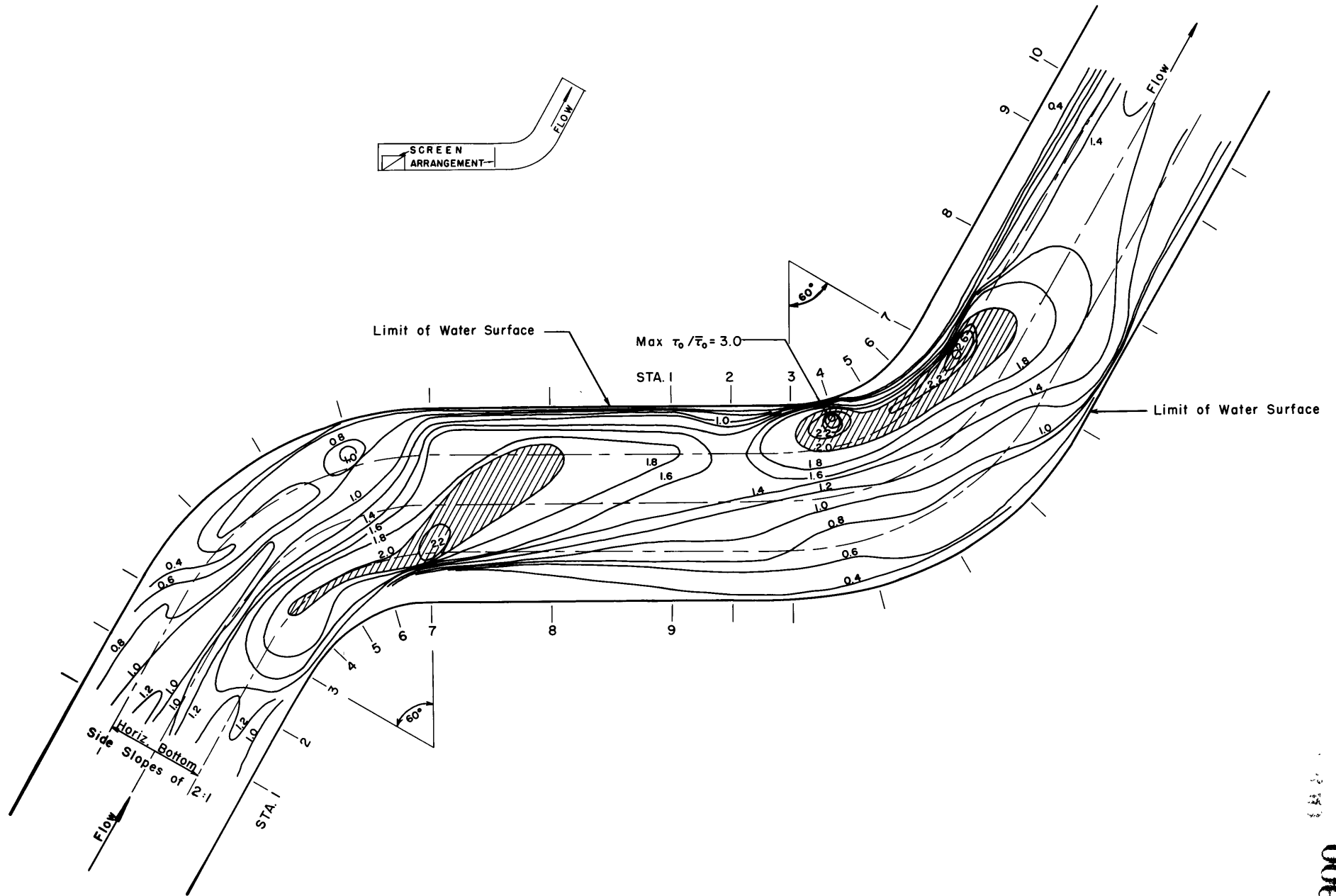


Figure 31

section was mapped for the entrance conditions shown in b and e of Figure 24; the pattern from Figure 12 was reproduced in reverse to show the upstream curve. The maps of the 6-inch double and reverse-bend tests were prepared in exactly the same way, with the upstream curve pattern being obtained from Figure 14. The boundary shears were mapped for the entrance conditions shown in Sections b and e of Figures 23 and 25.

Examination of Figures 28-31 reveals the striking similarity between the shear patterns of the 4-inch and 6-inch tests, for both the double and reverse-bend series.

In the double-bend tests, the deflection of the high velocities to the outside of the sequent bend prevents any degree of attack on the inner bank. In the downstream reach, comparison of the contours of $\tau_o / \overline{\tau_o} = 1.8$ shows that the shears are somewhat lower in Run 10 than in Run 11, although the difference is slight. The diminution of the outer bank shears within the sequent curve indicates a tendency for the flow to revert to the irrotational pattern of the single curve tests; however the momentum stays high on the outside and leads to sharply rising shear stresses on the outer bank, below the curve.

Figures 30 and 31 reveal that, in the reverse-bend tests, high shears -- higher, in fact, than any measured in previous tests -- are confined to the convex bank. This high shear intensity occurs high up on the bank, throughout the curve, and the crossover pattern seen in the earlier tests never develops. The deflection of the high velocities in the approach section to the inner bank reinforces the natural tendency towards free vortex flow. The momentum of the fluid along the inner bank is sufficient to prevent separation. In the absence of the high velocity shift to the outside, the high momentum diffuses rapidly through the

stream, and the shears return to normal, with a symmetrical distribution resulting again in a short distance.

The great similarity of the two shear patterns, in the double and reverse-bend tests, might best be explained by the turbulent structure of the flow in the various tests. For the single bend series, the flow enters the channel through a smooth transition from a reservoir in which there is essentially no turbulence. Thus, at Station 1, all of the stream turbulence is that which is generated in the boundary layer. With the introduction of upstream screens, however, free stream decaying turbulence is introduced into the flow at the point of disturbance. Since the variation in Reynolds number between the 4-inch and 6-inch screen conditions is small, it is to be expected that the turbulence intensities should be comparable. If the free stream turbulence were of sufficient intensity to overshadow the normal boundary effects, then the relative shear patterns would be quite similar, as indeed was the case.

In each of Figures 22-25 it will be noticed that sections c and d are more closely related to each other than they are to section a. The implication to be drawn from this is that, as might be expected, the effects of flow disturbances are not compounded indefinitely through curves.

Within the limitations of the simulative approach used in these tests, certain conclusions can be drawn. In the sequent part of a double-bend, the shear stresses are highest along the outer bank, and do not vary greatly over those in a single curve. In a series of closely spaced reverse curves, the shears along the inner bank may be greatly increased. It is probably safe to infer that a tight S-pattern, such as that in Runs 12 and 13, would not normally be found in natural streams; the

high shears on the sequent convex bank indicate that this configuration would tend to straighten itself rapidly.

C. Superelevation in the Channel Bend

As shown in the earlier discussions, the major non-ideal aspects of the flow through a curve -- i.e. helicoidal motion and separation -- are intimately related to the varied pressure gradients induced by the water surface configuration. It is of interest, therefore, to compare the measured superelevations with those predicted on the basis of various assumed conditions of flow.

As a first approximation the superelevations may be computed from one-dimensional analysis. Assuming concentric flow at a constant uniform velocity, such that the momentum of the stream acts at the mean (centerline) radius of the curve, the superelevation is given by,

$$\Delta y = \int_{r_i}^{r_o} \frac{v^2}{gr_c} dr = \frac{v^2}{2g} \frac{2w}{r_c}, \quad (11a)$$

where the subscripts, i and o, refer to the inner and outer radii of the bend, respectively.

Since the gross features of the flow through the single curve indicate an essentially irrotational behavior, a better approximation should be attainable by treating the flow as a free vortex, $u \propto 1/r$. By again equating the radial pressure gradient to the centripetal acceleration, and integrating over the width of the stream, the superelevation, in terms of a proportionality constant, is given by,

$$\Delta y = \frac{K_1^2}{2g} \left(\frac{1}{r_i^2} - \frac{1}{r_o^2} \right); \quad K_1 = ur.$$

In order to evaluate K_1 , it is convenient to assume a rectangular section; it should be noted, however, that for a trapezoidal section of equal width and mean velocity, K_1 should be somewhat smaller. Not only is the discharge, and hence total momentum, reduced through a trapezoidal section, but the effective radius is increased as the water surface moves outward on the sloping banks.

In the channel experiments it was established that the variation in area, and hence mean velocity, is slight throughout the test reach. Further, under the assumption of irrotational flow, the specific head, $H_0 = y_0 + u^2/2g$ is constant across a section. Thus as a good approximation

$$A = \bar{y}_0 w = \bar{y}_0 (r_0 - r_i) = \int_{r_i}^{r_0} y_0 dr = \int_{r_i}^{r_0} \left(H_0 - \frac{K_1^2}{2gr^2} \right) dr,$$

which reduces to

$$\bar{y}_0 = H_0 - \frac{K_1^2}{2gr_0 r_i} = H_0 - \frac{V^2}{2g}.$$

Solving for K_1 and substituting into the original expression for Δy , the superelevation in the free vortex becomes

$$\Delta y = \frac{V^2}{2g} \frac{2w}{r_c} \left(\frac{1}{1 - \frac{w^2}{4r_c^2}} \right), \quad (11b)$$

where,

$$r_0 - r_i = w$$

and

$$r_0 + r_i = 2r_c.$$

In the double curve tests, Runs 10 and 11, the higher velocities induced on the outer bank suppressed the free vortex motion. In natural streams also, the flow in curves will show various degrees of asymmetry, depending on the entrance conditions, the curvature, and the arc length of the curve. It is of interest, therefore, to consider as a further comparison the superelevation produced in a curve for a stream undergoing motion as a forced vortex. For this case,

$$\Delta y = \frac{K_2^2}{2g} (r_o^2 - r_i^2) ; \quad K_2 = \frac{u}{r} .$$

Once again it is assumed that A and V are constant throughout the curve. However, for the forced vortex, H_o is not a constant across the section, although to a fair approximation the mean specific head, $\overline{H}_o = \overline{y}_o + V^2/2g$, does not vary through the curve. (This argument is, of course, restricted to subcritical flows). The expression for the area of the stream section becomes

$$A = \overline{y}_o w = \int_{r_i}^{r_o} \left(H_o - \frac{K_2^2 r^2}{2g} \right) dr .$$

Now, as noted above, $\overline{H}_o = \frac{1}{w} \int_{r_i}^{r_o} H_o dr$, and hence:

$$\overline{y}_o = \overline{H}_o - \frac{K_2^2}{6g} \frac{(r_o^3 - r_i^3)}{(r_o - r_i)} = \overline{H}_o - \frac{V^2}{2g} .$$

Again substituting for K_2 into the original expression for Δy , there results for the superelevation in the forced vortex,

$$\Delta y = \frac{V^2}{2g} \frac{2w}{r_c} \left(\frac{1}{1 + \frac{w^2}{12r_c^2}} \right) \quad (11c)$$

As an alternative method, the constants K_1 and K_2 may be computed from the velocity distribution,

$$V = \frac{Q}{A} = \frac{1}{w y_0} \int u(r) dr = \frac{1}{w y_0} \int f(K,r) dr .$$

If u is defined as the mean tangential velocity over a vertical section at any radius, then K may be found by evaluation of the integral with substitution of the appropriate velocity distribution function. The two methods of determining K involve somewhat different initial assumptions, and the structures of the expressions in Equations (11b) and (11c) differ accordingly. For the range of curvature in these tests, however, it was found that the coefficient of the velocity head, which is a function only of the relative curvature, varies less than 3% for the two methods of computation. The approach used in deriving Equation (11b) and (11c) is preferred because it leads to simpler expressions.

Figure 32 shows a comparison of the maximum superelevations computed from Equations (11). It is of interest to note that for the bends of moderate curvature normally found in natural streams, $w/r_c < 0.5 - 0.7$, the superelevation is virtually independent of the radial distribution of velocity. Thus, for a bend of given geometry the shape of the transverse surface profile will vary with the radial distribution of momentum; the total superelevation is a function only of the mean momentum of the stream.

For conditions approaching maximum curvature, $w/r_c = 2$ (i.e.

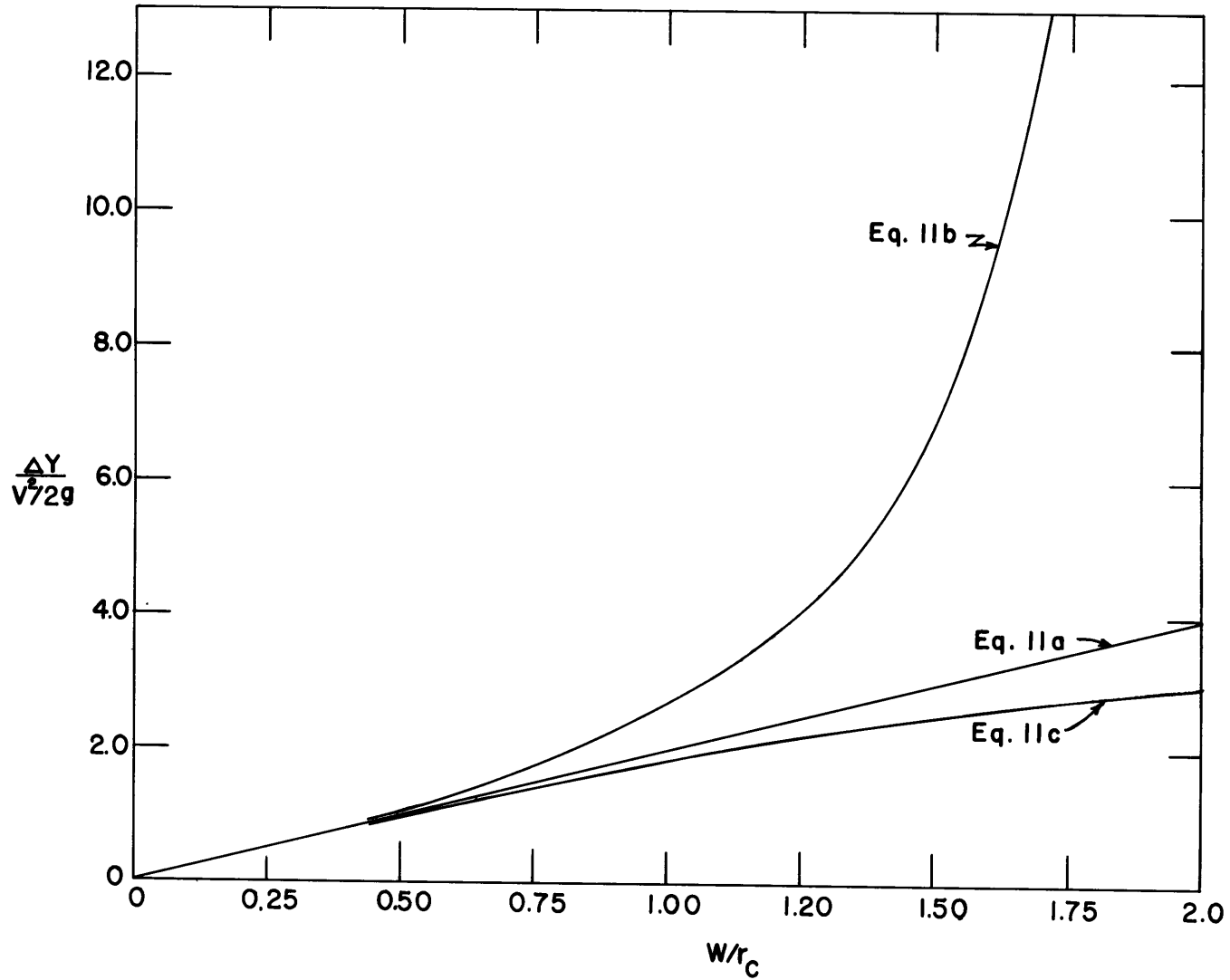


Figure 32. Variations in Total Water Surface Superelevation in a Circular Curve, as computed from one-dimensional analysis, and for the flow assumed as free and forced vortices.

TABLE III

Water Surface Superelevations Obtained from Measurements, One Dimensional Analysis and Vortex Theories.
 Δy given in inches.

Run No.	a. Full Channel Width				b. Rectangular Portion of Channel			
	Meas. at Sta 5	One-Dimen. Eq. (11a)	Free Vortex Eq. (11b)	Forced Vortex Eq. (11c)	Meas. at Sta 5	One-Dimen. Eq. (11a)	Free Vortex Eq. (11b)	Forced Vortex Eq. (11c)
1	0.52	0.41	0.45	0.40	0.31	0.28	0.29	0.27
2	0.53	0.55	0.62	0.53	0.35	0.34	0.35	0.33
3	0.77	0.77	0.89	0.74	0.43	0.42	0.44	0.41
4A	--	1.09	1.30	1.04	--	0.54	0.57	0.54
4B	0.53	0.53	0.63	0.50	0.29	0.26	0.28	0.26
5	0.10	0.08	0.09	0.08	0.06	0.05	0.05	0.05
6	0.18	0.18	0.18	0.18	0.10	0.09	0.09	0.09
7	0.28	0.29	0.30	0.28	0.14	0.12	0.13	0.12
8	0.23	0.22	0.25	0.22	0.14	0.14	0.14	0.14
9	0.37	0.41	0.46	0.40	0.19	0.20	0.21	0.20
10	0.51	0.55	0.62	0.53	0.33	0.34	0.35	0.33
11	0.95	1.09	1.30	1.04	0.58	0.54	0.57	0.54
12	0.64	0.55	0.62	0.53	0.32	0.34	0.35	0.33
13	1.07	1.09	1.30	1.04	0.59	0.54	0.57	0.54

$r_i = 0$), the computed superelevation for a free vortex becomes infinite. This is, of course, in accordance with the requirement of infinite velocity at the core of an irrotational vortex. In the motion of a real fluid, separation occurs under these conditions, imposing a finite limit on the actual magnitude of the superelevation.

The values of the superelevation computed for the complete test series from Equations (11) are listed in Table III for comparison with the measured values of Δy . Table IIIa shows the results for the full width of the trapezoidal section, while in Table IIIb only the central rectangular portion of the channel is treated.

Considering the practical limitations inherent in the exact measurement of water surface elevations, the agreement between the measured and computed results is good for the full trapezoid, as well as for the rectangular section. In the earlier report on this study (19), it was stated that the values measured over the full channel width were too low. Those figures were based on the measurements made closest to the edges of the stream. In the present compilation, shown in Table IIIa, the measured profiles were extrapolated to the stream boundaries, and the superelevations so estimated used as the values for the full stream width. There is no real evidence of the expected reduction in Δy , due to the effects of the sloping sides, noted above.

Run 1 (Table IIIa) shows the largest deviation from the predicted superelevation. It is likely that in this case wave disturbances emanating from the boundary influenced the measured value of Δy . The possibility of such error exists for all measurements near the edges of the stream; the size and magnitude of the error will depend on the distribution of the disturbances with respect to location of the measurements.

For conditions of least curvature the measured superelevation conforms closely to all of the predicted values. At increased curvatures, in the single curve tests, the full-width superelevation predicted for a free vortex is consistently too high, while the one-dimensional and forced vortex equations provide reasonably good estimates. The flow adjacent to the inner bank is retarded by boundary drag and here the irrotational pattern breaks down. It will be noted that for the single curve tests, the superelevation within the rectangular section is, in general, best represented by the free vortex formulation.

In the compound curve tests, Runs 10-13, the superelevations show, as expected, little effect of variations in the velocity distribution. It appears that such differences as do occur conform generally to the predicted trend. The double curves (Runs 10 and 11) with high velocities on the outer bank resemble the forced vortex. In the reverse curves, the higher velocities on the inner bank reinforce the natural tendency towards irrotational motion, and somewhat greater superelevation results.

It may be concluded that for streams of moderate curvature the water surface superelevation is quite insensitive to variation in the radial distribution of velocities. In practice an adequate estimate may be obtained through the simple one-dimensional treatment of the flow, Equation (11a).

D. Energy Dissipation in a Channel Bend

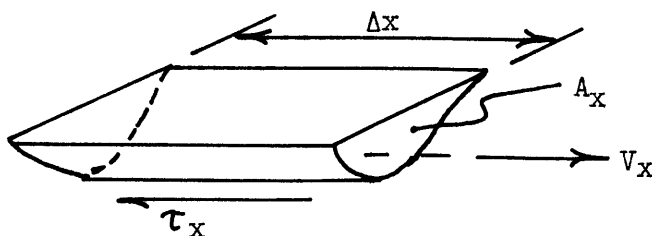
In order to relate the present work to previous studies of energy losses in bends, the measured shear distributions may be applied to a one-dimensional analysis of the energy dissipation in the curved reach of the open channel. In the following discussion only the smooth channel tests for a single curve, Runs 1-7, are considered.

As noted earlier, the short exit tangent made it impossible to study the return of the flow below the curve to uniform conditions. For this reason the results presented herein will not bear direct quantitative comparison to tests performed in channels of adequate length. However, the detailed information on the shear stresses in these tests contributes to the understanding of the modes of local dissipation as related to the overall losses in a bend.

The energy of a flowing stream is dissipated through the resistance or drag upon the solid boundaries. If a control volume is assumed of cross section A_x of perimeter P_x and of length Δx the power dissipated becomes:

$$\Delta HP = \tau_x P_x \frac{Q}{A_x} \Delta x = \tau_x P_x V_x \Delta x$$

wherein τ_x is the mean shear stress over the perimeter P_x .



The energy dissipated per pound of fluid flowing per unit length of channel becomes:

$$\left. \frac{\Delta H}{\Delta x} \right|_x = S_{e_x} = \frac{\tau_x P_x V_x}{\gamma A_x V_x} = \frac{\tau_x}{\gamma R_x} \quad (13a)$$

For uniform or normal flow in straight channels the quantities involved become independent of distance. For flow through curves and other channel transitions, variations in these quantities must be expected with distance in accordance with the non-uniform character of the flow.

Since the dimensions of the test-channel for the experiments on channel curves did not permit the establishment of completely uniform flow, the conditions at Station 1 were adopted for reference purposes. In order to avoid confusion with hydraulic properties for uniform flow which are usually denoted by the subscript, o , the coordinate, x , is here re-defined such that at Station 1, $\tau_x = \tau_1 = \overline{\tau}_o$.

Equation (13a) may be transformed by introducing a mean friction coefficient,

$$\tau_x = C_{f_x} \rho \frac{V_x^2}{2} ;$$

$$S_{e_x} = \left. \frac{\Delta H}{\Delta x} \right|_x = \frac{\tau_x}{\gamma R_x} = C_{f_x} \frac{V_x^2}{2gR_x} \quad (13b)$$

In these tests, it was found that the maximum increase in τ_x is of the order of 40% while A_x , P_x , and V_x vary only about 2-4%. From Equations (13) therefore, neglecting variations in flow geometry, the local average rate of energy dissipation is proportional to τ_x . However, $\left. \frac{\Delta H}{\Delta x} \right|_x$ is only approximately proportional to C_{f_x} within the variations of $V_x^2/2g$.

In Figure 34 graphs are shown for two of the runs in which the rate of energy dissipation relative to that at Station 1 is plotted as,

$$\frac{\tau_x}{\tau_1} = \frac{S_{e_x}}{S_{e_1}}, \text{ vs. } \frac{x}{r_c},$$

where x = centerline distance through the test reach and r_c = centerline radius of the bend. The values of average relative shear at each station, $\frac{\tau_x}{\tau_1}$, were obtained by graphical integration of the section plots of shear vs. perimeter shown in Figure 33;

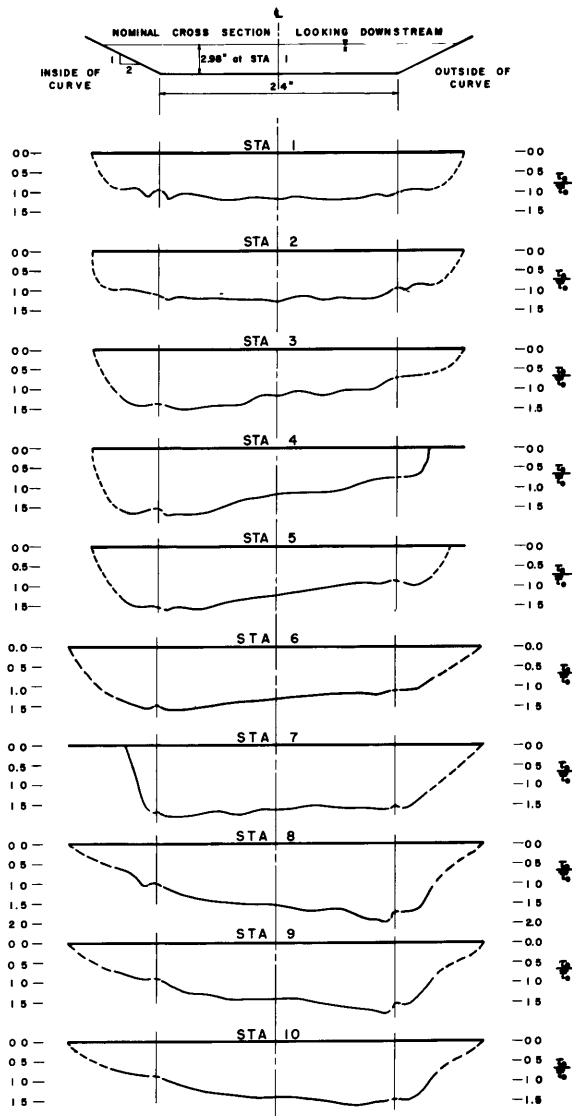
$$\frac{\tau_x}{\tau_1} = \frac{\tau_x}{\tau_0} = \frac{1}{P} \int \left(\frac{\tau_0}{\tau_0} \right) dP|_x. \quad (14)$$

In the same figure, the variation in C_f is plotted as C_{f_x}/C_{f_1} .

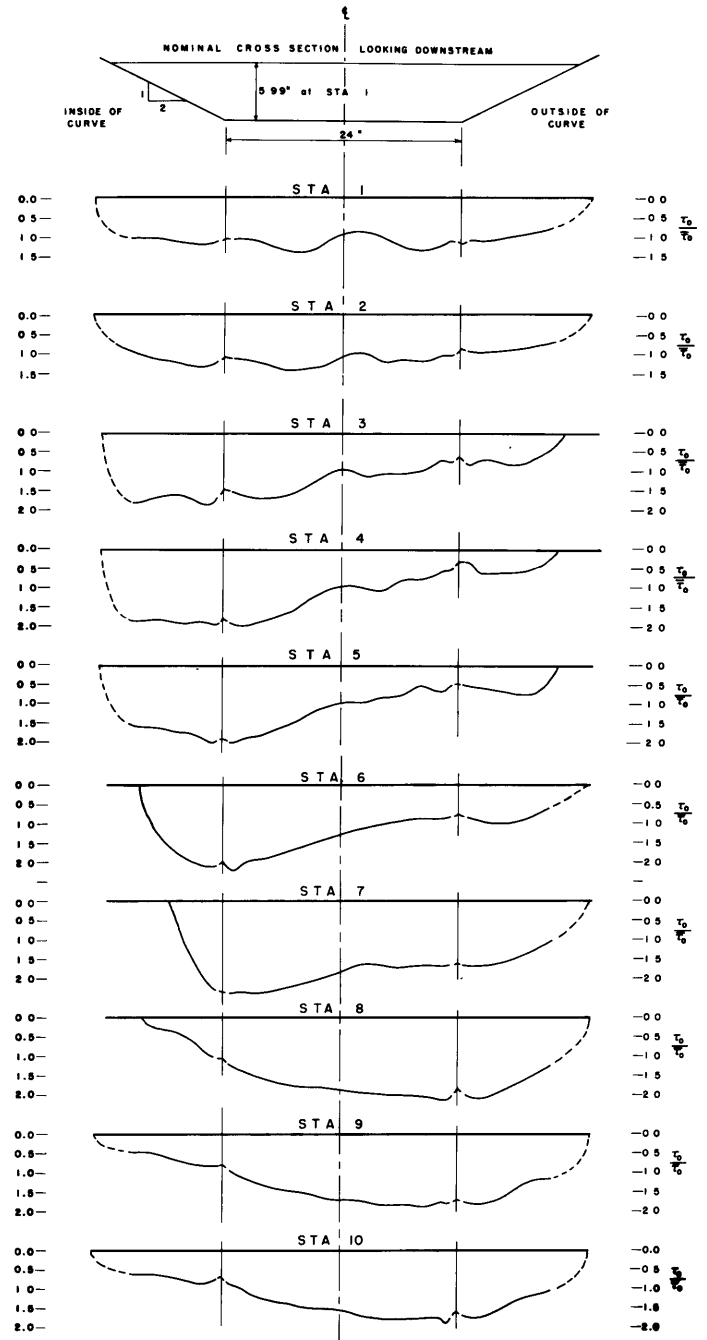
The foregoing relationships may be applied to give an approximation of the additional head loss for flow through the curve. By integration of the τ_x/τ_1 curves, the average relative shear stress, $\bar{\tau}_L/\tau_1$, may be determined over the test reach of length, L . These computations were performed for the test series, Runs 1-7. The average relative shears so obtained are presented in Table IV and Figure 35, which shown the variation with relative curvature. From the proportionality shown in Equations (13) between τ_x and S_{e_x} ,

$$\frac{\bar{S}_{e_L}}{S_{e_1}} = \frac{\bar{\tau}_L}{\tau_1}. \quad (15)$$

Since \bar{S}_{e_L} is the average energy gradient over the test reach, the difference, $(\bar{S}_{e_L} - S_{e_1})$, represents the average increase in head loss per unit length over the normal rate of head loss assumed here as existing



(a) Run No. 1



(b) Run No. 4-B

Figure 33. Shear Distribution by Section Showing Local Values of $\tau_0/\bar{\tau}_0$.

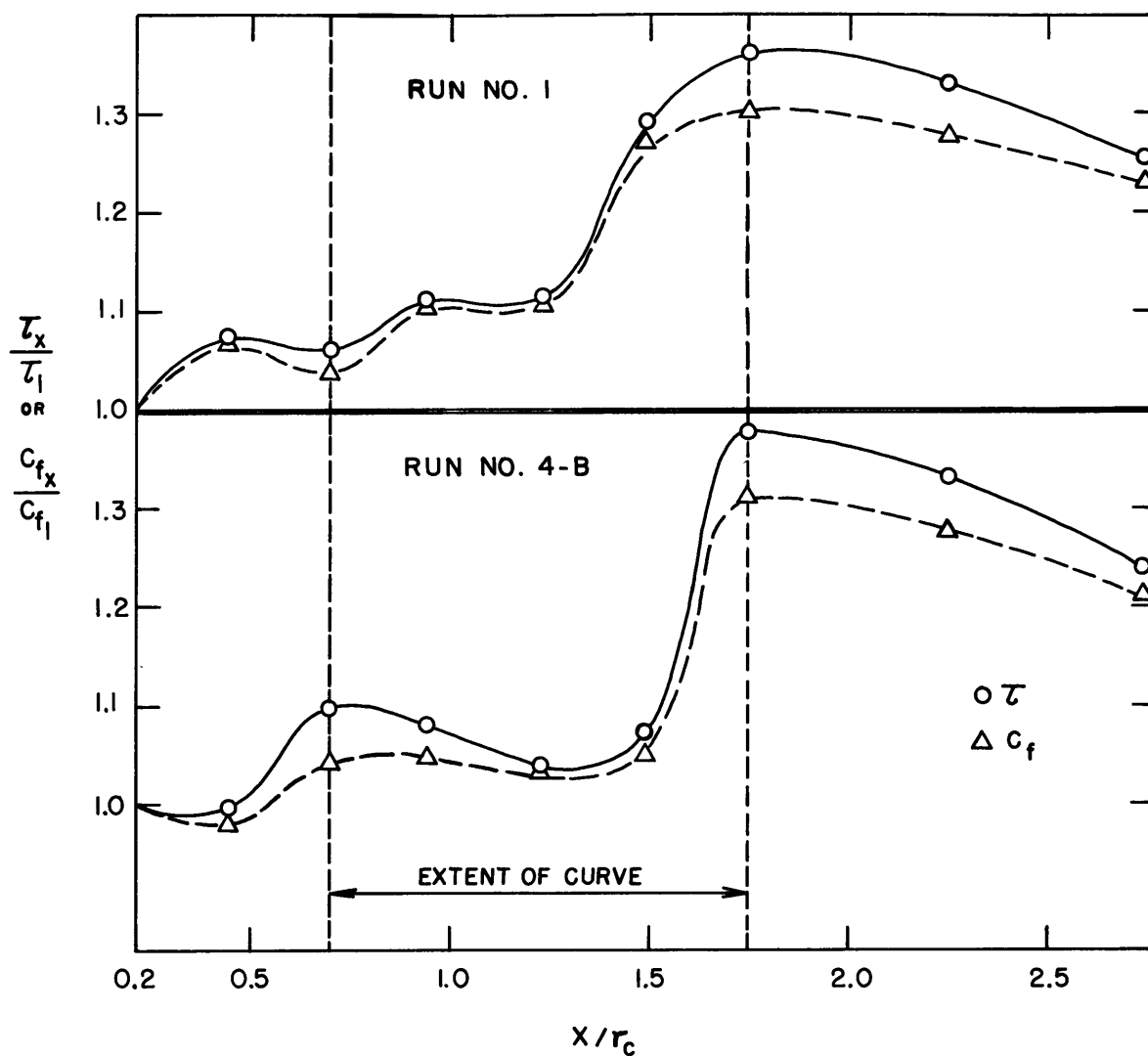


Figure 34. Longitudinal variation in the average rate of energy dissipation through the curve, shown for Runs 1 and 4-B.

TABLE IV

Energy Dissipation in the Test Reach

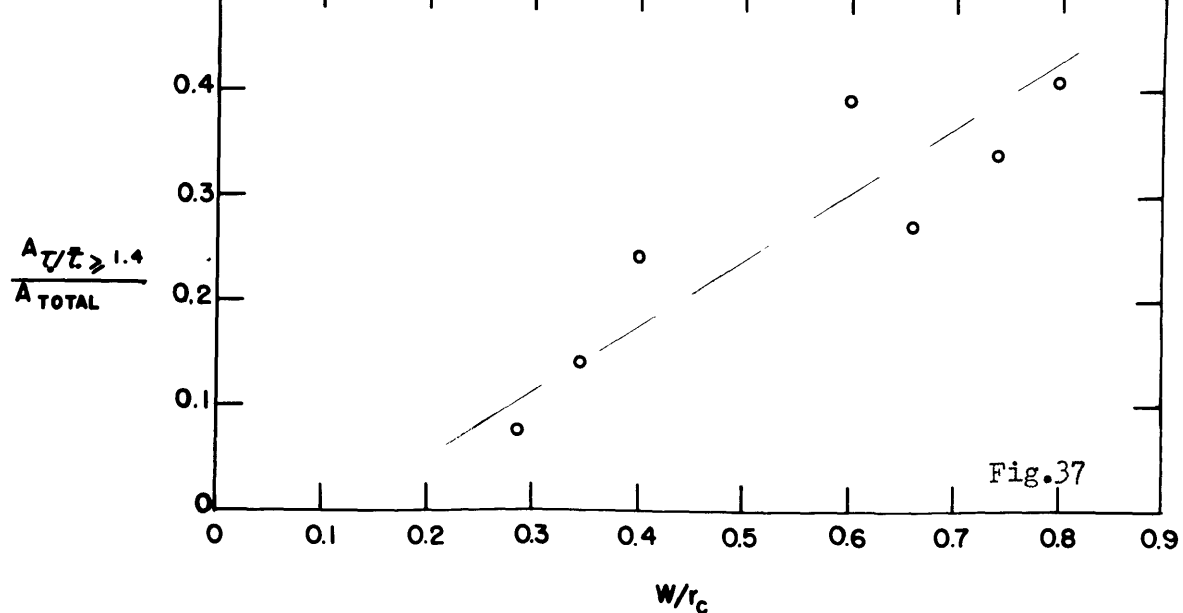
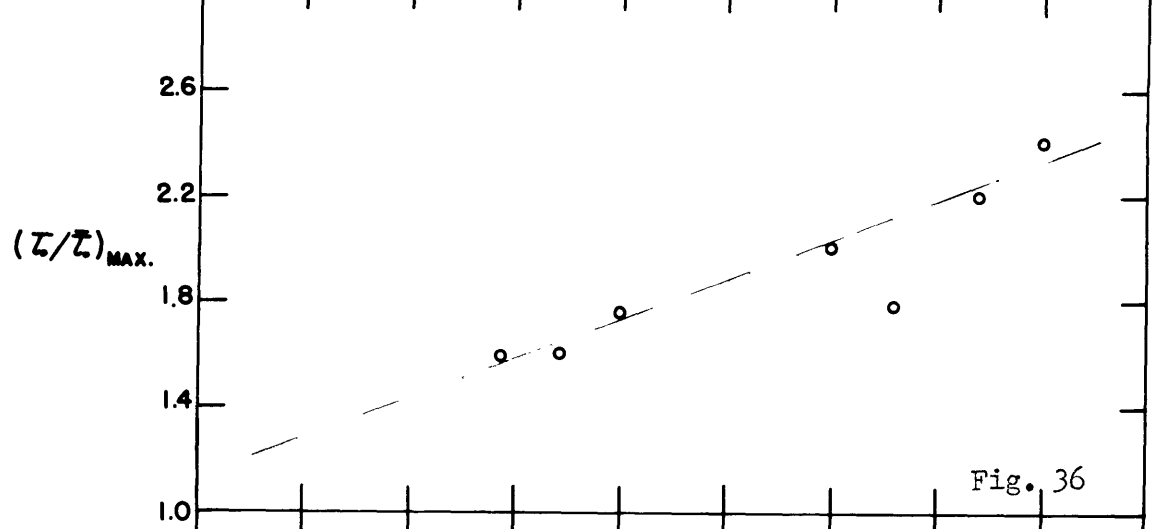
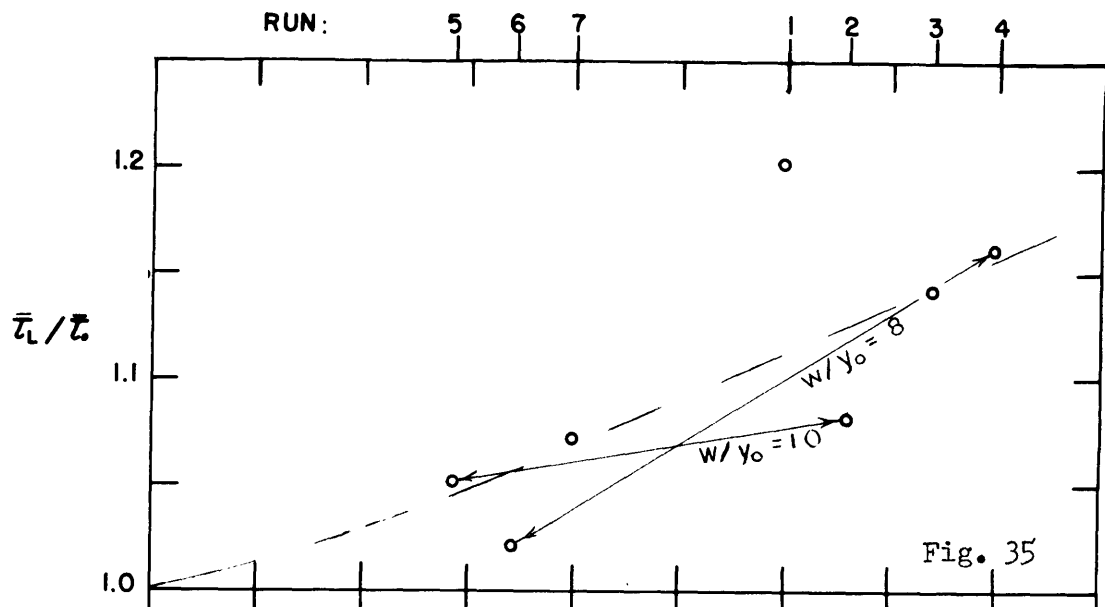
Run No:	Average shear stress at Station 1: $\tau_1 = \bar{\tau}_0, \text{lb/ft}^2$	Average relative Shear over the Test Reach: $\bar{\tau}_L / \tau_1$	Fractional excess energy dissipation over the Test Reach: $\frac{\bar{S}_{eL} - S_{e1}}{S_{e1}}$	Maximum local relative shear measured within the Test Reach: $\left(\frac{\tau_0}{\tau_1}\right)_{\text{max.}}$
1	0.0070	1.20	0.20	2.00
2	0.0087	1.08	0.08	1.78
3	0.0101	1.14	0.14	2.20
4-B	0.0060	1.16	0.16	2.40
5	0.0034	1.05	0.05	1.60
6	0.0055	1.02	0.02	1.60
7	0.0074	1.07	0.07	1.75

12/10

Figure 35. The variation with stream curvature of the average rate of energy dissipation in the test reach, expressed as $\overline{\tau}_L/\tau_L$. Runs 1-7.

Figure 36. The variation with stream curvature of the magnitude of the maximum relative shear stress measured in the test reach, $(\tau_o/\overline{\tau}_o)$ max. Runs 1-7.

Figure 37. The fraction of the test reach area affected by stresses of magnitude $\tau_o/\overline{\tau}_o$ 1.4. Runs 1-7.



at Station 1. The relative average excess head losses are shown for these tests in Table IV. Due to variation in the location of Station 10 in several of the tests, these computations are based on a test reach extending from Stations 1-9.

It is appreciated that this method as applied here can only give a very approximate value for the rate of energy loss caused by the curve, since the normal friction slope is probably higher than the one determined for Station 1. Also, the straight length downstream of the curve was not adequate to follow the return of the shear stresses back to normal values. However, other methods of determining the net head loss (e.g. the analysis of variation in specific head) are subject to the same difficulty of inadequate tangent lengths of channel and involve the measurement of surface gradients. With the flow conditions employed, these measurements could not be made accurate enough to give consistent results, and hence this approach of evaluating the head loss due to the curve was abandoned in favor of the direct application of the boundary shear stresses.

The effect of a curve is similar to that produced by any resistance which might exist in a straight channel, such as a sill, bridge pier, or a reach of increased roughness. Such a resistance to the flow will cause decreased velocities and increased depths, resulting in an upstream storage of potential energy. The excess energy dissipated in the curve is obtained from the backwater, or storage, reach upstream, where there is a compensating reduction in the total energy dissipated on the stream bed. At some distance below the curve, the flow will again return to normal conditions. Thus, for straight approach and exit reaches of sufficient length, there would be no net excess energy loss

through the curve. This is a general rule which may be stated for any obstruction or resistance in an open channel.

Therefore, a major difficulty in determining the excess rate of energy dissipation due to a curve lies in the definition of the total reach over which the loss is measured. In order to make open channel tests comparable to investigations on pipe bends, the best definition should probably be based on a reach starting above the curve at the point of maximum specific energy, and extending downstream to the point at which uniform flow is re-established. The exact location of the downstream point, as long as it lies in the region of uniform flow, is not critical. However, since the upstream point of measurement is determined by the backwater curve, it is clear that error in the location of this point will modify the measured results accordingly.

In the light of the above argument, it is to be expected that the boundary shear stress measured at Station 1 should be lower than the average shear stress, γRS_e , computed for a uniform flow. The short length of the test channel makes it impossible to evaluate γRS_e accurately, but, as shown in Table II, the measured values of $\overline{\tau}_0$ (at Station 1) are consistently lower than the estimated average shear stress, γRS_e .

It is seen from Figure 34, in which τ_x/τ_1 is equivalent to the ratio S_{e_x}/S_{e_1} , that the energy dissipation is only moderately increased in the upstream portion of the curve. Near the curve exit, however, the shear stresses rise sharply with the shift of momentum to the outer bank, and these high shears decrease only slowly towards the normal value in the channel section below the curve. In preparing the plots to determine $\overline{\tau}_L$ for the tests at lower curvature, Runs 5-7, it was found that within the early part of the curve the average shear, τ_x/τ_1 , decreases to a

value of about 0.92, before increasing towards the exit. The implication from this is that for decreasing curvature, the storage reach may extend further into the bend. The resistance of the curve lies primarily in the zone in which the irrotational pattern breaks down. Thus, as long as the flow through the curve takes place without separation, and essentially in accordance with an irrotational pattern, average energy losses remain moderate within the curve itself. The greatest part of the loss occurs below the point of breakdown, over a reach extending well below the curve.

The relative amounts of the loss which occur within the curve proper and over the downstream reach vary with the geometry of the bend. Ito (21) has shown that in pipe bends of large curvature, as much as 90% of the bend headloss may take place in the downstream tangent. However, for moderate curvatures ($d/r_c \approx 0.2$), only about 40% of the energy is dissipated in the sequent reach, due to the reduction in the disturbance generated by the curving boundary.

The general trend indicated in Figure 35 suggests an increase in excess dissipation with increasing curvature. Because of the small number of tests available for this comparison and the relatively large scatter of the points, no attempt was made to give concise formulation of this trend. Intuitively such a trend is quite plausible; at zero curvature, the resistance is that of a straight channel, $\overline{\tau}_I/\tau_1 = 1$, while at maximum curvature the resistance should attain a maximum (finite) value.

Previous investigations on losses through bends in pipes (2), as well as in open channels (26), have revealed that there may occur an anomaly in the rate increase of bend resistance with increasing curvature. For bends of constant roughness and deflection angle it appears that, with increasing curvature, there exists an intermediate condition of relative

minimum resistance. The critical value of curvature at which this anomaly occurs has not been clearly defined, nor has its cause been adequately explained. It is recognized that the deviation of Runs 1 and 2 from the general trend of increasing resistance may be an indication of this phenomenon in the open channel tests. However, it is felt that because of the small amount of available data, there is no justification in this case for assuming such a discontinuous behavior.

In concluding this discussion it can be stated that the mean loss coefficients determined for flow through curves from the usual hydraulic measurements give an inadequate indication of the maximum intensities of local shear stresses. For flow through single curves, the maximum local shears were found to exceed the mean initial shears by over 100%, while mean sectional shear stresses were only of the order of 35% larger than the mean stresses at the entrance of the curve. For conditions of increasing curvature, there is an increasing trend in the mean sectional shears as well as in the total relative resistance of the entire curved reach.

E. Scour Patterns in Alluvial Streams

In the previous section the energy dissipated by a curving stream was discussed in terms of an average resistance over the total curved reach. While this approach is of interest in considering the role of boundary geometry on the overall energy balance of the stream, it tends to obscure the local conditions controlling the scour pattern. From a comparison of the shear maps with the mean values shown in Figures 34 and 35, it is clear that in an erodible channel localized areas of scour should be expected at various sections for which the mean shear stress is not critically high.

For the understanding of scour patterns, therefore, it is probably more logical to consider the variation in magnitude of some parameter of local shear as a function of bend geometry. In Figure 36, the magnitude of the maximum measured shear stress for Runs 1-7 is plotted against relative curvature, w/r_c . Because of the statistical uncertainty of actually determining an extreme value in these tests, the quantitative validity of Figure 36 is subject to question. However, the trend is clear, and it may be concluded that, in an erodible trapezoidal channel, these would represent points at which erosion would first appear. As noted in the earlier discussions, with increasing curvature this point of initial scour moves to a position further upstream. On the basis of these tests, this shift is apparently quite abrupt, occurring at a curvature in the range $0.67 < w/r_c < 0.73$.

An additional parameter which may also be relevant in an approach to the problem of channel stability and the design of revetments, is the variation in areal extent of a zone subjected to shears greater than some

critical magnitude. Consider, for example, the zones in the curved reach (Runs 1-7) enclosed by the contour $\tau_o/\bar{\tau}_o = 1.4$. These areas, expressed as a fraction of the area of the test reach, are plotted in Figure 37. As might be expected, the relative area exposed to shears equal to or greater than a given value increases with increasing curvature. For channels of fixed boundary geometry (Runs 1-4, or 5-7), the increase in depth and curvature at flood conditions will lead to scour which is increased both in extent and intensity.

Before it becomes feasible to apply these experimental results directly to natural streams, further information is needed on the effects of boundary deformation on the pattern of scour. It is evident that, at a point of high local shear stress, scour will occur. It cannot be predicted, however, to what degree the resulting boundary depression will modify the shear either at the point or in the surrounding area. In addition, the deposition which may be expected in the zones of reduced shear should further modify the flow pattern by localized aggradation of the boundary.

The variation in erodibility of sorted sediments adds still another complicating factor to this problem. Sundborg (43) has shown that the sorting of a heterogeneous bottom sediment depends on the size range as well as on the particle shapes and the nature of the sediment mixture. In some sediments, the fine material is winnowed out, leaving an erosion pavement which can withstand much higher shears. Under other conditions the residual sediment is comprised of the finer material, which may then develop into ripples and thus alter the effective bottom roughness. Valuable information could be gained from both laboratory and field work in which systematic studies were made to determine the sorting of bottom

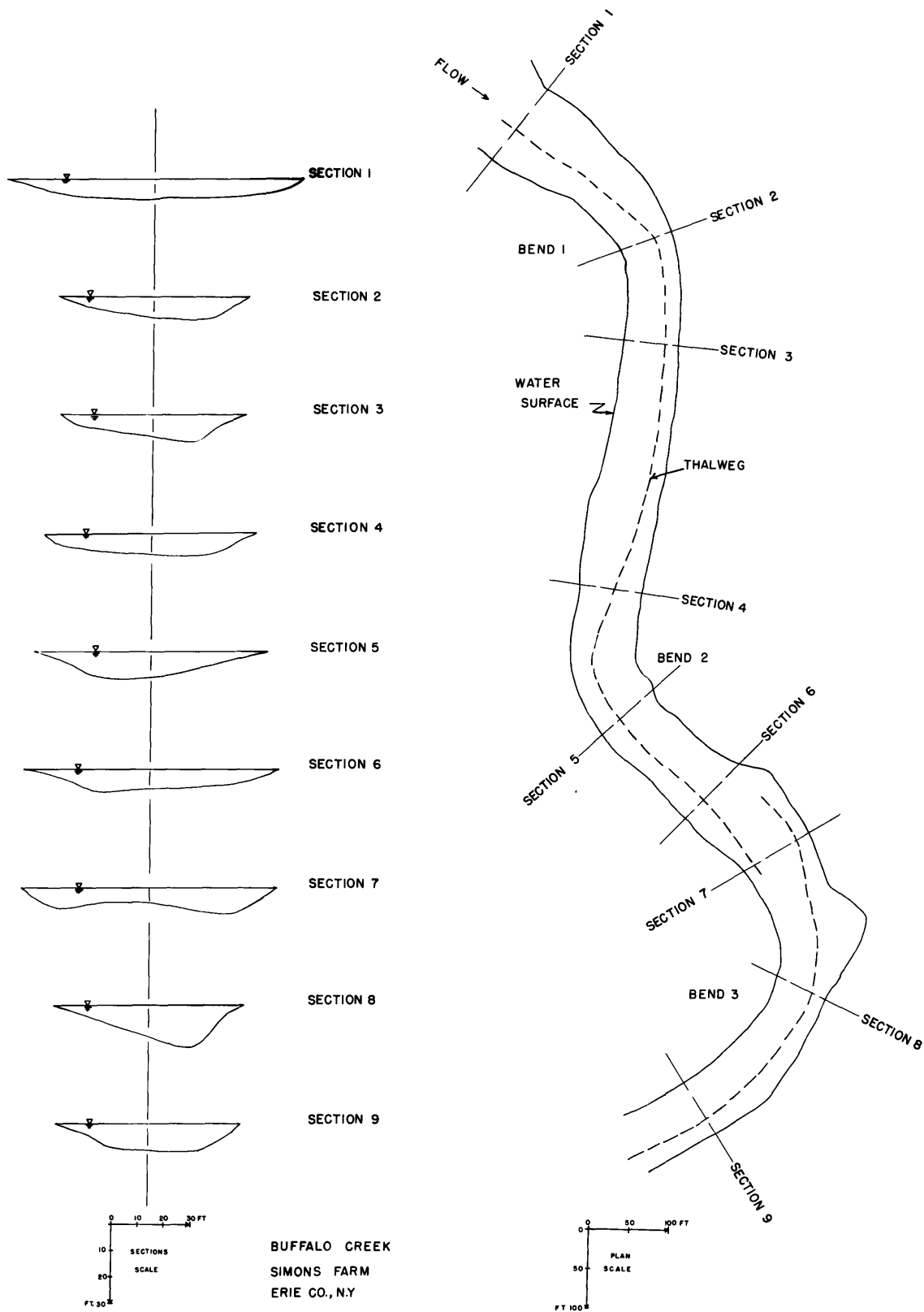
sediments under varied shear stresses. Of particular interest to the present study would be data on the size distribution across transverse sections in stream bends. As far as could be determined, this work has never been done.

In spite of these still unsolved problems a quite logical relationship can be observed between the scour patterns in alluvial streams and the boundary shear distributions measured in the channel experiments. Figure 38* shows a short reach of Buffalo Creek, Erie County, New York, in an area where the stream flows through an unconsolidated mixture of glacial sands and silty clays. The stream discharge of 2,500 cfs to which the map corresponds is based on the approximate conditions of annual spring flooding.

By comparison of the section profiles with the map, the scour pattern through the reach can be observed. Before each bend the stream assumes an approximately trapezoidal shape, indicating a symmetrical flow distribution. The tendency for the flow to cross to the outer bank under the influence of the helicoidal motion extends quite far upstream in each bend, as evidenced by the early dislocation of the thalweg. Between the second and third bends, an oblique bar is evident at the crossing point, with a discontinuity of the thalweg. This is a type of bar configuration which is common to many sinuous streams. The scour extending down to the inner bank of Bend 3 is due to the tendency to irrotational motion of the flow entering the curve, as well as to the asymmetry of the flow leaving Bend 2. A similar condition may be observed for the reverse curve tests in the channel, Figures 30, 31. In these

*This material was supplied to the author in personal transmittals by Messrs. D. A. Parsons and R. P. Apmann, of the Agricultural Research Service.

Figure 38. Sketch map and lateral sections of an alluvial stream, showing the course of the channel of maximum scour.



BUFFALO CREEK
SIMONS FARM
ERIE CO., N.Y.

SECTIONS ARE AT 2500 CFS
F AT 2500 CFS = 0.25

BEND NO.	1	2	3
$\theta \approx$	60°	60°	110°
l/w	5.0	3.5	4.5

Figure 38

bends of moderate curvature, the helicoidal motion should be developed early in the curve, and the deeper channel on the concave bank is thus extended quite far upstream.

In closing the discussions of these experiments it may be remarked that the magnitudes of the measured shears which might be expected to cause bank instability compare favorably to field observations on erosion in curves. Lane (22) set forth stability criteria based on tractive force studies conducted in unlined channels. For canals ranging in curvature from straight to very sinuous, the stability criterion is given as a fractional reduction in the permissible tractive force. It is stated that for very sinuous canals, the permissible tractive force (equivalent to $\overline{\tau}_0$) is reduced by a factor of 0.6. Thus, the maximum relative tractive force to be expected in such curves is $\tau_0/\overline{\tau}_0 = 1/0.6 = 1.7$.

The degree of curvature as defined by "very sinuous" corresponds to the areal configuration "typical of canals in foothills or mountainous topography" [(22), p.1257]. A reasonable estimate of curvatures for such streams appears to be of the order of $0.4 < w/r_c < 6$. While the maximum shears measured in the channel are somewhat greater than this, the agreement is quite good.

It may be concluded that the local tractive forces measured under these simplified channel conditions do provide a useful indication of the distribution and intensity of erosive attack on the boundaries of alluvial channels. In order to establish closer correlation between the laboratory and field conditions, further effort should be directed towards two major areas: (1) observation techniques leading to more concise quantification of field data and (2) the interaction between flowing water and the stream sediments. The latter problem includes the role of entrained

sediment as it modifies the dynamical properties of the transporting fluid, as well as the effect of boundary alteration arising from movement of the bed material.

VI. CONCLUSIONS

The results of this investigation of flow through curved trapezoidal channels permit a number of important conclusions.

A. Flow through single curves.

1. For channels composed of a single 60 degree curve with straight approach and exit tangents, the flow pattern within the curve tends to conform to that of a free vortex. Boundary layer effects, combined with the centripetal acceleration in the curving flow, cause a trend to separation along the concave bank near the curve entrance, and a more pronounced separation zone originating at the convex bank towards the exit of the curve. In addition to separation, the frictional effects produce the expected helicoidal motion.

2. The two frictional aspects of the flow, separation and the secondary, helicoidal current, tend to produce a breakdown in the irrotational type of motion, with the ultimate establishment of high velocities along the concave bank. The section of the curve at which the stream momentum is transferred from the inner to the outer bank varies with the bend geometry. This crossover point occurs earlier in the curve for streams of decreasing curvature. Under conditions of greatest curvature, the irrotational type of pattern prevails throughout the curve itself, and at the exit section the crossover is abrupt, due to the large separation zone on the inner bank.

3. The distribution and the magnitudes of the boundary shear stresses produced by the curved flow cannot at present be predicted quantitatively, either by theory or by correlation with measured velocity distributions. In general, the locations of the shear

maxima were found to be associated with the course of the filament of highest velocity and with the zones of locally accelerated motion. Thus, high stresses are found along the inner part of the curve, and near the outer bank below the curve exit, with a strongly asymmetrical shear distribution persisting for a considerable distance in the downstream tangent reach.

4. The location and the relative intensity of the maximum local shear stress in a curve are controlled primarily by the stream geometry. For streams of increasing curvature, the relative magnitude of the shear maximum increases, and it tends to occur earlier in the curved reach. For the range of curvatures studied in the smooth channels, $0.29 < w/r_c < 0.8$, the shear maximum increased from $\tau_o/\overline{\tau_o} = 1.6$ to 2.4.

5. The total head loss for the curve, as well as the average rates of loss at sections throughout the curved reach, may be computed from the measured shear distributions. This one-dimensional treatment of the flow gives inadequate indication of either the intensities or the peripheral locations of the highest shears; however, it demonstrates that the excess stream energy dissipated due to a curve increases with increasing curvature.

6. The introduction of boundary roughness does not appear to modify the shear pattern within the curve itself. However, in the downstream reach below the crossover point, the shears are substantially higher, due to the greater development of the helicoidal motion over the rough boundary.

B. Compound Curve Systems.

1. The technique of simulating the effects of upstream curvature by artificially reproducing the related velocity distributions in

the approach channel has proved to be useful and economical for establishing shear patterns for compound curves. The quantitative validity of this method remains subject to detailed confirmation.

2. The effect of a reversed curvature is simulated with high velocities near the inside bank at the entrance section. This condition reinforces the free vortex pattern, increasing the super-elevation to a slight degree. High shear stresses are produced along the inner bank. Separation towards the exit section is prevented and thus a more symmetrical flow condition exists in the downstream tangent with shear stresses much reduced as compared to the case of the single curve.

3. With high velocities produced near the outside bank at the entrance section a double curve configuration is simulated with a short straight section between the curves. This approach condition suppresses the free vortex pattern in the curve, a larger separation zone is formed near the inside bank, and higher shear stresses are encountered along the outer bank throughout the test reach than for the single curve.

4. In general it may be concluded that longer curves will not materially increase maximum shear intensities; by contrast, reversal of curvature in compound systems leads to a substantial increase in local shear intensity. The absolute maximum relative shear stress was observed to be 3.0 in the simulated reverse curve.

C. General Observations.

1. For stream bends of moderate curvature, the super-elevation of the water surface is quite insensitive to variation in the radial distribution of velocities, and may be predicted adequately by a one-dimensional treatment of the flow. The total super-elevation appears to be a function only of the mean momentum of the stream, and the relative

curvature of the bend.

2. For a given channel alignment the relative shear patterns in a curve are in general not greatly modified by variations in depth and velocity at the curve entrance, but seem to depend primarily on the boundary geometry. For the range of flow conditions which can occur in a trapezoidal channel, the intensities and the areal extent of the highest shears increase with increasing depth and curvature.

3. This study has demonstrated the importance of boundary shear stress patterns with respect to the ultimate understanding of erosion and deposition processes in channel curves. It has been shown that the trends in the measured shear distributions conform quite closely to the scour patterns observed in sinuous alluvial streams, and that, insofar as the limited field data permit a comparison, the magnitudes of the measured stresses suggest agreement with the intensity of the channel scour.

4. While the orientation of the shear stresses was neglected in this study and is not believed to affect the stated results, it may be concluded that it assumes considerable importance with respect to bank slope stability in channels through uniform non-cohesive materials.

5. The distribution of the shear stresses over the boundary is conveniently determined from surface Pitot tube measurements. This technique as previously developed by Preston for air flows has been successfully adapted to the present problem for smooth as well as rough boundary surfaces.

D. Recommendations for Further Research.

1. Controlling aspects of the stream geometry: The limited range of the stream and geometric parameters covered in this study does

not permit generalization of the shear distributions and magnitudes to streams of varied geometry. Additional studies are particularly necessary to evaluate the effects of variations in bend angle and channel cross section, as well as in the upstream alignment of the approach flow, which must enter into the analysis of sinuous streams.

2. The effects of sediment on the scour pattern: Until the role of stream sediment in the dynamics of erosion is clarified, the primary contributions of the present work will be towards a qualitative explanation of observed scour phenomena. Further work must be directed towards the dynamic properties of the sediment itself and the way in which it in turn modifies the properties of the transporting fluid, as well as towards the changes in the shear pattern produced by erosive deformation in the channel boundaries.

3. Energy dissipation in channel bends: For economic reasons, studies of flow through bends have generally been conducted in channels too short to permit the establishment of fully uniform conditions in the approach and exit tangents. In order to carry the analysis of this problem beyond the realm of speculation and inadequate analogy to pipe flows, an investigation should be conceived for the specific purpose of obtaining measurements of sufficient accuracy and scope to study the dissipative effects of channel curvature on the energy balance of a stream.

VII. BIBLIOGRAPHY

1. Abarbanel, S.S., Hakkinen, R.J., and Trilling, L, Use of a Stanton Tube for Skin-friction Measurements, NASA Memo 2-17-59W, 1959.
2. Anderson, A.G., Fluid Flow Diversion; A Summary and Bibliography of Literature, Univ.of Minnesota, St. Anthony Falls Hydraulics Laboratory Project Report No. 1, 1947.
3. Bagnold, R.A., The Flow of Cohesionless Grains in Fluids, Phil. Trans. Roy. Soc. A, London, No. 964, Vol. 249, 1956.
4. Bradshaw, P., and Gee, M.T., Note on the Inner Velocity Profiles of Non-equilibrium Turbulent Boundary Layers, Aero. Res. Council, ARC 20, 889, 1959.
5. Bradshaw, P. and Gregory, N., Calibration of Preston Tubes on a Flat Plate using Measurements of Local Skin Friction, Aero. Res. Council, ARC 20, 199, 1958.
6. Dhawan, S., Direct Measurements of Skin Friction, NACA Report 1121, 1953.
7. Eagle, H.C. and Wilson, W.F., Differential Manometers Investigated, Civil Engrg. Vol. 4, pp. 30-32, 1934.
8. Einstein, H.A. and Harder, J.A., Velocity Distribution and the Boundary Layer at Channel Bends, Trans. AGU, Vol. 35, No. 1, 1954.
9. Elata, C. and Ippen, A.T., The Dynamics of Open Channel Flow with Suspensions of Neutrally Buoyant Particles, Massachusetts Institute of Technology Hydrodynamics Laboratory Technical Report No. 45, 1961.
10. Enger, P.F., Tractive Force Fluctuations around an Open Channel Perimeter as Determined From Point Velocity Measurements, paper presented at ASCE Convention, Phoenix, Arizona, April 10-14, 1961.
11. Fage, A. and Faulkner, V.M., An Experimental Determination of the Intensity of Friction on the Surface of an Aerofoil, Proc. Roy. Soc. A, London, Vol. 129, p. 378, 1930.
12. Fenter, F.W. and Stalmach, C.S., Jr., The Measurement of Turbulent Boundary Layer Shear Stress by Means of Surface Impact-pressure Probes, J. Aero. Space Sci., 25, 12, 793-794, 1958.
13. Friedkin, J.F., A Laboratory Study of the Meandering of Alluvial Rivers, U.S. Waterways Experiment Station, 1945.
14. Gibson, A.H., Hydraulics and its Applications, London Constable and Co., Ltd., 4th Edition, 1945.

15. Givler, C.A., Measurement of Boundary Shear in an Open Channel Curve with a Surface Pitot Tube, SM Thesis, MIT (unpublished), 1959.
16. Granville, P.S., The Determination of the Local Skin Friction and the Thickness of Turbulent Boundary Layers from the Velocity Similarity Laws, David Taylor Model Basin Report 1340, 1959.
17. Hakkinen, R.J., Measurements of Turbulent Skin Friction on a Flat Plate at Transonic Speeds, NACA T.N. 3486, 1955.
18. Hsu, E.Y., The Measurement of Local Turbulent Skin Friction by Means of Surface Pitot Tubes, David Taylor Model Basin Report 957, 1955.
19. Ippen, A.T., Drinker, P.A., Jobin, W.R., and Noutsopoulos, G.K., The Distribution of Boundary Shear Stresses in Curved Trapezoidal Channels, MIT, Hydrodynamics Laboratory Technical Report No. 43, 1960.
20. Ippen, A.T. and Mitchell, M.M., The Damping of the Solitary Wave from Boundary Shear Measurements, MIT Hydrodynamics Laboratory Technical Report No. 23, 1957.
21. Ito, H., Pressure Losses in Pipe Bends, Trans. ASME, J. Basic Engrg. Paper No. 59-Hyd 4, 1959.
22. Lane, E.W., Design of Stable Channels, Trans. ASCE, vol. 120, p. 1234, 1955.
23. Lane, E.W. and Borland, W.M., River-bed Scour During Floods, Trans. ASCE, Hyd. Division, Vol. 119, p. 1069, 1954.
24. Leliavsky, S., An Introduction to Fluvial Hydraulics, Constable and Co., Ltd., London, 1955.
25. Leighly, J.B., Toward a Theory of the Morphologic Significance of Turbulence in the Flow of Water in Streams, Univ. of Calif., Publication in Geography, Vol. 6, pp. 1-22, 1932.
26. Leopold, L.B., Bagnold, R.A., Wolman, M.G., and Brush, L.M., Jr., Flow Resistance in Sinuous Channels, U.S.G.S. Professional Papers 282-D, and 282-E (R.A. Bagnold), 1960.
27. Leopold, L.B. and Maddock, T., The Hydraulic Geometry of Stream Channels and some Physiographic Implications, U.S.G.S. Professional Paper 252, 1953.
28. Leopold, L.B. and Wolman, M.G., River Meanders, Bull. Geol. Soc. Am., Vol. 71, p. 769, 1960.
29. Liepmann, H.W. and Skinner, G.T., Shearing-stress Measurements by use of a Heated Element, NACA T.N. 3268, 1954.
30. Ludweig, H., Instrument for Measuring the Wall Shearing Stress of Turbulent Boundary Layers, NACA T.M. 1284, 1950.

31. Mockmore, C.A., Flow around Bends in Stable Channels, Trans. ASCE Vol. 109, p. 593, 1944.
32. Nece, R.E., Givler, C.A., and Drinker, P.A., Measurement of Boundary Shear Stress in an Open Channel Curve with a Surface Pitot Tube, MIT Hydrodynamics Laboratory Technical Note No. 6, 1959.
33. Nikuradse, J., Laws of Flow in Rough Pipes, NACA T.M. 1292 (originally published in German 1933), 1950.
34. Noutsopoulos, G.K., Velocity and Boundary Shear Distributions in an Open Channel Bend, SM Thesis, MIT (unpublished), 1960.
35. Olsen, O.J. and Florey, Q.L., Sedimentation Studies in Open Channels, Boundary Shear and Velocity Distribution by the Membrane Analogy, Analytic, and Finite-difference Methods, Bureau of Reclamation Structural Lab. Report No. SP-34, 1952.
36. Parsons, D.A., Effects of Flood Flow on Channel Boundaries, Proc. ASCE, Vol. 86, paper Hy 4, 1960.
37. Preston, J.H., The Determination of Turbulent Skin Friction by Means of Pitot Tubes, J. Roy. Aero. Soc., Vol. 54, pp. 109-121, 1954.
38. Schlichting, H., Boundary Layer Theory, Pergamon Press (McGraw-Hill Book Co.), Inc., New York, 1955.
39. Shukry, A., Flow around Bends in an Open Flume, Trans. ASCE, Vol. 115, p. 751, 1950.
40. Smith, D.W. and Walker, J.H., Skin-friction Measurements in Incompressible Flow, NASA T.R. R-26 (supersedes NACA TN 4231), 1959.
41. Stanton, T.E., Marshall, D.S., and Bryant, C.N., Proc. Roy. Soc. A, Vol. 97, pp. 422-434, 1920.
42. Steinberg, I.H., Russian River Channel Works, Proc. ASCE, J. Waterways and Harbors Div., WW4, No. 2647, 1960.
43. Sundborg, A., The Riber Klaralven, a Study of Fluvial Processes, Inst. of Hydr., Roy. Inst. of Tech., Stockholm, Bull., 52, 1956.
44. Thompson, J., On the Origin and Winding of Rivers in Alluvial Plains, Proc. Roy. Soc., London, 1876.
45. Vanoni, V.A. and Nomicos, G.N., Resistance Properties of Sediment Laden Streams, Proc. ASCE, J. Hyd. Div., Vol. 84, paper No. Hy5, 1959.
46. Woodward, S.M., Hydraulics of the Miami Flood Control Project, State of Ohio, The Miami Conservancy District, Technical Reports Part VII 1920.
47. Young, A.D. and Maas, J.N., The Behavior of a Pitot Tube in a Transverse Total Pressure Gradient, Aero. Res. Council Repts. and Memo. No. 1770, 1937.

VIII. APPENDIX

A. The Test Channel Facility

The general construction plan of the test unit is shown in Figure A-1. The basic channel is a trapezoidal trough of reinforced concrete consisting of a straight approach section 20 feet in length, a 60 degree curve of 5-foot centerline radius, and a straight 10-foot exit section. The channel, which was precast in short sections, is supported on a segmented steel framework, the two straight reaches and the curve being mounted as three separate units. Each frame unit rests on jackscrews, permitting adjustment of the slope to a maximum of 1.4%.

Longitudinal guide rails, with adjustable supports set into the concrete serve as tracks on which to mount instrument carriages. The rails, which are accurately set to line and grade, also guide template blades used in shaping the channel section. Carriage alignment in the curve is provided by a center pivot and radius arm (Figure A-3).

Test channels up to 5 feet in width may be formed in the concrete bed. For this purpose two different lining materials were used in these tests. In the larger channel, Figure 3a, the lining material used was a mixture of plaster, lime, and portland cement (2:2:1 by dry volume), which can be easily worked after the initial plaster setting, but which becomes quite hard after the cement has set. In laying the smaller channel, Figure 3a, a filler mix of lean concrete (1:8) was applied, followed by a finish coat of a resin-base patching cement.*

The finished channels were shaped by trapezoidal blades mounted on the guide rails. After the surface had cured, it was sandpapered

*Larsen Mix, Larsen Products Corp., Bethesda, Maryland

carefully and covered, by brush application, with a liquid vinyl coating** which dries to a smooth, tough, elastic film.

The centerline slope of the unit was set during initial construction at $0.00064 = 1/1563$, and the mechanical adjustment was not changed throughout the test series. The slope was checked, after completion of the larger channel, by closing the channel exit and measuring the depth of the impounded water at intervals along the centerline. Upon completion of the smaller channel, a similar check revealed that the slope of the approach section had decreased to 0.00055 . This difference, which amounts to an elevation change of 0.02 inches over the length of the straight channel, is thought to be due to settling of the building foundation. No attempt was made to restore the slope to its original value.

As shown in Figure A-1, the entire system is a self-contained unit comprising all the equipment necessary for water storage and recirculation as well as for the control and measurement of discharge. Flows up to 3 cfs are supplied by a 25 hp centrifugal pump. The discharge is controlled by a gate valve, and can be metered either with a calibrated orifice in the return pipe, or with a rectangular weir in the downstream bank. Gravel flow diffusers were installed to provide stilling conditions at the channel entrance and in the weir basin.

The baffle screens used in producing distorted flow patterns for the simulation of upstream curves were made from sheets of 1/4-inch mesh galvanized hardware cloth mounted in aluminum frames. For each test condition, final modifications of the flow pattern were obtained by trial and error using overlays of 1/16-inch mesh wire screening. A typical screen arrangement is shown in Figures A-4 and A-5.

** Liquid Envelope, Better Finishes and Coatings, Inc., Newark, New Jersey.

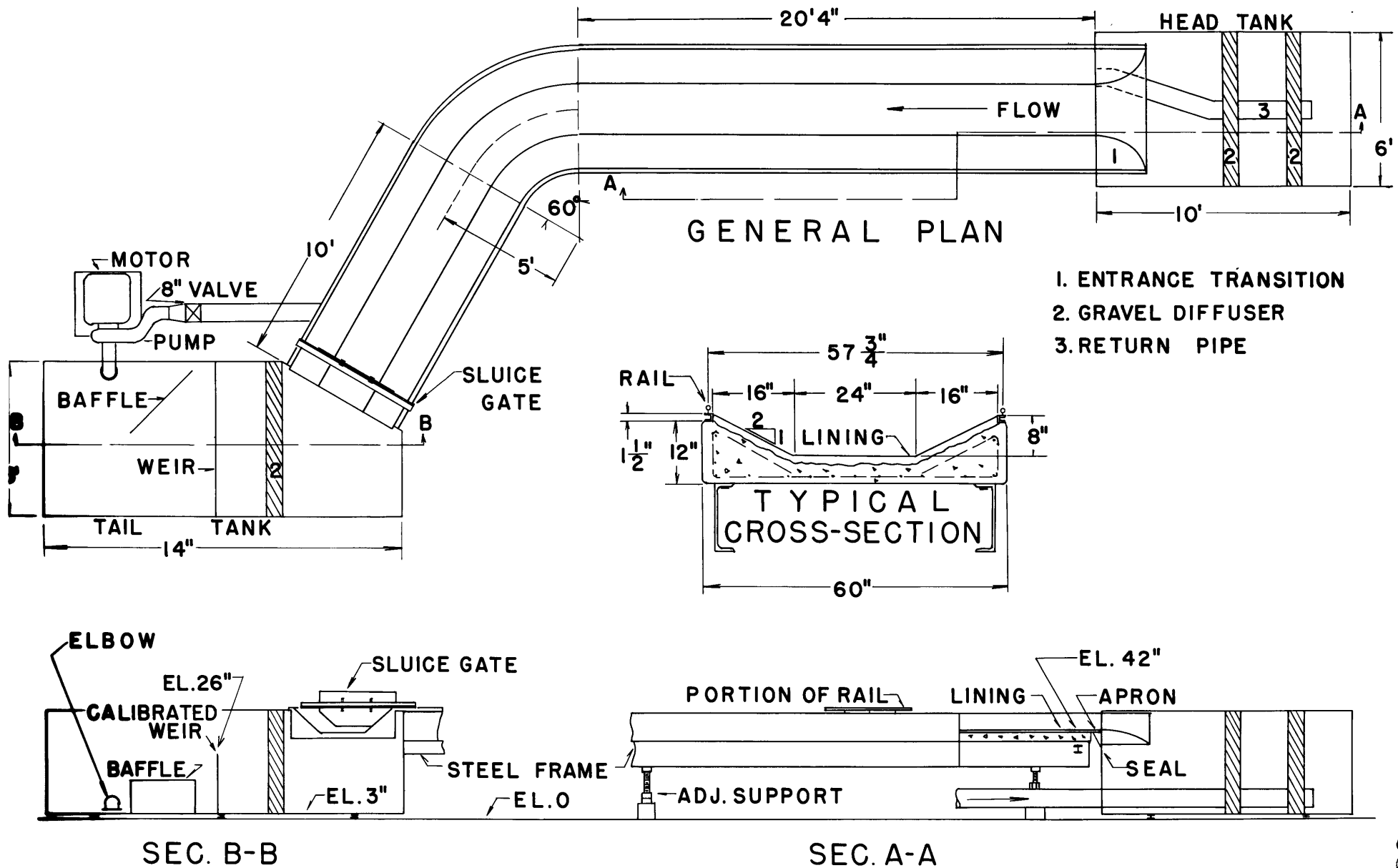


Figure A-1. General Plan of the Experimental Facility



Figure A-2. Overall View of Channel.

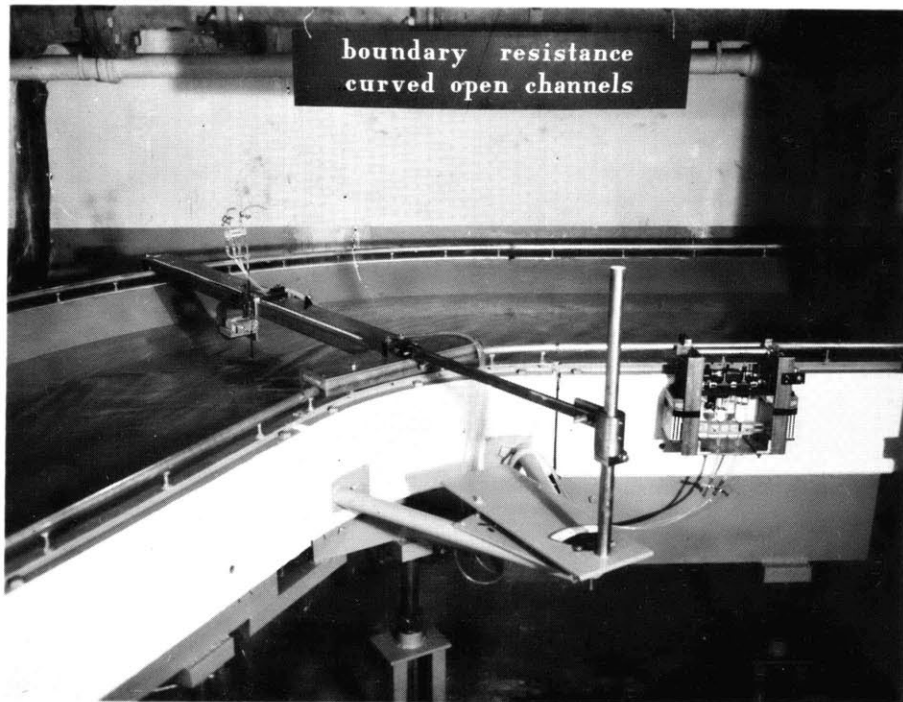


Figure A-3. Instrument Carriage Mounted in 60° Bend.

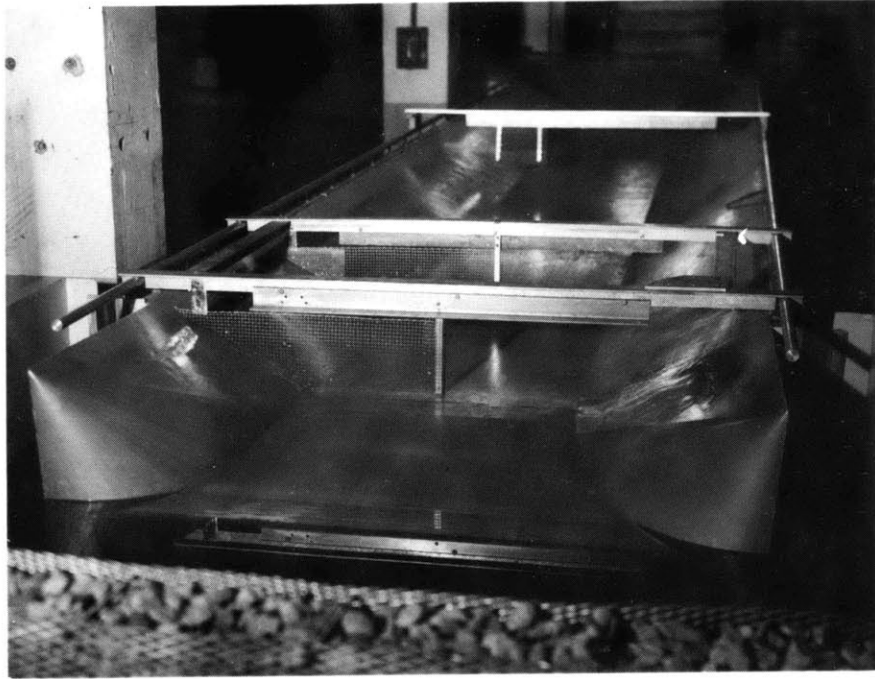


Figure A-4. Typical Screen Arrangement for Simulated Curves.

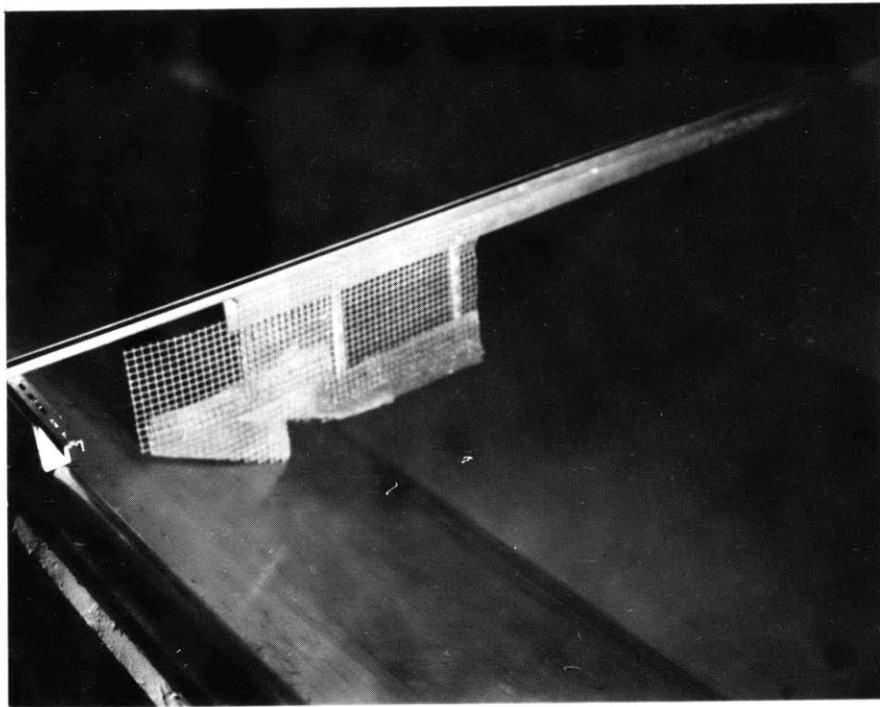


Figure A-5. Surface Drag for Simulation of Separation Zones.

B. Instrumentation

Many of the instruments developed during this investigation are of special design, and have **been reported in Reference(19)**. In the following paragraphs the major design details of these instruments are described. Their applications are discussed under the appropriate sections in the text.

1.) Velocity Measurements

The gross free stream velocity distributions were determined with a 5/16" standard design Prandtl tube and a manometer.

In order to check the calibration of the surface Pitot tubes, it was necessary to measure velocities in close proximity to the stream boundary. For this purpose, the Pitot-static tube shown in Figure A-6 was constructed.

The flattened total head tube was made from annealed stainless tubing (0.125" OD bored to 0.104" ID) compressed over 0.015" shim stock. The face was machined square and all burrs honed off. The tip dimensions were measured on a tool maker's microscope and the averages are as shown in Figure A-6b.

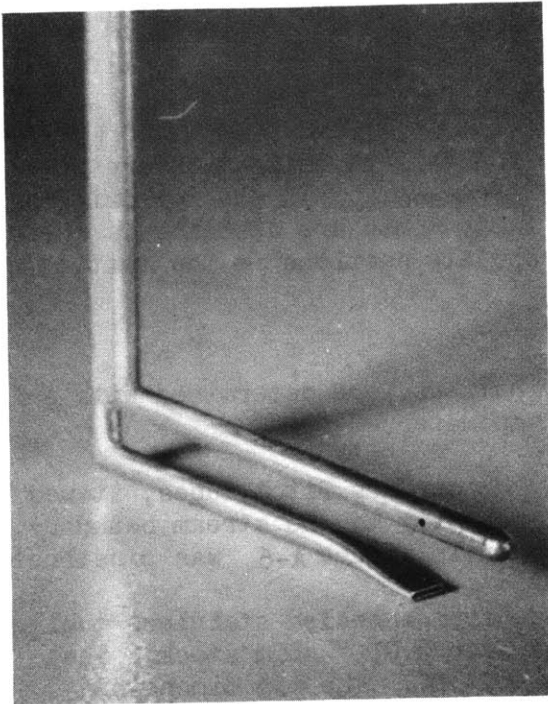
The tip is thin enough that, as shown by Young and Maas (47), the correction due to the effective displacement of the tube center may be neglected.

The static tube is mounted higher on the stem in order to avoid the region of high total pressure gradient near the wall. Since pressure taps set in the channel surface are impractical here, similar free stream static tubes were incorporated into all of the boundary layer probes used in this study.

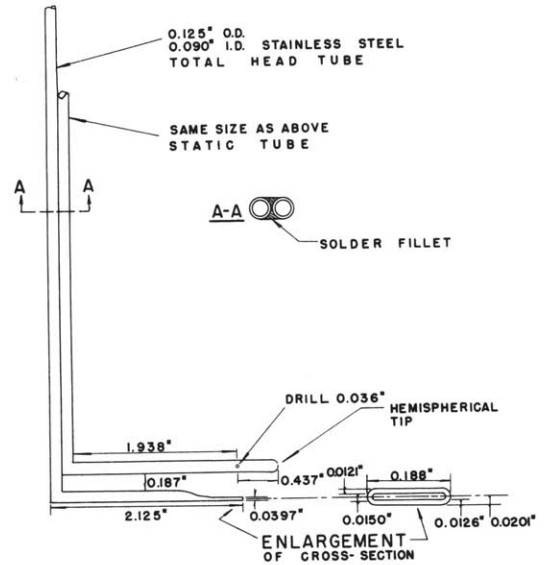
Before final assembly of the instrument, it was first established that there was no mutual interference of the static and total head tubes due to their spacing. Because its dimensions were set arbitrarily, the instrument was calibrated in free stream flow against a standard design Prandtl tube; the agreement of the measured velocities was satisfactory and was still better than $\pm 5\%$ for water velocities as low as 1 fps.

2. Surface Pitot Tubes

As mentioned earlier, round, square-faced, total head tubes were used to measure boundary shear stress. For the smooth channel tests, the various models used had identical total head tubes (Figures 4 and A-7) machined from 0.25" x 0.18" stainless tubing. This diameter was selected to place the measured data within the limits of Preston's calibration. The length of the impact tube is six diameters; the geometry was set in an effort to minimize stem effects on the velocity distribution at the tube

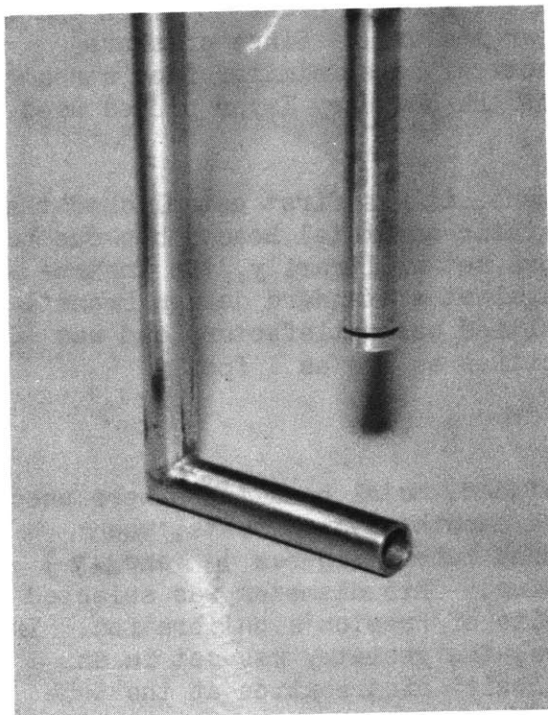


(a.)

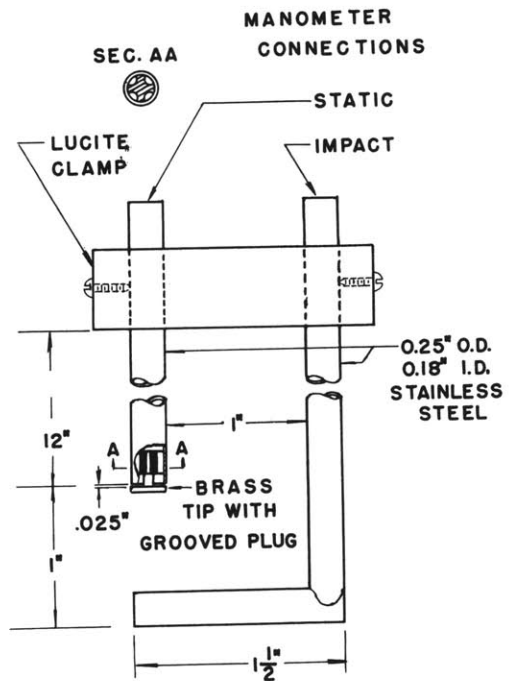


(b.)

Figure A-6. Pitot Tube for Measuring Wall Velocities.

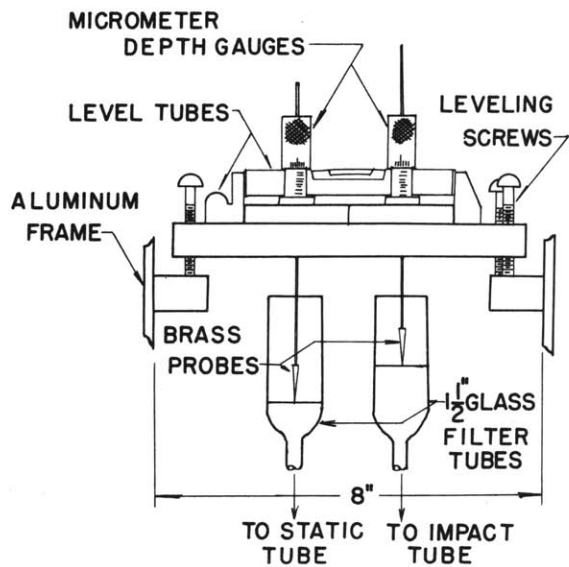


(a.)

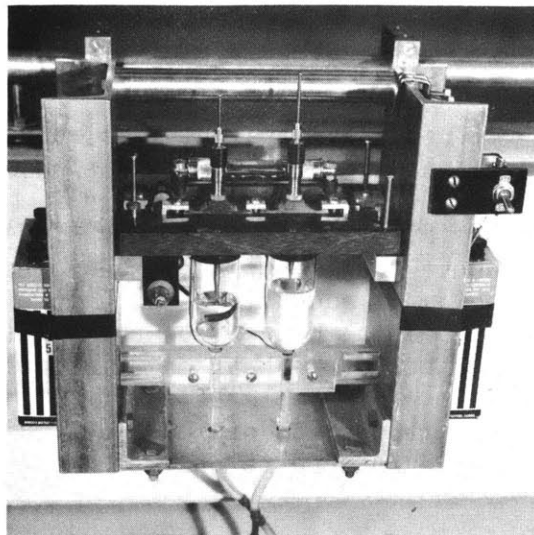


(b.)

Figure A-7. Model II Surface Pitot Tube.

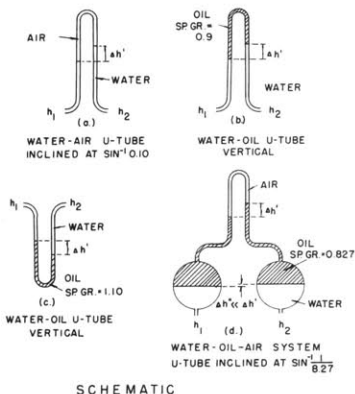


(a.)



(b.)

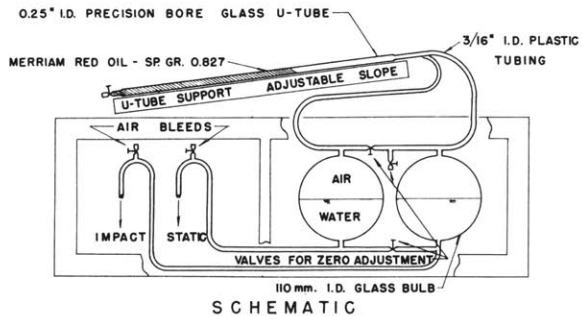
Figure A-8. Micromanometer.



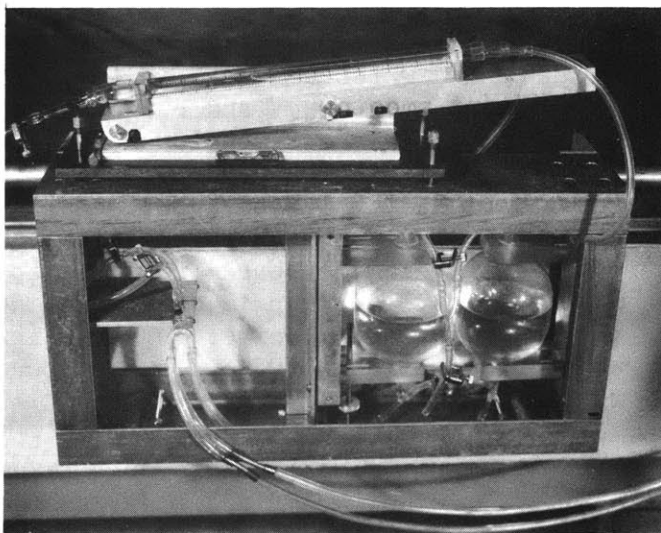
SCHEMATIC

Figure A-9. Development of the Inclined Manometer.

All Manometers are designed such that $\Delta h' = 10(h_2 - h_1) = 10\Delta h$.



(a.)



(b.)

Figure A-10. Inclined Manometer.

face, yet retain a straight tube sufficiently short to be placed tangent to the sides in the channel curve.

The static tube on all models was located, as discussed previously, above the impact tube, away from the boundary. In the course of developing an adequate design, however, several modifications were tried and used in the various runs, before the final model was developed. The boundary shear data, presented in the various figures, was taken, as noted in Table II, with the different instruments. After the introduction of the Model III surface Pitot tube, however, the earlier runs were re-checked in order to assure consistency of the data.

As reported earlier (32) the first surface Pitot tube, with the static ports set in 2 rows on the vertical stem at $39 \frac{1}{4} \phi$ about the center line, proved to have great directional sensitivity. In the $\frac{1}{4}$ " single curve run, therefore, a Prandtl tube mounted in tandem with the total head tube was used to give the static reading. This instrument combination was designated the Model I Surface Pitot Tube.

Because the above method entailed rather laborious experimental techniques, a second instrument, designated Model II, was developed, and used in the 3" and 6" single curve runs. The static opening is in the form of a ringed slot on the end of a separate stem (Figure A-7). The intention in the design of Model II was to provide a method of measuring static pressure which would be insensitive to orientation (for flows perpendicular to the vertical stems). However, flow around the circular static tube results in a large positive error in the measured ΔH . The calibration to give the true ($h_t - h_o$) which is reported by Noutsopoulos (34) is not reproduced here, since this design was ultimately discarded. The calibration added several steps to the computations, making the reduction of data unnecessarily long; in addition, it was found that the performance of the tube was unreliable, giving generally higher values of τ_o than the other models.

A satisfactory design was achieved in the Model III instrument (Figure 4) which was used in the 5" single curve run, and in all the subsequent smooth and rough surface tests. The static arm is proportional to the dimensions of a standard Prandtl tube, using the $\frac{1}{8}$ " stem tube as the reference diameter. The ovoid stem shape attenuates the effect of the larger tube, and it was found that the stem has negligible influence in the static readings. The static holes are nominally 3 diameters back from the tip, but a trial and error process was necessary in order to determine the best exact location. Setting the holes in tandem pairs, as shown in Figure 4, gave a static head error of less than $0.02 \frac{u^2}{2g}$, yet permitted a reasonably short response time.

The tests of orientation effects on the instrument, Model III, showed that at yaw angles of up to 20° , there is a decrease of up to $0.06(h_t - h_s)$ in both the static and impact heads, but that $(h_t - h_s)$ remained essentially constant. In the test channel curve, examination of dye traces revealed that strong flow angularity is confined to a thin zone near the channel bottom, and that at the height of the static probe, the flow is essentially parallel to the curve centerline. Tests to determine the angular sensitivity of the total head tube showed that the error in measured shear stress varies essentially as $(1 - \cos \alpha)$; at $\alpha = 20^\circ$, the error is 6%, and at $\alpha = 15^\circ$, the error is about 3%.

In order to measure boundary shear stress on a rough surface, a cylindrical sleeve assembly was made to fit snugly over the impact tube, and calibrated on the Model III; the modified instrument is designated the Model III-A. The aluminum sleeve, which was machined from $7/16'' \times 3/8''$ tubing, is shown with the teflon bushing in Figure 4.b. The reasons for making the impact tube so large were twofold: (1), at the low channel slope, the velocities near the rough boundary were slight, and the larger diameter was selected in order to sample more of the boundary layer with a consequent increase in ΔH ; (2) since the roughness particles were approximately 0.1" in height, the effects of poor tube placement would be reduced for a tube diameter appreciably larger than the roughness height.

3. Manometers

The low velocities encountered in this investigation led to the design of two manometers sensitive in the range $0.01' < \Delta H < 0.1'$.

A micromanometer, shown in Figure A-8, was used as the standard instrument, throughout the study. Two micrometer depth gauges and a precision level are mounted on an adjustable plate. Pointed brass probes extend down into 1 1/2" diameter filter funnels which serve as open piezometer columns. The difference in water levels is read on the two gauges to the nearest 0.001". The instrument is mounted on the instrument rails of the flume and can be easily moved. Originally the instrument was fitted with a neon lamp circuit designed to close when either probe touched the water surface. The electrical system was not used, however, since it was found that, with proper lighting, visual observation gave faster and more consistent results.

This instrument, although highly accurate, has a slow response time. At least 3 minutes are necessary between readings, although it has been found that to obtain a reproduceable average in a dynamic test may take as long as 15 minutes. This is due to the large diameter wells which were necessary in order to eliminate capillary effects*. Attempts to improve the response of the instrument by the use of smaller wells resulted in unpredictable errors.

*The use of silicone non-wetting agents, such as Desicote (Beckman Instruments, Inc.), is not recommended by the manufacturers for high precision water

As a means of speeding up the laboratory procedures, the inclined manometer shown in Figure A-10 was developed. The instrument which used three fluids, evolved from a series of attempts to use water as the meter fluid, and various water-oil combinations.

In using water as the fluid in two inclined piezometers (Figure A-9a) it was found impossible to keep the tubes clean enough to prevent differential wetting of the glass. The manometer could not be calibrated, and errors of ± 0.01 were common.

Manometers using an immiscible fluid of specific gravity close to that of water also failed. Mixtures of Tetrachloroethylene and Xylene of Sp. Gr. 0.90 and 1.10 were each tried in contact with water. with the U-tube positioned according to the respective density differences of the fluids (Figure A-9 b and c). Eagle and Wilson (7.) working with similar manometers also found them unsuitable for measuring small head differences.

It was first assumed that errors were due to surface tension effects at the liquid interfaces, and that by enlarging the tubes the system could be made stable. As shown in Figure A-9 d, the interfaces were set at the enlarged bulbs with the lighter oil floating in the water, and the air space above the oil was sealed. For bulbs of sufficiently large diameter, the interface levels remain essentially constant, and $(h_1 - h_2)$ is read directly from the upper oil surfaces. Calibration of this manometer appeared at first to be satisfactory. After a week's time, however, scum began to form at the interfaces, and the calibration was again uncertain.

At head differentials of the order of $0.01'$, all the manometer schemes shown in Figure A-9 gave excessive errors .

For the final design (Figure A-D) the oil and water are separated by air spaces. The instrument, in effect, combines the accuracy of large piezometer wells with the quick response of an air-oil manometer. The system uses a commercial gauge fluid (Meriam Red Oil D-2673 Sp. Gr. 0.827) in a U-tube inclined at an angle of $\sin^{-1}(1/8.27)$ to give a direct reading scale factor of $10x$. Calibration of the instrument against the micromanometer has shown a consistent accuracy of better than $\pm 2\%$ over the range $0.02' < \Delta H < 0.08'$. With the $10x$ scale factor, Δh is read directly to the nearest $0.001'$, and estimated to $0.0001'$. After every 6-8 weeks of use, the gauge oil is changed and the calibration checked. The instrument has been in continuous use for a year, and has proven to be completely dependable. The response time between readings is not over 30 seconds,

manometers. It is claimed that an un-wetted surface inhibits free motion of the meniscus. Therefore, all the instrument glassware used in this study was not treated, but was washed frequently to assure uniform wetting.

although, as with any instrument, a somewhat longer period is necessary to average a fluctuating condition.

The manometer is mounted on the flume rails in a rigid aluminum frame. There is provision for independent leveling of the U-tube support. Shunt tubes above and below the bulbs permit the system to be checked for zero reading without interrupting a test. Because the air spaces make the instrument extremely sensitive to temperature gradients, the two bulbs are enclosed in fibre board walls and the system is kept sheltered from drafts.

C. Review of Techniques for the Determination of Boundary Shear Stress

In selecting the instrumentation for this study, various methods of determining local boundary drag were investigated. In the following discussion a survey of these techniques is given; each of the methods listed is reviewed within the framework of the requirement of this study.

1. Velocity Profile Methods

A number of methods based upon the flow velocity distribution are available for the indirect determination of boundary shear.

a. Shear Computed from a known or assumed Velocity Distribution:

There are several methods by which the boundary shear stress can be computed from the distribution of velocities within the boundary layer. Since the surface Pitot tube technique used in this investigation lies within this category, an extensive discussion on the principles underlying the various related methods is given in Appendix D.

b. Momentum Analysis: The momentum principle could be applied to arbitrarily selected control volumes in the flow. For non-uniform flow in the straight channel or for curvilinear flow in the bend, the size of these control volumes become small as a local, and not an average, shear is desired. This method depends upon the accuracy of the velocity profiles over the depths of the control volumes selected, requires velocity data close to the boundaries for an accurate determination of the momentum flux, and also depends upon the accuracy of the bottom slope and surface profile measurements as well as an assumed pressure distribution. This approach is obviously too cumbersome and subject to error.

A simplification of this approach has been suggested by Leighly (25)

for the determination of the boundary shear distribution for uniform flow in straight open channels. Considered is the equilibrium of forces on a filament of the flow bounded by a segment of the solid boundary perimeter and by surfaces constructed perpendicular to isovels of the measured longitudinal velocities. This method is not applicable to curved flow because, in the presence of secondary currents and asymmetric velocity distributions, equilibrium along the internal surfaces can no longer be assumed.

c. Theoretical Methods: The pattern of curved flow also eliminates the various analogic methods proposed by Olsen and Florey (35) on the basis of their mathematical model of channel flow. This latter approach has been applied only for rectilinear flow; furthermore, the assumptions leading to the reduction of the problem to a solution of Poisson's equation restrict the results to laminar streams. For the general turbulent channels, the method provides an approximate solution only.

2. Direct Shear Force Measurement

This method consists of determining the local skin friction on a plane surface by measuring the shear force exerted on a small movable element located in and flush with the plane surface. This approach, first used by Kempf in 1929 to obtain skin friction values at high Reynolds numbers on the bottom of a barge, has been used for shear measurements on smooth surfaces in air by Dhawan (6) for both laminar and turbulent boundary layers, and by Hakkinen (17) who extended test data in to the supersonic range. The displacement of the small floating element used is caused by shear stress. In these latter two investigations, linear variable differential transformers served as the transducers to convert a physical displacement into an electrical signal; strain gages could also

be used for this. Such floating element gages, on a larger scale, have been used to measure transient shear stresses under waves (20).

The major objection to this approach is that data can be obtained readily at only one point. In order to map shear distributions over an area, either a large number of such instruments would have to be mounted permanently in recesses in the channel lining, or one instrument assembly would have to be moved from one location to another, with attendant gage alignment problems at each location. Either approach is impractical.

A serious additional limitation inherent in this approach is that such floating element devices are unsuitable where pressure gradients in the flow give rise to forces on the moving element which may easily be of the same order of magnitude as the shear stresses which are to be measured.

3. Heat Transfer Measurement

The heat transfer approach makes use of the analogy between the transport of momentum and the transfer of heat near a solid boundary. The instrument consists of a heated element which is flush with the surface in which the shear is to be measured, and thermally insulated from it; the heat flow to this element is measured, as are the temperatures of the element itself and of the flowing stream. This technique has been used for measurements in air. Liepmann and Skinner (29) report a method using a simple hot-wire embedded in the surface to determine skin friction coefficients for low speed air flows; this is an extension of the hot-spot technique reported by Ludwig (30).

One difficulty of this technique is providing a known shear stress for calibration purposes, although Liepmann and Skinner found a single calibration to hold true for both laminar and turbulent boundary layers.

As with the displacement gauges, lack of mobility precludes the use of heat transfer methods.

D. The Measurement of Boundary Shear
Stress with Pitot Tubes

1. Smooth Boundary Applications

a. General: The use of Pitot tubes for shear stress measurements on smooth surfaces is well known in aeronautical research. The various techniques are all based on the common principle that, within a limited portion of the boundary layer, the velocity distribution past a smooth surface may be expressed as,

$$\frac{u}{u_*} = \Phi_1\left(\frac{u_* y}{\nu}\right) . \quad (1)$$

Since $u = \sqrt{(p_t - p_o)2/\rho}$, the dynamic pressure determined with a Pitot-static tube is a function dependent only on ρ, ν, y , and τ_o , and by dimensional analysis, Equation (1) may be regrouped in the form,

$$\frac{(p_t - p_o)y^2}{\rho\nu^2} = \Phi_2\left(\frac{\tau_o y^2}{\rho\nu^2}\right) , \quad (2)$$

where y is the normal distance from the wall to the geometric center of a small Pitot tube. Thus for a known velocity distribution, the boundary shear stress can be determined from point velocity measurements. This method has been applied by Enger (10) in a recent investigation in which the shear was measured over the periphery of a straight trapezoidal channel.

It is known that, for a Pitot tube of relatively large size, a correction, y^1 , must be applied to offset the displacement of the effective center of the Pitot tube from the geometric center (47). However, if a Pitot tube of some specified geometry - or one of a set of geometrically similar Pitot tubes - is placed on the surface, then for that geometry, $y/d = \text{constant}$, where d is the height of the probe. Thus, by substitution, Equation (2) becomes,

$$\frac{(p_t - p_o)d^2}{\rho\nu^2} = \Phi_3\left(\frac{\tau_o d^2}{\rho\nu^2}\right) . \quad (3)$$

Here, the correction of Young and Maas (47) for the center displacement is unnecessary, since as shown by Granville (16),

$$\frac{y^1}{y} = f\left(\frac{y}{d}, \frac{u_* y}{\nu}\right) , \quad (4)$$

and hence the correction will be absorbed in the structure of Equation (3), which is obtained experimentally.

Equation (3) forms the basis of all techniques for measuring boundary shear stress with Pitot tubes on smooth surfaces. If Equation (1) can be given a concise expression over some range of $R_x = u_* y / \nu$, then an empirical calibration, Equation (3), can be obtained for a set of similar Pitot tubes. However, a change in Pitot tube geometry would require a new calibration since the center displacement effect (Equation [4]) varies with the shape of the Pitot tube.

In turbulent incompressible flow past a smooth boundary two flow regimes exist within the region loosely defined as the inner boundary layer. Immediately adjacent to the wall, in the laminar sublayer, the velocity profile may be considered linear and Equation (1) becomes,

$$\frac{u}{u_*} = \frac{u_* y}{\nu}, \quad (5)$$

for the range $0 \leq u_* y / \nu \leq 11$. (cf., Schlichting (38) Chap. XX) Farther out from the wall the flow becomes turbulent and the inner velocity layer may be expressed

$$\frac{u}{u_*} = A \log \frac{u_* y}{\nu} + B,$$

or, alternatively,

$$\frac{u}{u_*} = C \left(\frac{u_* y}{\nu} \right)^{1/n} \quad (6)$$

For $11 < R_x < 500-700$, the exponent $1/n = 1/7$ gives good agreement with the data of most investigators. Due to the difference between flow past flat plates and in round pipes, there has been some disagreement in the value of the coefficient, but it seems clear that in general $C \approx 8.7$.

b. Surface Pitot Tubes in the Laminar Flow.

Small Pitot tubes of various designs have been reported with calibration data (1)(11)(11), for the determination of shear stress within the laminar sublayer. These instruments are designed so that the height of the probe, d , does not exceed the thickness of the laminar regime, δ' . Thus, from Equation (5), the calibration corresponding to Equation (3), has the form,

$$\frac{\tau_0 d^2}{\rho \nu^2} = K \left[\frac{(p_t - p_0) d^2}{\rho \nu^2} \right]^{1/2}, \quad (7)$$

K being a factor dependent on the geometry of the probe. Equation (7) is valid only for incompressible flow; Abarbanel et. al. (1) have reported calibration data for compressible flows as well as for the case of the probe height exceeding the thickness of the laminar sublayer.

This type of instrument has received wide and successful application in aeronautical research. For the test conditions of the present investigation, however, the laminar sublayer never attains a thickness greater than a few hundredths of an inch. To illustrate, assuming a representative $\tau_0 = \gamma R S_e = 0.01$ psf in water at 70°F, the maximum Pitot tube size becomes

$$d \leq \delta' \approx \frac{11\gamma}{\sqrt{\tau_0/\rho}} \approx 0.018'' \quad (8)$$

Thus, practical considerations alone precluded the use of Pitot tubes in the laminar sublayer. The small tube dimensions would lead to exceedingly slow instrumental response. Furthermore, the channel, while being essentially a hydraulically smooth surface, does contain irregularities of this order of magnitude, and correct placement of the instrument would be uncertain.

c. Surface Pitot Tubes in the Turbulent Boundary Layer.

A technique developed by Preston (37) is based on the use of round surface Pitot tubes for the measurement of turbulent boundary shear stress on smooth surfaces. He reasoned that if a Pitot tube is designed with $d \gg \delta'$, then the effect of the laminar sublayer may be considered negligible, and Equation (1) should assume the form of a logarithmic or power function, resulting in a corresponding form of Equation (3).

Preston's calibration experiments were carried out for air flows in a smooth pipe, with the pipe pressure drop in a region of uniform flow being used to determine the wall shear. In order to avoid the problem of variation in y/d , the experiments were conducted with a set of four geometrically similar Pitot tubes. Fabricated from round tubing, the tubes were machined square-faced to a constant ratio of inner to outer diameters. The circular shape was chosen to simplify positioning of the tubes on the boundary, and because, in the machining operations, it permits more precise control of the tube geometry than is possible with other shapes.

For the turbulent boundary layer, Preston obtained the following empirical relationship, with its limits of applicability:

$$\log \frac{\tau_0 d^2}{4 \rho v^2} = -1.396 + 7/8 \log \frac{(p_t - p_o) d^2}{4 \rho v^2}, \quad (9)$$

$$4.5 < \log \frac{(p_t - p_o) d^2}{4 \rho v^2} < 6.5.$$

The experimental limits of this equation correspond, in effect, to the range over which Equation (6) is valid. At lower values of $\log \frac{(p_t - p_o)d^2}{4 \rho v^2}$, the laminar sublayer becomes significant, while above the given range, the region of similarity postulated in Equation (6) no longer exists.

As Preston points out, the coefficient, $7/8$, in Equation (9) implies the existence of a $1/7$ - power velocity law. Using a small, flattened Pitot tube in the free stream, he determined the velocity distribution to be

$$\frac{u}{u_*} = 8.61 \left(\frac{u_* y}{\nu} \right)^{1/7} \quad (10)$$

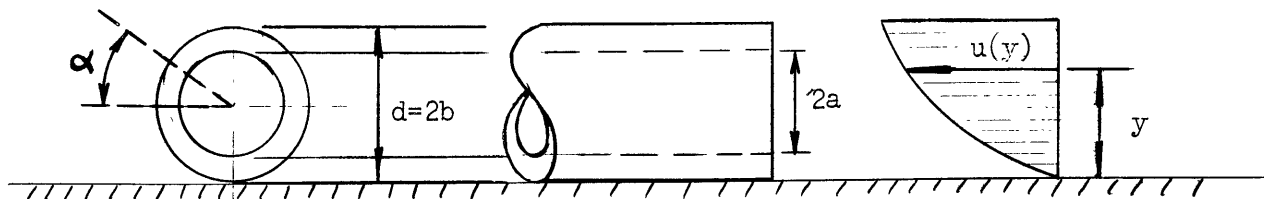
By squaring this equation, multiplying both sides by $u_* y / \nu$, and making appropriate substitutions, the relation analogous to Equation (2) becomes

$$\log \frac{\tau_o y^2}{\rho v^2} = -1.372 + 7/8 \log \frac{(P_t - P_o) y^2}{\rho v^2} \quad (11)$$

By the structural similarity between Equations (9) and (11), which differ only by a constant due to the displacement effect noted above, Preston thus showed that the form of the calibration equation can be predicted from a known velocity distribution.

Preston, and later, Hsu (18) extended this work to flat surfaces tested in larger wind tunnels under conditions of zero and adverse pressure gradients, and further substantiated Equation(9). On the basis of further surface tube and velocity profile data, Preston concluded that the region of similarity (Equation(6)) over which the calibration holds, ranges from $1/5$ to $1/20$ the boundary layer thickness, for respective conditions close to or remote from separation.

In addition to verifying Preston's equation, Hsu showed, both analytically and experimentally, that the ratio of inner to outer tube diameters has a negligible effect on the measured results. Starting with Preston's velocity distribution, Equation (10), Hsu derived the turbulent shear relation for round surface Pitot tubes as follows: consider a round surface Pitot tube in a turbulent boundary layer, as shown in the definition sketch.



A round surface Pitot tube in boundary layer flow.

Neglecting both the influence of the laminar sublayer, and any disturbance caused by the presence of the tube, the dynamic pressure recorded at the tube face may be expressed as

$$(p_t - p_o) = \frac{1/2 \rho \int_{\sigma} u^2 d\sigma}{\pi a^2} .$$

Substituting

$$u = 8.61 u_* \left(\frac{u_* y}{\nu}\right)^{1/7} \equiv C u_* \left(\frac{u_* y}{\nu}\right)^{1/7}$$

and

$$d\sigma = 2 \sqrt{a^2 - (b-y)^2} dy,$$

this becomes

$$(p_t - p_o) = \frac{\rho}{\pi a^2} \int_{b-a}^{b+a} C^2 u_*^2 \left(\frac{u_* y}{\nu}\right)^{2/7} \sqrt{a^2 - (b-y)^2} dy.$$

Noting that $y - b = a \sin \alpha$, the expression simplifies to

$$\Delta p = \frac{\rho}{\pi} C^2 u_*^2 \left(\frac{u_*}{\nu}\right)^{2/7} b^{2/7} I(t), \quad (12)$$

where t is the tube thickness ratio, a/b , and

$$I(t) \equiv \int_{-\pi/2}^{\pi/2} (1 + t \sin \alpha)^{2/7} \cos^2 \alpha d\alpha.$$

The integral, $I(t)$, must be evaluated numerically for desired values of t .

Equation (12) may be rearranged into the form of Equation (9) as

$$\log \frac{\tau_o d^2}{4\rho\nu^2} = \log C_1 + 7/8 \log \frac{(p_t - p_o)d^2}{4\rho\nu^2}, \quad (13)$$

$$C_1 \equiv \left[\frac{\pi}{C^2 I(t)} \right]^{7/8} .$$

Hsu's values of C_1 for $t = 0$ and $t = 1$, together with the corresponding values determined by other investigators are listed in Table A-I. In spite of the predicted higher values of C_1 , his experimental evidence led Hsu

Table A-I.			
Summary of the results of previous investigations on the calibration of round surface Pitot tubes in turbulent boundary layers.			
Investigator	$\log C_1$	C_1	Method of determining τ_0
Preston (37)	-1.396	0.0403	Pipe Pressure drop
Hsu (18): Experimental:	-1.396	0.0403	Momentum thickness measurements on a flat surface
Predicted: $t = 0$:	-1.373	0.0424	
$t = 1$:	-1.360	0.0437	
Bradshaw and Gregory (5):	-1.350	0.0447	Stanton tubes on a flat surface
Smith and Walker (40)	-1.366	0.0431	Floating element dynamometer set into a flat surface

to conclude that Preston's that Preston's equation is adequate, and that the internal geometry of round surface Pitot tubes is not an important factor.

In more recent years, a controversy has arisen as to the validity of Equation (9), which was determined in fully developed pipe flow, for boundary layer flows past flat plates. While the various investigators have established the exponent as $7/8$, there has been disagreement, as shown in Table A-I, over the coefficient, C_1 . In a later study Bradshaw and Gee (4) using pitot tubes in unseparated zones of a deflected airfoil flap, showed that longitudinal pressure gradients may effect the calibration by as much as 10 %.

d. Experimental Applications

In order to use the surface Pitot tube in the test channel it was necessary to prove that one calibration expression would hold throughout all parts of the straight and curving flow. Since direct calibration was not possible in this case, the velocity distribution near the boundary was determined, permitting calculation of the calibration equation.

Figure A-11 shows the results of nine vertical velocity profiles, six of which were taken in the test channel at the positions shown in the inset sketch. The measurements were taken at the conditions of the 5" Run (cf. Table II) with the Pitot tube shown in Figure A-6. The traverses were started with the Pitot tube resting on the boundary; each profile consists of 11 readings taken at successive 1mm. intervals. For all of the points the shear velocity, u_* , was computed from the boundary shear stress as determined by the surface Pitot tube (Model III, Figure 4) readings, with Equation (9).

Although the six velocity profiles taken in the test channel represent one condition of flow only, their positions were selected to include great variation in shear stress as well as local velocity. The local shear stress ranged from 0.010 to 0.019 psf., while the velocity at 1 cm. from the boundary varied from 1.46 to 2.00 fps. Since this variation is of the same order as the variation among all the test conditions, little would have been gained by repeating the profiles at another flow condition.

The additional points on the plot represent three profiles taken at a higher velocity in a glass bottomed flume. In this case it was possible to compute the friction factor from the Reynolds number, and hence the shear stress, providing a check against the Pitot tube results. The two methods of obtaining τ_0 gave results which were within 5% of each other, the higher value being that given by the Pitot tube.

The solid curve drawn through the experimental points is the velocity distribution found by Preston, Equation (10). The agreement between this expression and the measured velocity distributions is sufficiently close, that Equation (10) was assumed to be an adequate representation of the inner velocity distribution in smooth walled flumes. It is of interest to note that for the Pitot tubes used in this study, Equation (13) gives a value of $C_1 = 0.0429$. However, since Hsu's direct calibration experiments give results close to Preston's, Equation (9) was used as the calibration law for round Pitot tubes on smooth surfaces. Had Equation (9) been seriously in error, the experimental points in Figure A-11 would have been displaced from Equation (10).

It should be noted that the top of the 1/4" diameter total head probe was always well within the established region of similarity of Equation (10); for $y = 0.25$ ", none of the recorded values of u_{xy}/v exceeded 250. No specific effort was directed towards establishing the importance of variations in longitudinal pressure gradient; for the range of local water surface slopes encountered in these tests, however, this apparently is a minor effect.

On the basis of these tests it is concluded that in free surface flows, both straight and curving, Pitot Tubes do provide a reasonably accurate means of determining the absolute, as well as the relative boundary shear stress.

From Equation (9) it is clear, that for a given fluid, the size of a Pitot tube must be selected to bring the term $\log(\Delta p d^2 / 4 \rho v^2)$ within the proper range. If, for a series of experiments, it is possible to use Pitot tubes of one diameter in a single fluid, then Equation (9) may be written in a more convenient dimensional form,

$$\tau_o = 0.0403 \left(\frac{4 \rho v^2}{d^2} \right)^{1/8} (\Delta p)^{7/8} \quad (14)$$

In the present investigation the fluid is water, d was set at 0.25", and Δp was measured as manometer head, in feet of water. These restrictions reduce Equation (14) to:

$$\tau_o = 2.64 (\rho v^{1/4}) (\Delta H)^{7/8}, \quad (15)$$

which is plotted in Figure A-12 for various water temperatures.

2. Rough Boundary Applications

In the course of this investigation, a method was needed for rapidly measuring the boundary shear on rough surfaces. Because the surface Pitot tube technique has proven to be adequate, easy to use, and inexpensive, an attempt was made to determine the calibration for hydrodynamically rough surfaces. To simplify the problem, a single Pitot tube was used on a surface of uniform roughness. This technique was applied to a specific situation only; direct extrapolation of the technique to other types or degrees of roughness is therefore not warranted at present.

For flow past a hydrodynamically rough surface the velocity distribution is independent of the Reynolds number $u_* y / \nu$, and, may be expressed,

$$\frac{u}{u_*} = \Phi_a \left(\frac{y}{k} \right), \quad (16)$$

where k is the height of the roughness protrusions. (cf. Schlichting Ch. XX). Preston (37) suggests it should be possible, by a method analogous to the development of Equation (3) to determine the corresponding calibration function for a Pitot tube, on a rough surface:

$$\frac{\Delta p}{\tau_o} = \Phi_b \left(\frac{d}{k} \right). \quad (17)$$

The major difficulty is, that the Pitot tube must always be placed in the same position with respect to the rough boundary, and for this reason alone, the technique does not lend itself to general application.

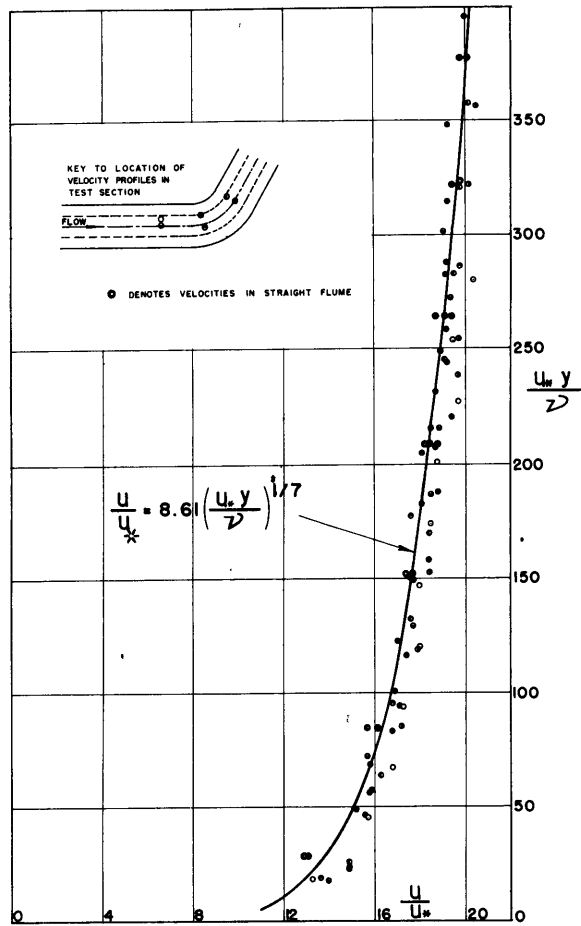


Figure A-11. Velocity Distribution Past the Smooth Test Surface.

Equation 15: $\tau_w = \phi(T) \cdot \Delta H^{7/8}$

Restrictions:

1. For 0.25" diameter Pitot tube in water.
2. $0.0012 < \tau < 0.041$ PSF

Definition:

$$\phi = 2.64 \rho \nu^{1/4}$$

For water

T - °F	ϕ - LB/FT ^{3/4}
60	0.302
70	0.291
80	0.281
90	0.273
100	0.265

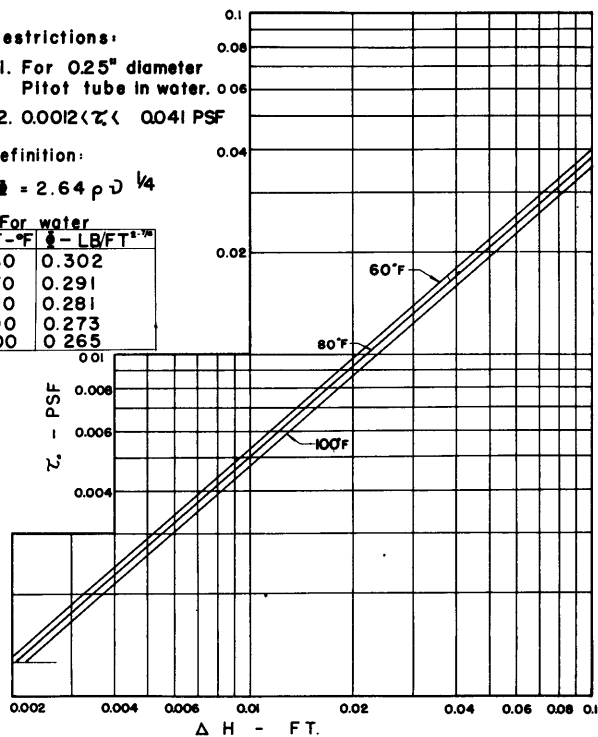


Figure A-12. The Simplified Preston Calibration Curve.

- PROFILE NO. 1
- NO. 2
- NO. 3
- NO. 4
- NO. 5

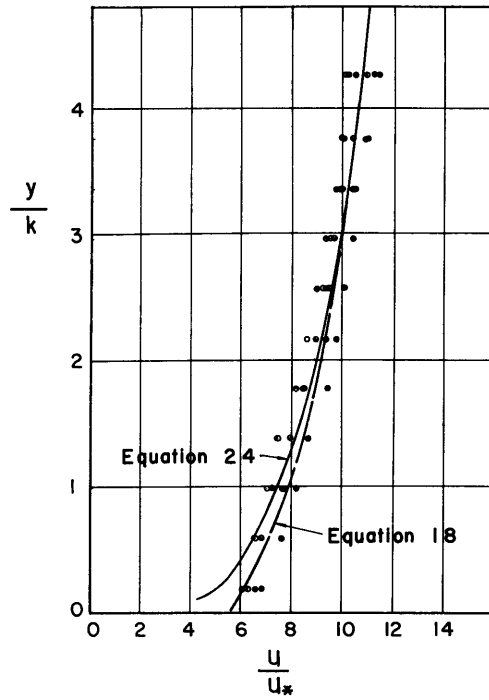


Figure A-13. Velocity Distribution Past the Rough Test Surface.

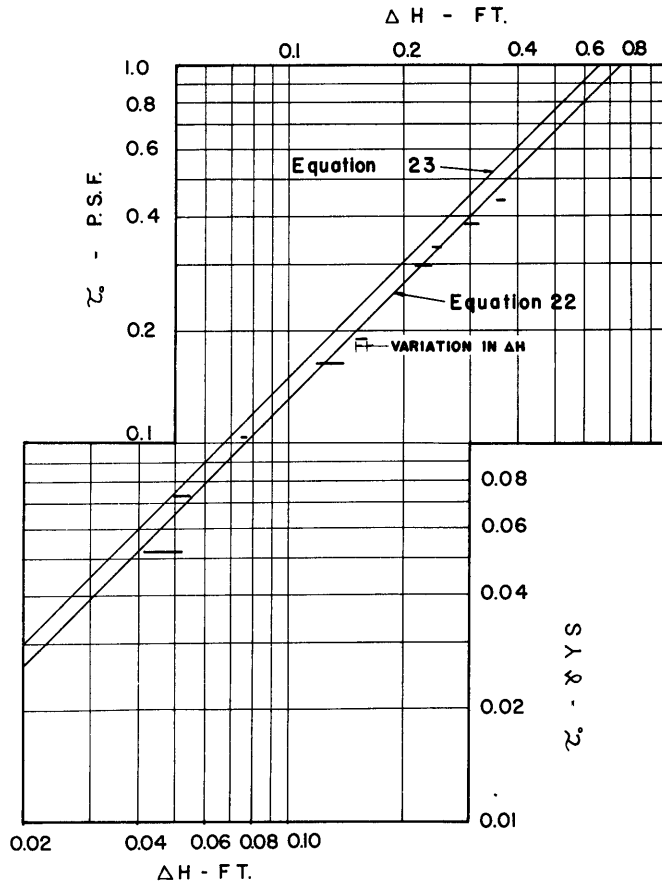


Figure A-14. Rough Surface Pitot Tube Calibration.

In the following discussion, a calibration of a round surface Pitot tube is presented. On the basis of measured velocity profiles, a velocity power law is defined which leads, following Hsu's derivation, to a predicted calibration equation. An empirical calibration was determined for one Pitot tube tested on a single surface of uniform roughness, for a very limited range of y_0/k under conditions of fully rough flow. The agreement between the predicted and empirical equations is only fair, but because the equations differ only by a constant coefficient, the method could be used for measuring τ_0/τ_0 in the test channel.

Within these restrictions, therefore, the following derivation and calibration are presented:

The calibration and velocity measurements were performed in a straight, smooth walled, tilting flume, in which had been laid 20 feet of the rough surface used in the curved channel study. This length allowed full boundary layer development, with a 6 foot test reach in the downstream portion. The boundary shear stress was computed from $\tau_0 = \gamma y_0 S_e$, where y_0 was defined as the depth from the surface to the bottom of the roughness particles. The error in assuming y_0 as the effective hydraulic radius was small since, with smooth sides and shallow depths, the flows were essentially 2 dimensional.

For fully rough flow, the velocity distribution, Equation (16), is generally stated as a logarithmic law. Nikuradse (33) also suggests that, over a limited range of y/k , a power law will give an adequate approximation of Equation (16), but that the exponent, and hence the coefficient, will vary with the geometric parameter ro/k . Therefore, the power law,

$$\frac{u}{u_*} = C \left(\frac{y}{k}\right)^{1/n}, \quad (17)$$

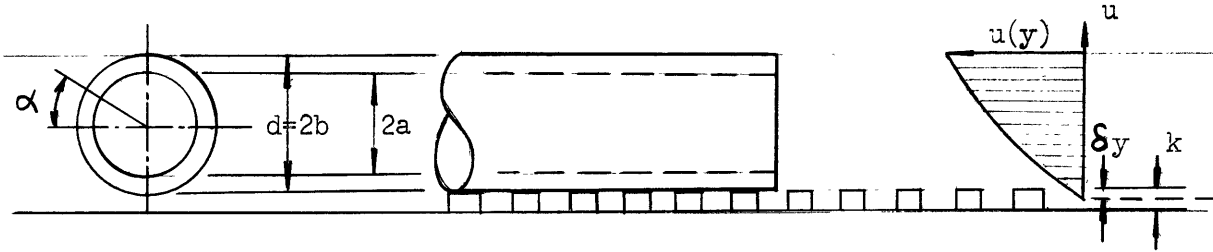
was assumed valid, for the conditions of the test series.

Figure A-13 shows the results of five velocity profiles plotted as y/k vs. u/u_* , in which the point $y = 0$ is defined as the top of the roughness particles and k is the absolute roughness height. The velocity measurements were taken in exactly the same way as the smooth surface profiles (Figure A-11), starting with the Pitot tube resting on the top of the roughness particles. The trend of the data shows that the coordinate system should be displaced, by a constant amount δ , bringing the origin below the top of the rough surface. A process of curve fitting, first to determine the exponent, and then the origin and coefficient led to the equation,

$$\frac{u}{u_*} = 7.25 \left(\frac{y + \delta y}{k} \right)^{1/4}, \quad (18)$$

$$\delta y = 0.0027 \text{ ft.}$$

In order to derive the turbulent shear relation, Equation (17), the displacement constant, δy , must now be considered in the integration. A round surface Pitot tube, such as that shown in the definition sketch below, will record a pressure,



$$p_t - p_o = \frac{1/2 \rho \int_{b-a+\delta y}^{b+a+\delta y} \left[u_* C \left(\frac{y}{k} \right)^{1/n} \right]^2 \cdot 2 \sqrt{a^2 - (y-b-\delta y)^2} dy}{\pi a^2} \quad (19)$$

By the steps outlined earlier, and with $u_*^2 = \tau_o / \rho$ this simplifies to

$$p_t - p_o = \frac{\rho u_*^2 C^2}{2^{2/n} \pi} \left(\frac{d}{k} \right)^{2/n} I(t), \quad (20)$$

$$\text{where } I(t) = \int_{-\pi/2}^{\pi/2} \left(1 + \frac{\delta y}{b} + t \sin \alpha \right)^{2/n} \cos^2 \alpha d\alpha$$

$$\text{and } (y - b - \delta y) = a \sin \alpha.$$

Then, by rearranging Equation (20), the dimensionless calibration may be obtained as

$$\frac{\tau_o}{(p_t - p_o)} = \left(\frac{d}{k} \right)^{-2/n} \left[\frac{\pi 2^{2/n}}{C^2 I(t)} \right] \quad (21)$$

A Pitot tube of 0.432" diameter was calibrated with a manometer in the tilting flume. For each shear velocity condition, readings were taken at six positions in the flume to give the range of data shown in Figure A-14. From the structure of Equations (17) or (20), it is clear that for fully rough flow, $\tau_o \sim (p_t - p_o)$. In evaluating the calibration curve, therefore, a slope of unity was assumed, and the mean constant determined. The resulting calibration equation is,

$$\tau_o = .0208 \gamma \Delta H = 1.30 \Delta H \quad (22)$$

where ΔH is the manometer reading in feet of water.

For the conditions of the calibration and the subsequent channel tests, the following experimental values may be substituted into Equation (21): $d = 2b = 0.432"$, $k = 0.1"$, $\delta y = 0.0027'$, $C = 7.25$, and the water density, $\gamma = 62.3 \text{ lbs/ft}^3$. Then, assuming $t = 0$, the predicted calibration equation becomes,

$$\tau_o = .0242 \gamma \Delta H = 1.51 \Delta H \quad (23a)$$

Because of the extra steps involved in determining the displacement constant, δy , a calibration equation was also computed for the best fit to the data in Figure A-13 on the basis of the one fourth power law assuming $\delta y = 0$. This approximate velocity distribution,

$$\frac{u}{u_*} = 7.5 \left(\frac{y}{k} \right)^{1/4}, \quad (24)$$

is also plotted in Figure A-13. It gives the calibration:

$$\tau_o = 1.50 \Delta H \quad (23b)$$

It may be concluded, therefore, that the Pitot calibration equation is not sensitive to small variations in the velocity distribution.

The difference between the predicted and the empirical calibration constants must be attributed to the fact that the theory neglects the internal circulation induced within the tube by the total pressure gradient over the height of the tube.

E. Experimental Error

Since the use of surface Pitot tubes represents a new technique in open channel hydraulics, a short discussion is presented on the validity of these experiments.

In the discussion on the theory of surface Pitot tubes, Appendix D, evidence is given supporting the validity of Preston's empirical calibration, Equation (9). In addition to these tests, shown in Figure A-11, a check was made with Pitot tubes of two different diameters against the computed local friction in a smooth horizontal flume. The two Pitot tubes gave values of τ_0 which were 3-6% higher than the computed local skin friction, at two different conditions of flow. On the basis of the series of calibration tests, Equation (9) was accepted as being a valid expression for the calibration of round surface Pitot tubes.

Assuming the validity of Preston's calibration, an estimate of the maximum probable experimental error in τ_0 can be determined from examination of the equation itself:

$$\log \frac{\tau_0 d^2}{4\rho v^2} = -1.396 + 0.875 \log \frac{(\gamma \Delta H) d^2}{4\rho v^2} \quad (9)$$

or, regrouping the terms,

$$\tau_0 = 10.02 \rho \left(\frac{v}{d}\right)^{1/4} (\Delta H)^{7/8} \quad (25)$$

Since the error in τ_0 depends on the error in measuring each factor on the right hand side of Equation (25), an approximation of the error in the

computed shear stress, $\tau_o = f(p, v, d, \Delta H)$, may be obtained from the expression,

$$\pm \left| \Delta \tau_o \right| = \left| \frac{\partial \tau_o}{\partial \rho} \Delta \rho \right| + \left| \frac{\partial \tau_o}{\partial v} \Delta v \right| + \left| \frac{\partial \tau_o}{\partial d} \Delta d \right| + \left| \frac{\partial \tau_o}{\partial (\Delta H)} \Delta (\Delta H) \right|. \quad (26)$$

Substituting representative values for the estimated individual errors, it is found that at $\tau_o = 0.0120$ psf, $\Delta \tau_o = 0.0008$, giving a maximum probable error of $\pm 7\%$. In the calculation of $\Delta \tau_o$, the fourth term in Equation (17) accounts for virtually the entire experimental error, the first three terms being negligible. The uncertainty in ΔH , which amounted to ± 0.003 ft., is due primarily to local variations in the velocity distribution (Figure A-11), and to the neglect of secondary currents at the Pitot tube face. It should be noted that, since the wall velocity profiles were measured with the inclined manometer, the error in this procedure is included in the calculated value of $\Delta \tau_o$. The error due to tube orientation (i.e. neglect of secondary currents) was found from measurements in a straight flume to vary essentially as $(1 - \cos \alpha)$, where α = angular misalignment, and amounted to a maximum of 3.4% at $\alpha = 15^\circ$.

From Table II, a comparison of γRS_e with $\overline{\tau_o}$ shows a value of the mean boundary shear stress computed from γRS_e ranging from 4 to 30% higher. Since the total drop in the approach section is less than 0.15", errors of this magnitude can be attributed to difficulties in measuring the water surface slope and thus S_e . The fact that γRS_e gives consistently higher values is explained by the decreased energy dissipation above the curve, which is discussed in Section V-E.

The instrument verification tests were conducted with Models I

and III, since these instruments gave essentially identical results. Due to the design of the Model II static probe (cf. Appendix B), the absolute values of τ_0 determined with this instrument proved to be unreliable, being in general higher than those determined with the other models. Because the three surface Pitot tubes gave slightly different readings of ΔH due to the variations in the static probes, it was necessary to prove that the maps of shear distribution were not significantly affected by the particular instrument used. This was thoroughly checked by mapping the 5" Test with the Models II and III tubes, and the 4" Test with the Models I and II tubes. The Model III tube was also used to check various points on the 3" and 4" Tests. The resulting patterns, mapped as relative shear, $\tau_0 / \overline{\tau_0}$, showed virtually no differences.

Whenever a new tube was used to check a shear map, the fact that it registered slightly different magnitudes of shear stress, made it necessary to re-determine $\overline{\tau_0}$ using the new tube. In this way inconsistencies in the maps of $\tau_0 / \overline{\tau_0}$ were eliminated.

The calibration of the Model III-A tube is not sufficiently refined to warrant a formal discussion of error. In addition to being subject to the same errors as the smooth surface tubes, the uncertainty of the Model III-A is increased by irregularities in the roughness which may either prevent good tube placement of the surface, or may tend to shield the face of the tube from the flow. From inspection of Figure A-14, the error to be expected with this instrument is of the order of $\pm 15\%$.

IX. BIOGRAPHICAL NOTE

Philip Aldrich Drinker was born April 7, 1932 in Brookline Massachusetts. He attended the Phillips Exeter Academy, in Exeter, New Hampshire, for three years, graduating in June 1950. He entered Yale University in New Haven, Connecticut, in September 1951, and received the degree of Bachelor of Science (Cum Laude) in Geology, in June 1954.

From July through October 1954 he was employed by the St. Joseph Lead Co., Bonne Terre, Missouri, as Mine Engineer-in-Training.

In December 1954 he was commissioned in the U.S. Public Health Service, and served for two and one-half years in the Engineering Research and Development Section, Community Air Pollution Program, at the Robert A. Taft Sanitary Engineering Center, Cincinnati, Ohio.

From September 1957 to August 1961 he studied at the Massachusetts Institute of Technology in a program leading to the degree of Doctor of Philosophy in the combined areas of Hydrodynamics and Geology. During the first year of graduate study he held a U.S. Public Health Service Traineeship. Subsequent to this he was appointed Research Assistant in Hydrodynamics for two years. In September 1960, he was appointed Geologist in the Agricultural Research Service, U.S. Department of Agriculture, in which capacity he served during the remaining period of his thesis research.

After September 1961, he will hold the position of Assistant Professor of Hydraulics at the Massachusetts Institute of Technology, Cambridge, Massachusetts. Concurrently with the academic appointment, he will receive a grant for post doctoral research in Hydrodynamics, sponsored by the Ford Foundation.

The author holds membership in the American Geophysical Union,

The International Association for Hydraulic Research, and the Society of Sigma Xi.

Publications:

1. R.S. Brief and P.A. Drinker, Collection of Integrated Samples of Gaseous Effluents, AMA Arch. Ind. Health, v. 17, June 1958.
2. R.S. Brief and P.A. Drinker, Collecting Integrated Gaseous Samples, Chem. Engrg., v. 65, November 17, 1958.
3. A.H. Rose, J.S. Nader, and P.A. Drinker, Development of an Improved Smoke Inspection Guide, Jour. APCA, v. 8, August 1958.
4. A.T. Ippen and P.A. Drinker, Boundary Shear Stresses in Curved Trapezoidal Channels, Presented at the Hydraulics Division Conference of the American Society of Civil Engineers, Urbana, Illinois, August 16-18, 1961, Manuscript in Press with Proceedings, Hydraulics Divn., ASCE.